HIGH-TEMPERATURE AUSTENITIC STAINLESS STEEL

A Dissertation

by

TAYMAZ JOZAGHI

Submitted to the Office of Graduate and Professional Studies of
Texas A&M University
in partial fulfillment of the requirements for the degree of

DOCTOR OF PHILOSOPHY

Chair of Committee,	Ibrahim Karaman
Committee Members,	Raymundo Arroyave
	Amine Benzerga
	Karl 'Ted' Hartwig
Head of Department,	Andreas A. Polycarpou

May 2019

Major Subject: Mechanical Engineering

ABSTRACT

Improvement in CO_2 emission and efficiency of power plants calls for an increase in the operating temperature of such plants. The structural alloys employed are already at their potential limit, which in turn necessitates design of more advanced and efficient alloys. Such alloys must have satisfactory performance at high temperature with reasonable cost. Therefore, while Ni-based alloys can demonstrate the required response, their higher cost compared to their steel counterparts can limit their application. Such steels, however, require improvement in high-temperature mechanical strength, as well as oxidation resistance. To address the former, we hypothesize that a high density of low-energy, high-angle boundaries (e.g. coherent twin boundaries) will improve the high temperature strength, without significantly sacrificing stability or ductility. To this end, conventional 316 stainless steels were thermo-mechanically processed to create a high volume fraction of deformation twins in an austenite matrix with low dislocation density. The deformation twins were found to be thermally stable up to 800 °C, and in some case, they start to disappear at around 1000 °C. This microstructural feature was shown to be beneficial in improving the strength of steel at -100 °C to 500 °C temperature range, while maintaining an acceptable level of ductility. The enhancement of strength of this structure showed a peculiar resistance to increase in temperatures, i.e. the relative increase in yield strength increases as temperature is increased. This behavior was found to be a contribution of thermally-stable twin bands. This unique structure is also expected to perform well in creep condition, and be even further improved through precipitation

strengthening. As for the oxidation resistance, alumina-forming austenitic stainless steels have been proposed as a more stable alternative than chromia-forming steels at high temperatures. There are a few successful alumina-forming system reports in literature, however, they require high levels of microalloying addition, and they were designed mostly in an ad-hoc manner. In this work, we developed an alumina-forming austenitic stainless steel that was designed to employ thermodynamic and kinetics of oxidation. This model also aimed to have the lowest extent of alloying, and to produce the "leanest" alumina-forming austenitic stainless steel composition. Short-term and long-term oxidation tests demonstrated the capability to form alumina scale. This alloy can be used as the baseline for alumina scale formation studies, with further alloying additions.

DEDICATION

To Nazanin, for without her, it would be all grey.

To my parents, for being the firsts.

ACKNOWLEDGEMENTS

First and foremost, I would like to thank my committee chair, Professor Ibrahim Karaman. He has not only been an academic guardian to me, I also proudly call him my life mentor. I believe working with Dr. Karaman has equipped me with tools to be a good researcher, but also has helped me grow into a better version of me. I'm extremely grateful to the wheels of fortune for being assigned as his Teacher Assistant in Fall 2012, and henceforth, being a member of the MESAM group.

Special thanks to Dr. Arroyave who was the co-PI in this project. He has been a great teacher as well as a second adviser to me during my time in Texas A&M. I'm deeply grateful for his support and guidance, and the insightful information and comments he has provided me during every class lecture, or every meeting. I also would like to thank my committee members, Dr. Benzerga and Dr. Hartwig for their guidance and support throughout the course of this research.

Thanks also go to the faculty and staff at the Department of Mechanical Engineering and the Department of Materials Science and Engineering at Texas A&M University. Special thanks go to Robert Barber and Michael Elverud and Murat Kaynak for providing me with the knowledge that comes from years of experience, which a graduate student lacks.

I would like to take this opportunity to thank all my friends and classmates, especially my colleagues in the MESAM group. Dr. Ruixian Zhu for showing me the way and starting me on the world of steels. Drs. James Monroe, Alper Evirgen, Liangfa Hu,

Can Atli, Ebubekir Dogan, Nicholas Bruno, and Li-Wei Tseng for many helpful insights. Special thanks to Dr. Ji Ma for not only being a great roommate, but being a talking Wikipedia of Materials Science. Also Dr. Ceylan Hayerettin and Wahaz Nasim for tolerating me during the years. Many thanks to Dr. Ankush Kothalkar for helping me see the light in the darkness. My deep gratitude goes to Dr. Nicholas Barta, Brian Franco, and Hande Ozcan for being the best friends and colleagues any researcher could ever hope for. Further thanks to Dr. Daniel Salas Mula, Matthew Vaughan, Wenhao Lin, Tejas Umale, Abhinav Srivastava, Omer Karakoc, Ben Young, Jahanzaib Malik, Woohyun Cho, Sezer Picak, Xavier Huerta-San Juan, Raiyan Seede, Alex Demblon, and Willie Trehern, Olga Eliseeva, Dominic Gehring, Joel Sam, and Lei Xue for being wonderful friends, and for making me say “Great I will be spending time with my friends tomorrow”, every Sunday afternoon.

This is also a good place to thank Dr. Bahrololoom, Dr. Shariat, and Dr. Mahzoon in Shiraz University for their help and guidance in my first academic project during my master’s degree. I will be forever grateful to all the teachers in my life.

I cannot thank my parents enough for supporting me thought my life and helping me achieve this point. To my mother for being the first to teach me how to use my brain, and to my father for training my moral compass, and all the life lessons my dear sister taught me.

Finally and most importantly, I want to thank Nazanin Afsar Kazerooni, my dear wife, my best friend, my angel and my muse. If not for her, my life would be probably in

a ditch now, figuratively and even possibly literally. Thanks to her for being the foundation for me to start stepping on the shoulders of the giants. Thanks for all the love and support.

CONTRIBUTORS AND FUNDING SOURCES

Contributors

This work was supervised by a dissertation committee consisting of Professors Karaman [advisor] and Arroyave and Hartwig of the Department of Materials Science and Engineering, and Professor Benzerga of the Department of Aerospace Engineering.

The TEM data were provided and analyzed with the help of Dr. Shujuan Wang and Dr. Peyman Samimi. The oxidation model and implementation in genetic algorithm to design the second generation alloys were part of Chung Juiwang's thesis in Materials Science and Engineering department in Texas A&M University under Dr. Arroyave's supervision. Single crystals of some of the alloys were grown in collaboration with Professor Yuriy Chumlyakov, Tomsk State University, Russia.

All other work conducted for the dissertation was completed by the student independently.

Funding Sources

This study was partly supported by the US Department of Energy – National Energy Technology Laboratory (NETL) under the program "Support of Advanced Coal Research at United States Colleges and Universities," with the grant number of DE-FE0008719.

TABLE OF CONTENTS

Page

LIST OF FIGURES

Page

LIST OF TABLES

Page

CHAPTER I

INTRODUCTION

Motivation

In the United States almost 80% of the power is produced from fossil fuels [1, 2]. This calls for advanced energy conversion systems that are operating at temperatures above 700°C in order to boost the efficiency over 50% and reduce fuel burn, which in turn, demand state-of-the-art heat-resistant, cost-effective alloys capable of operating at these increasingly higher temperatures. This issue poses a significant challenge for materials design in terms of high-temperature performance, especially mechanical response and oxidation resistance. In addition to these issues, fabrication related issues such as formability and weldability must be taken into account as well further down the line. Moreover, the majority of the alloys currently in use in power plants are operating at their potential limit and any further optimization requires significant advances in the alloy design process in a cost-effective manner.

Among the currently available potential alloy systems for high-temperature power plants, ferritic/martensitic stainless steels are rather inexpensive but they do not perform well mechanically in the required temperature range. When oxidation and corrosion resistance are considered, they exhibit even poorer performance [2]. The best option for achieving the desired mechanical response at high temperatures as well as oxidation resistance is nickel-based alloys but they are significantly more expensive than steels. Austenitic steels, however, can perform satisfactorily at temperatures higher than their

ferritic counterparts, while being 3-10 times less expensive than Ni-based alloys. This temperature range is still not as high as Ni-based alloys, but recent researches show promise that the operating temperature of austenitic stainless steel may be increased, through enhancing both high-temperature mechanical strength and oxidation resistance [3].

The improvement in mechanical strength can be basically achieved by creating barriers to dislocation motion, diffusion, and creep. The improvement of oxidation resistance, on the other hand, is more challenging. One possible pathway to achieve better oxidation resistance in austenitic steels is to form protective aluminum oxide scale on the surface, as opposed to the chromium oxide that conventionally forms on the stainless steels. Alumina scale grows at a lower rate than chromium oxide (Figure 1-a) and is thermodynamically more stable than Cr_2O_3 (Figure 1-b) [4], and offers better resistance in more aggressive environments [5, 6], especially in presence of water vapor [7].

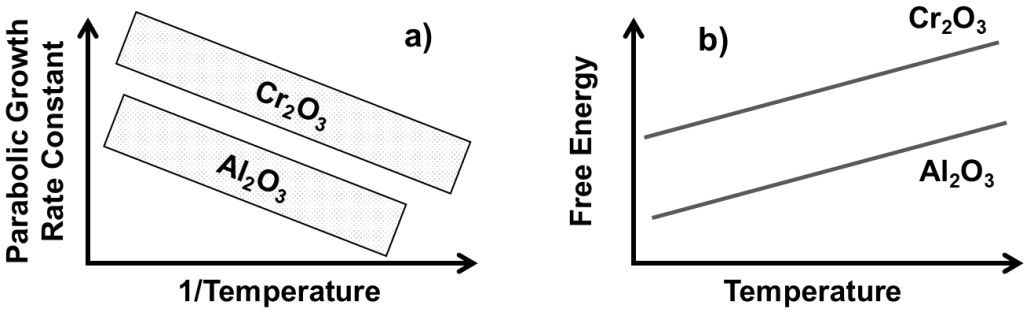

Figure 1 a) Growth rate constants of different oxides at different temperatures, b) free energy and thermodynamic stability of different oxides at different temperatures, showing stability of alumina over other types of oxides for oxidation resistance applications adapted from Brady *et al.*, JOM, 2008 [4].

The purpose of this work is to study the possibility of employing high-angle low-energy boundaries, which are stable at high-temperature, to increase the strength of austenitic alloys. In addition, alumina-scale formation in custom alloys will be studied. The details of the proposed work are presented in the following chapters. The ultimate goal of this project is to develop new austenitic stainless steels with high temperature strength and oxidation resistance. These steels are expected to increase the operating temperatures significantly in power production systems and enhance the efficiency noticeably, which ultimately decreases emission and cost. Our hypothesis is that an austenitic stainless steel with a high density of low energy deformation twins, having low coincidence site lattice (CSL) boundaries, that is capable of forming coherent nano-precipitates and alumina scale, will be able to increase the operating temperatures of this class of materials. This will be achieved through the following chemical and microstructural attributes, as schematically shown in Figure 2:

1) an austenite matrix for high temperature strength and ductility, as well as solid solubility of Ni, Cr, Al and other alloying elements in a wide temperature range, and relatively low stacking fault energy for promotion of deformation twin formation,
2) high density of low-energy high-angle grain boundaries or nano-twin boundaries to enhance strength at high temperatures through impeding dislocation motion without sacrificing the ductility, while maintaining their stability at elevated temperatures resisting boundary migration and creep, which can be obtained by modifying SFE and thermomechanical process,

3) nano-scale precipitates, intermetallics and carbides stable at high temperatures to increase the strength and thermomechanical stability of the aforementioned boundaries, and pinning the boundaries against boundary migration and creep,
4) formation of alumina scale for oxidation resistance at high temperatures, which provides a superior and more stable protective layer on the surface of the alloy as compared with other types of oxides, especially the usual chromium oxide on conventional stainless steels.

The conceptual challenge is that any micro-alloying designed to target any of the features mentioned above may potentially affect the other desired features adversely. For instance, addition of aluminum for promotion of alumina scale that is targeting oxidation resistance, stabilizes ferrite over austenite, and increases stacking fault energy, which in turn negates the effects intended to enhance the high-temperature mechanical strength. These issues will be tackled through processing and microstructure design methodologies, helped with computational methods.

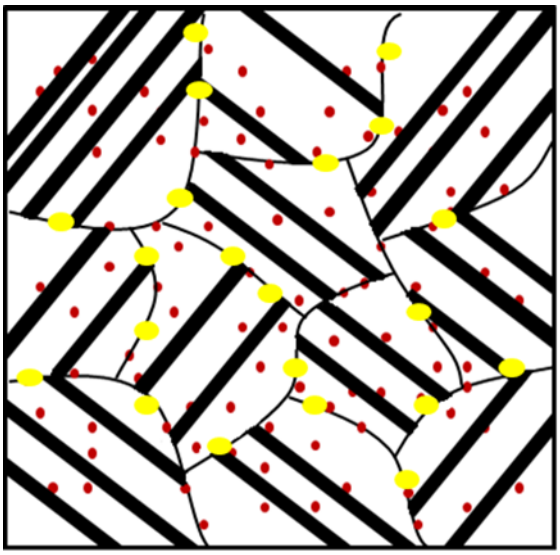

Figure 2 Schematic showing the proposed microstructure, consisting of grain boundaries and twin boundaries pinned by precipitates, that is expected to improve mechanical response at higher temperatures, which when combined with alumina scale formation for oxidation resistance, can increase the operating temperature of the alloy.

Our hypothesis is that a steel with specific structural and microstructural attributes, namely an austenitic matrix capable of forming mechanical twins and controllable precipitates that forms alumina scale, can be used at noticeably higher temperatures in power plant applications, with much lower costs than their Ni-base superalloy counters. The main challenge is, designing the alloy or the process to target any of these attributes will potentially deteriorate the other needed attributes. Therefore, we need to attempt finding an optimum design space where each of the attributes is satisfied. Furthermore, certain building blocks of our hypothesis has not been validated. As an example, it is not known how the deformation nano-twins would influence the high temperature strength of austenitic steels, yet alone there is no systematic work, to the best of our knowledge, on the high temperature stability of these twins, and their contribution to mechanical strength

in an almost dislocation-free matrix. Therefore, one of the significances of this research is that here, we will hierarchically dissect the problem / hypothesis into smaller ones and try to address them separately, and then we'll attempt to find out whether it is possible to integrate various aspects into one final solution to see if our entire hypothesis, i.e. alumina-forming and nano-twinning austenitic steels, would come to a fruition. As it will be presented shortly, the investigation is divided into two major parts: the mechanical-response part where the twinnability and twin stability of different alloys in different states (single and polycrystals) alongside with their contributions to mechanical strength are studied, and the oxidation part where the capability of various new alloys to form protective aluminum oxide layer is investigated. We will also utilize unique thermo-mechanical processing strategies through twinning-induced grain boundary engineering (GBE). In addition, our hypothesized alloy will have only the least number of alloying elements deemed necessary to form a protective alumina scale, excluding elements such as Nb, Ti, V etc. that are present in other current studies in this field. Most of the known alumina-forming alloys contain niobium, and some contain titanium or vanadium, as constituents required for formation of protective alumina scale. In the proposed work, we hypothesize that there might be alloys without these elements forming alumina scale. If proven successful, this work can be the baseline of a primary alumina-forming alloy that can be used for further alloy design that targets further optimization and attributes, such as refractory particle formation for creep resistance. Note that as mentioned above, an integral part of designing ultra-high temperature stable austenitic steels is the consideration of particles that would increase the stability of low energy grain / twin

boundaries and suppress creep further. However, the addition of this third design attribute further complicates the already challenging problem, therefore, the proposed research will focus on the first two parts of our hypothesis, i.e. demonstrating the feasibility of designing alumina forming austenitic steels with stable nano-twins. The particle design part and the feasibility will be left for future studies.

Another significance of the proposed work is that it will be aided with computational studies for performance prediction. Concurrent to this study, theoretical models were employed to predict alumina formation, as well as probability of showing deformation twinning. This computational aid offers the potential to significantly facilitate the investigation, through predicting and presenting trends in properties, such as ability to from alumina in an austenitic structure for different alloys, instead of the conventional empirical path. Specifically, ThermoCalc will be applied to predict the phase diagram of the custom alloys in order to make sure of the presence of a fully austenitic structure, and a thermodynamical model based on the inward diffusion of oxygen and outward diffusion of aluminum will be used to predict the formation of alumina scale.

Background

ASSs are potential materials for use in high temperature power conversion technologies due to their lower cost as compared to Ni-based superalloys and their stability at high temperatures (up to 700ºC [8]) and pressure (35 MPa and higher). Precipitation / dispersion strengthening is commonly employed to increase the creep rupture strength of ASSs. The state-of-the-art commercial ASSs for high temperature applications, such as

NF709 or Sanicro25 are precipitation strengthened by carbides, nitrides and carbo/nitrides, in particular Nb(C,N) and NbCrN [9, 10]. These precipitates are extremely small and stable up to high temperatures, usually above 700 °C [11]. However, their number density is relatively small as compared to the γ' precipitates in superalloys [12]. For example, the density of the γ' particles has been reported to be two degrees of order larger than that of Nb-carbonitrides [13-15]. Alloy 800HT consists mainly of Ni, Fe, Cr, and possess high creep strength and very good oxidation resistance [2]. ASSs 253MA and 353MA are alloyed with nitrogen and rare earth metals [16]. They have high creep strength and very good resistance to cyclic oxidation [17, 18], although none of the current alloys have the high temperature yield strength required in advanced power generation.

Similar to carbides and nitrides [19], stable nanoscale intermetallics are also beneficial to creep and strengthening as they have been reported to improve the creep resistance at elevated temperatures [20-23]. Increased volume fraction of aluminides increases the creep resistance of ASSs [24] and Ni_3Ti nano-precipitates lead to ultrahigh strength levels [25-28]. $Ni_3(AlTi)$ was suggested to be a beneficial precipitate due to the similar crystal structure and good coherency with the austenite phase [29].

In this work, low-energy high-angle twin boundaries as a potential mechanism for strengthening will be discussed. Thin deformation or annealing twin formation is pretty common in Fe-Mn based austenitic steels due to high interstitial carbon content which limits the growth of twins. In ASSs, twinning is not as common as in Fe-Mn-C based austenitic steels due to their higher SFEs and small amount of interstitials. In some ASSs, nano-twins have been obtained through severe plastic deformation (SPD), such as Equal

Channel Angular Processing (ECAP) [25, 30-33] and High Pressure Torsion (HPT) [34, 35]. High tensile strength of about 1.6 GPa accompanied with 17% total elongation has been reported for ECAP processed 316L stainless steel [31]. However, bulk nanostructured steels produced by SPD suffer from both thermal and mechanical instabilities [31, 36, 37].

To best of our knowledge, very few reports have been published on the thermal stability of twins in austenitic steels. It was reported that for twinning-induced plasticity (TWIP) steels, nano-twins could be retained after annealing at 625°C for 120s [38, 39]. A more recent study showed that after annealing at 700°C for 240s, the microstructure of cold rolled Fe–24Mn–3Al–2Si–1Ni–0.06C comprises a mixture of heavily twinned deformed grains and dislocation-free recrystallized grains [40-42]. These works indicate the possibility of retaining deformation twinning at high temperatures while dislocations are recovered. On the other hand, the annealing time in these studies are very short.

Grain boundary studies have revealed that grain boundary-mediated phenomena (grain boundary diffusion, sliding, mobility, precipitation, corrosion, etc.) strongly depend on grain boundary structure and character, which can be controlled within the framework of GBE [43-49]. The premise of GBE is that low-Σ coincidence site lattice (CSL) boundaries are “special” boundaries and increasing their presence in a microstructure would improve its fracture/creep/corrosion resistance [43, 50-53]. Most GBE efforts have primarily focused on controlling the misorientation distribution through thermo-mechanical processing (deformation and annealing). When the appropriate processing conditions are obtained, GBE can also refine the grain size. Since there is a close

relationship between the grain boundary types and deformation and recrystallization textures, one of the methods of GBE is the intentional creation of a texture specified by a high density of low-Σ boundaries. Deformation and annealing twinning in low SFE materials is the most interesting route to achieve the aims of GBE since twins are a subset of Σ3 boundaries and they have been shown to contribute to improved properties [54-56]. Most GBE efforts on polycrystals of low SFE materials have relied on annealing twinning [44, 52, 57, 58]. The effect of deformation twinning on the grain boundary network has not been studied extensively to date because of twinning usually occurs at low temperatures and high strains, and because of complex interaction of slip and twinning. Another factor that has prevented the investigation of GBE through deformation twinning is the lack of good characterization capabilities at elevated temperature. In the alloys studied in the proposed work, twinning will be activated in the absence of large slip activity and a Field Emission Scanning Electron Microscope (FE-SEM) with Orientation Imaging Microscopy (OIM) and high temperature capabilities with a Transmission Electron Microscope (TEM) will be used to characterize evolution of nano-twins at elevated temperatures. The purpose of increasing twin interface density is to significantly enhance the strength without sacrificing ductility [59, 60]. Since twin interfaces are low coincidence site lattice (CSL) boundaries and can have very low boundary energies [61], their effect on creep resistance is expected to be minimal. Twinning propensity will be increased by reducing the stacking fault energy (SFE) through micro-alloying. Previous research has shown that this alloy design strategy is quite effective, particularly in twinning-induced plasticity (TWIP) steels [62, 63]. Grain refinement down to submicron

to nanometers levels should further increase twin propensity, reduce twin thickness, and lead to ultrahigh strength (Figure 3) [30]. The ultimate goal is to increase the high temperature stability of these twins by utilizing different strategies to pin the boundaries and reduce their energies. In conventional Fe-Mn-C steels, deformation twins are stable up to 600ºC for long term heat treatments [64] and up to 700ºC for short term heat treatments [38, 43].

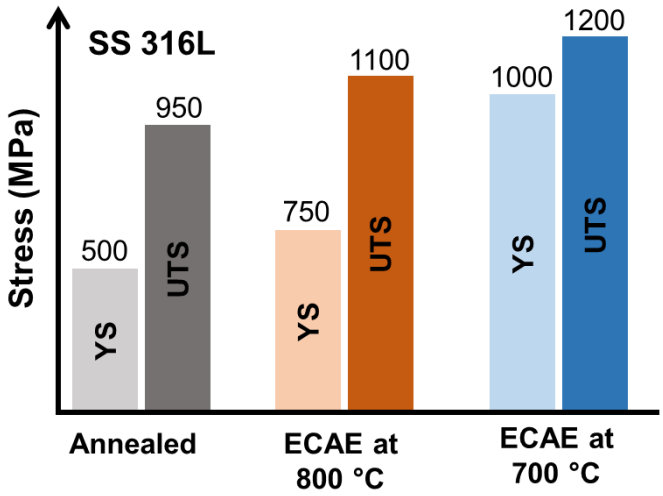

Figure 3 The effect of severe plastic deformation via equal channel angular extrusion (ECAE) resulting in grain refinement in 316L stainless steel, and increasing the yield strength (YS) and ultimate tensile strength (UTS), adapted from Yapici *et al.*, Journal of Material Research, 2004 [30].

In the proposed work, the designed alloys will have low SFE and thus, the deformation twins are expected to form upon deformation at ambient temperature. These deformation twins should lead to the nucleation of low CSL boundaries upon recovery/recrystallization at high temperatures [46]. This twinning-induced GBE approach, associated boundaries with extremely low boundary energies, is expected to

enhance the high temperature mechanical strength of these alloys. The use of austenitic stainless steels at high temperatures is limited by their oxidation resistance in water vapor since Cr_2O_3-based protective scales form volatile Cr oxy-hydroxide species [7, 65, 66] in water vapor and suffers from accelerated corrosion. This leads to loss of protection and significant material loss, especially at high temperatures. The alumina scale, on the other hand, is resistant to oxidation at temperatures up to 1000°C [7, 65-68] This behavior is expected to significantly enhance the corrosion and oxidation resistance of high temperature austenitic stainless steels [69, 70]. As a result, austenitic steels containing 4-5 wt % Al have been designed to form different types of alumina scale [67]. However, high levels of Al are not desired since it is a ferrite former and stabilizer, it increases SFE, and reduces twinnability. Moreover, the addition of Al increases the volume fraction of B2 β-(Ni,Fe)Al precipitates that help improve the creep resistance [24]. Microalloy addition of Nb improves the stability of alumina and increases the volume fraction of B2-NiAl intermetallics further [71, 72]. Similarly, addition of Zr stabilizes the formation of coherent $L1_2$-ordered Ni_3(Al,Ti) precipitates where the interface coherency can be modified by the addition of B [73], but Zr addition are shown to be detrimental for mechanical properties due to coarsening of the carbo-nitrides [74].

Based on the nature of this research, we find it can be best represented if the results were divided into two groups: one group about deformation twins and their thermal stability, and another group about alumina scale formation. The purpose of the first part will be exclusively studying deformation twining: their evolution, their stability, their contribution to the mechanical response. As it will be shown shortly, different materials

in different conditions will be used for this end. On the second part, alloys will be studied only for their ability to form alumina scale, in a solutionized fully austenitic structure.

CHAPTER II

TECHNICAL APPROACH

Materials Selection, Processing, and Microstructure Design

The base material for the present work is a variation of conventional Ni-Cr ASS grades. The base material is used to study the deformation twinning, high temperature stability of nano-deformation twins, the interaction between twins, and their contribution to high temperature mechanical response, with the purpose of fundamental scientific understanding. These is accomplished through systematic thermomechanical processing targeted at increasing the twin fraction density while making the structure almost free from dislocations. Initial studies focus on investigating the high temperature stability of deformation nano-twins. We later utilize thermally stable deformation twins and increase the population of low-Σ CSL boundaries, in order to study their effect of mechanical response. To achieve this end, we strain materials to low levels of elongation, followed by annealing at temperatures low enough to prevent recrystallization yet cause some recovery and reorientation of grain boundaries towards lower energy configurations [75]. The advantage of this approach is to directly see the effect of deformation twins while recovering the dislocations and decreasing dislocation density. Especially, processing single crystals with this approach will provide the opportunity to distinguish the direct effect of deformation twins in mechanical response. Another approach would be dynamic recrystallization during the application of very high strain levels during ECAP. This

method is shown to be effective in refining grain size and obtaining high angle / low energy boundaries in ASSs [25, 30, 76, 77].

To form high density of nanoscale twins, one needs to reduce the SFE of materials and increase lattice friction (to suppress twin growth). Already some relevant research exists on few austenitic steels, investigated twin – slip interactions, and the features of deformation twins (size, fraction, crystallographic orientation dependence, effects on work hardening) at room temperature [30, 62, 63, 78-89]. It was shown that by decreasing SFE and increasing lattice friction, it is possible to obtain high density of nano-twins in austenitic steels (Figure 4-a) [62, 63]. The high twin density in ASSs should considerably increase the attainable strength levels in these materials, as it has been shown in Fe-Mn and 316L ASSs (Figure 4-b) [62, 63, 78-81, 83, 84].

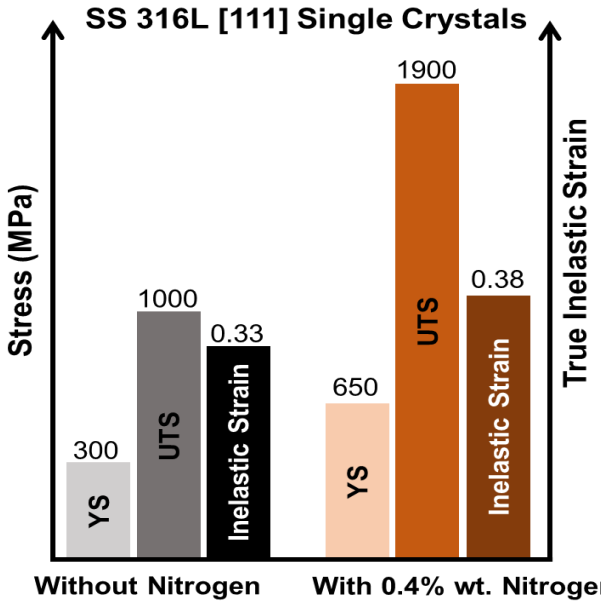

Figure 4 A tremendous strengthening at room temperature because of high propensity of nano-twins in 316L stainless steel due to the enhanced lattice friction after nitrogen addition, adapted from Karaman *et al.*, Acta Materialia, 2001 [78].

The overall idea of the thermo-mechanical processing in the proposed work is sequential to: (1) deform the designed steels to low strain levels at room temperature, (2) obtain high density of deformation nano-twins (~40-50%) with as low as possible dislocation density, and (3) heat treat them to recover dislocations, partially recrystallize the structure forming low energy grain boundaries and submicron grains (since deformation twinning causes sluggish recrystallization). The resulting microstructure is expected to provide superior high temperature mechanical response.

Microstructural Characterization

The goal of the microstructural characterization work is to reveal grain, twin, and precipitate sizes and distribution, and active deformation mechanisms. Transmission Electron Microscopy (TEM) including in-situ heating, Scanning Transmission Electron Microscopy with Energy Dispersive Spectroscopy (STEM-EDS), Scanning Electron Microscopy (SEM), and Electron Backscatter Diffractometry (EBSD) will be used. EBSD will provide information on the twins with small sizes, their respective fraction, and morphology. Phase structures will be determined using the X-Ray Diffraction (XRD) system. The precipitates will be identified with the selected area diffraction techniques. Further, Energy Dispersive Spectroscopy (EDS) technique was employed as well as Wavelength Dispersive Spectroscopy (WDS) to determine the composition of the particles. In a few cases, in order to measure nitrogen content more accurately, a Bruker Elemental G8 Galileo O/H/N (OHN) fusion reaction detector.

Thermo-mechanical Characterization

The materials will be thermo-mechanically tested in polycrystalline forms at temperatures ranging from ambient to high temperatures for their uniaxial stress-strain response. The effects of different GBCDs on deformation stages and deformation mechanisms will be investigated in large-strain monotonic experiments. The load is measured using a load cell on an MTS testing device. Strain is measured using an extensometer with extended legs to measure the change in samples length at different temperatures. The load is then calculated into stress, based on the dimensions of the sample.

Oxidation Testing

The oxidation testing will be carried out in two different groups of durations: short-term and long term. In short term oxidation tests, samples will be tested at elevated temperatures (800°C) and then studied using microscopy to investigate the formed scale. Samples will be cross-sectioned and studied using SEM-EDS to obtain elemental distribution profile. For long term oxidation tests, samples will be oxidized at elevated temperatures for longer durations of time (up to 1000 hours), periodically moved out of the furnace and weighed to obtain the mass change as a function of time. After the long oxidation tests, samples will be studied using SEM-EDS in the cross section.

CHAPTER III

MECHANICAL RESPONSE[1]

Initial Results: Finding the Appropriate Alloys

The purpose of this part is to study the formation and evolution of deformation twins in some existing and newly designed ASSs as a function of applied strain levels and composition, their thermal stability, and their significance on the resulting mechanical response, especially at high temperatures. The criteria that an alloy has to meet in order to qualify as a potential candidate are: it has to have a homogenous austenitic structure, with controllable precipitates, and intermediate or low SFE in order to form deformation twins. Additionally, in order to exclude the effects of crystal orientations, and grain boundaries, on the mechanical response of deformation twins and their stability, a part of research will be conducted on single crystals. The list of alloys that were investigated are as follows:

- *Fe-Mn-C (Hadfield Steel) Single Crystals*

One of the promising alloys for investigating deformation twins is Hadfield steel. Previous work on this alloy demonstrated its ability to form deformation twins. Single crystal samples oriented along the [111] direction with the composition shown in Table 1 were prepared and uniaxially tested at room temperatures to 5%, 10%, and 20%

[1] Part of the data reported in this chapter is reprinted with permission from "Hierarchical evolution and thermal stability of microstructure with deformation twins in 316 stainless steel" by S.J. Wang, T. Jozaghi, *et al.*, 2017. Materials Science and Engineering: A, 694, 121-131, Copyright 2017 by Elsevier B.V.

engineering strains under tension (Figure 5). This specific crystalline orientation was chosen because it promotes the most twinnability. Figure 6 is OM and TEM of 20% strained sample, showing large volume fractions of deformation twins, with relatively low dislocation density. Figure 7 shows the inverse pole figure (IPF) and orientation map of this sample, and wide bands of twins are visible. So far, this alloy appears to be a very good candidate for deformation twinning studies, however, upon heating to 500°C (Figure 8) and 600°C (Figure 9) for 1 hour, a new set of texture component starts to show up on the IPF that corresponds to the evolution of another phase. Figure 10-a shows phase map of the sample heat treated at 600°C for 1 hour, and it can be seen that α-ferrite is starting to form. Moreover, this new ferrite phase appears to be evolving without any preferred crystallization sites (Figure 10-b). This second phase evolution makes Hadfield steel inappropriate for the study, as the design criterion for this part of study was a fully austenitic single crystalline structure with a specific orientation in a wide range of temperatures.

Table 1 Chemical composition of Hadfield steel

Elements	C	Mn	Si	P	Cr	Mo	Ni	Al
wt%	1.03	12.34	0.9	0.01	0.38	0.12	0.46	0.05

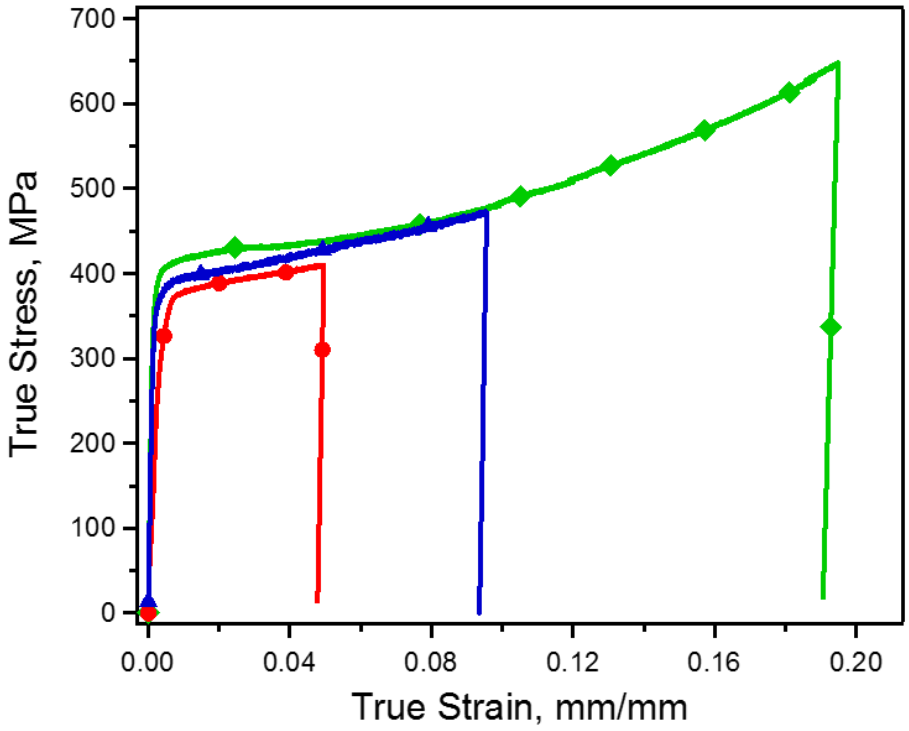

Figure 5 Stress-strain response of Hadfield steel [111] single crystals.

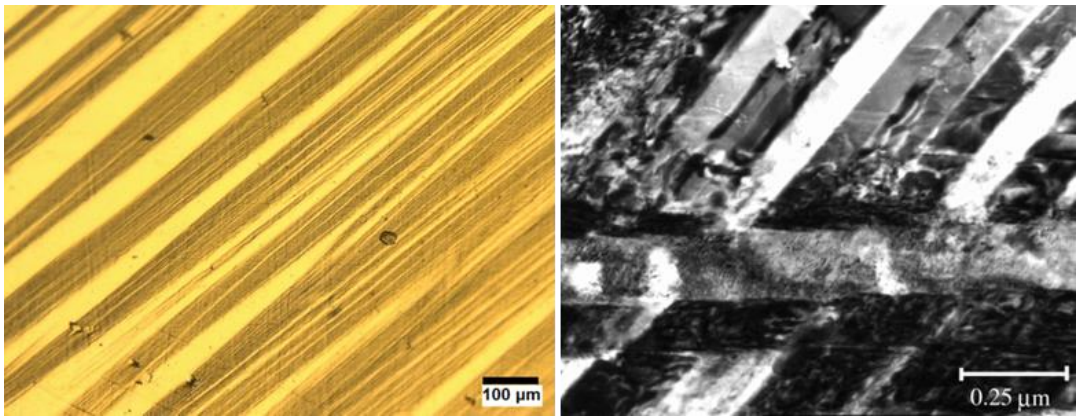

Figure 6 Hadfield steel [111] single crystals deformed to 30%, left) OM, right) TEM image, with large volume fraction of twins and low dislocation density.

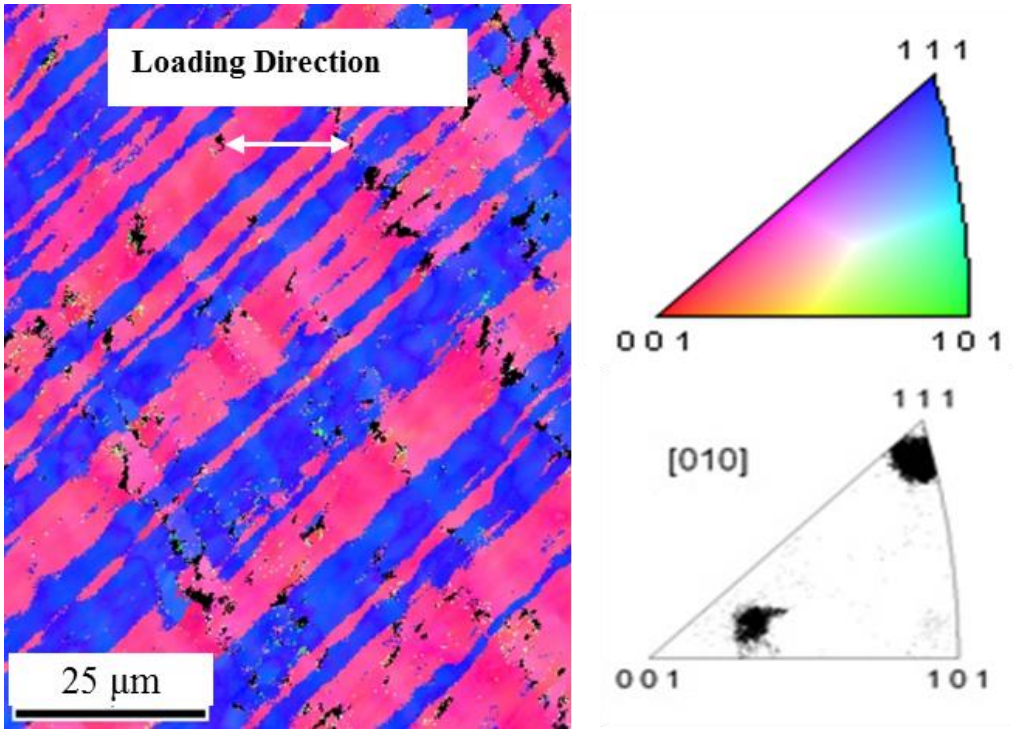

Figure 7 Hadfield steel [111] single crystals deformed to 20%, inverse pole figure (IPF) and orientation map obtained from EBSD, showing large volume fraction of twins.

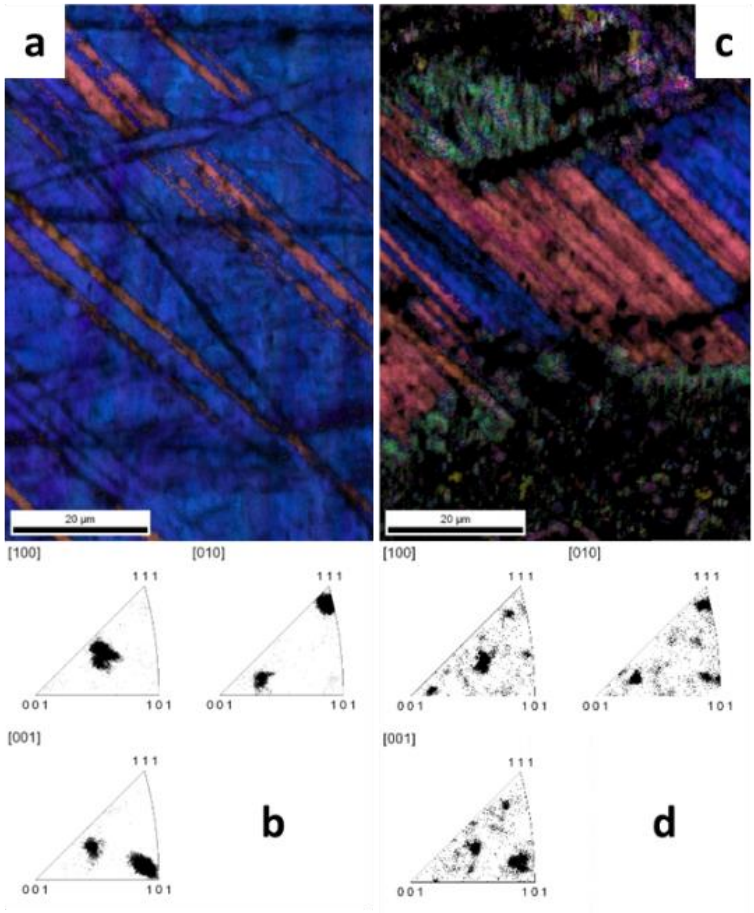

Figure 8 Hadfield steel [111] single crystals deformed to 20% tensile strain, a) EBSD IPF map and b) EBSD IPFs, c) IPF map after heat treatment at 500°C for 1 hr and d) IPFs.

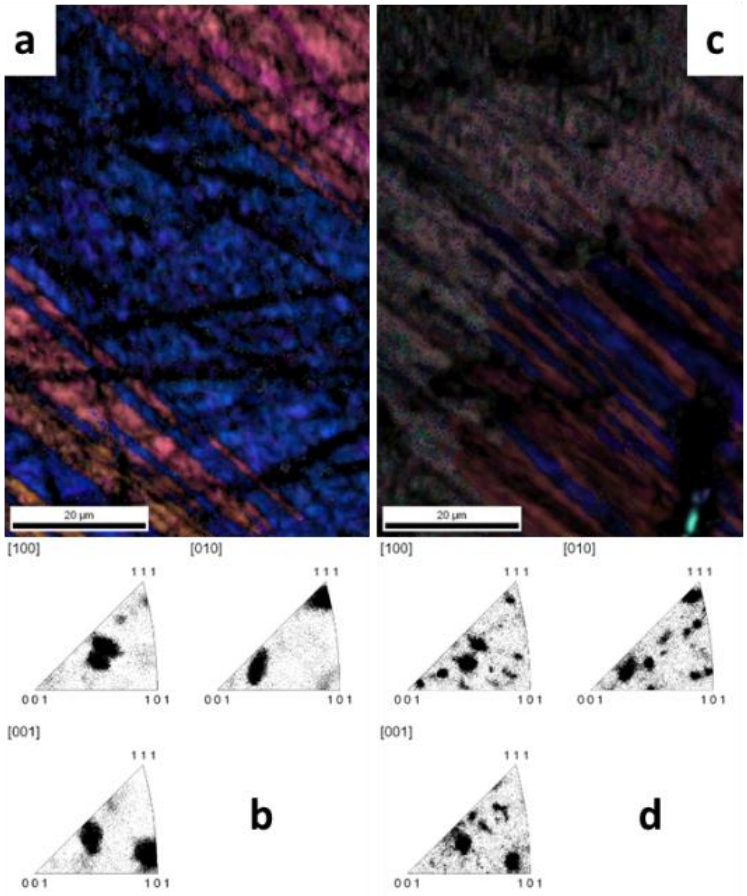

Figure 9 Hadfield steel [111] single crystals deformed to 20% tensile strain, a) EBSD IPF map and b) EBSD IPFs, c) IPF map after heat treatment at 600°C for 1 hr and d) IPFs.

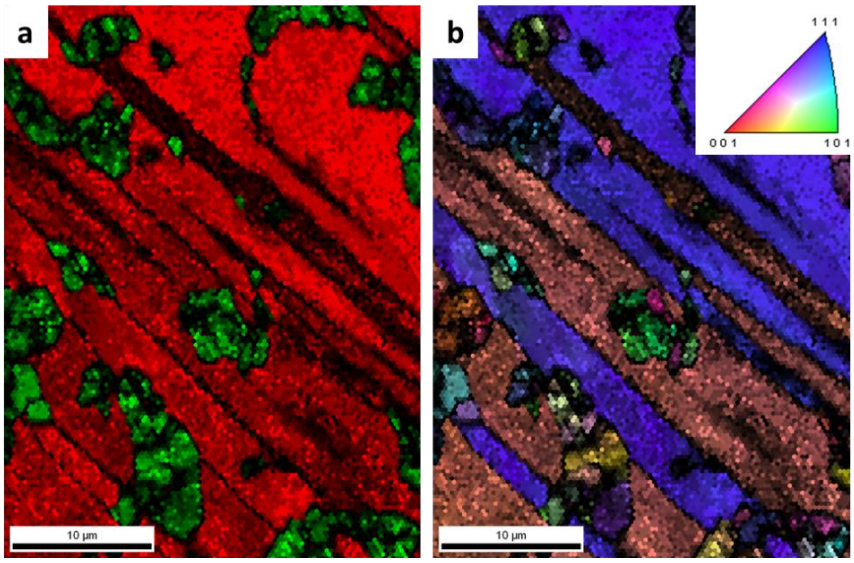

Figure 10 Hadfield steel [111] single crystals deformed 20%, after heat treatment at 600°C for 1 hr, a) phase map showing austenite in red and ferrite in green, b) IPF map.

- *316L+N Stainless Steel Single Crystals*

316L stainless steel plus 0.20 wt.% nitrogen single crystals were tested next. Previous research showed that this alloy is expected to show deformation twins. In order to study the role of deformation twins on mechanical response and their high temperature stability, uniaxial tension tests were performed along [111] direction to maximize the twinnability, both at room temperature and at -80°C (through conduction by cooling the grips using liquid nitrogen flowing through copper tubing), in order to suppress dislocation slip. This specific [111] direction was chosen because in fcc crystals, this direction is known to promote mechanical twinning under tension due to the high Schmid factor for twinning along this orientation [78]. The stress-strain behavior is presented in Figure 11. Figure 12 shows the OM and SEM of the surface features of samples tested to 10% elongation at both room temperature and -80°C. The observed surface features may be an

indication of deformation twins, but the EBSD on the -80°C sample (Figure 13-a) and the TEM (Figure 13-b) do not confirm this. As a results, it was decided that deformation twinning either does not occur or cannot be detected in this alloy, at room temperature or at -80°C. It has been shown that the stacking fault energy is a non-monotonic function of nitrogen content [90], which makes it possible that deformation twins do not form in this specific alloy with its specific nitrogen content.

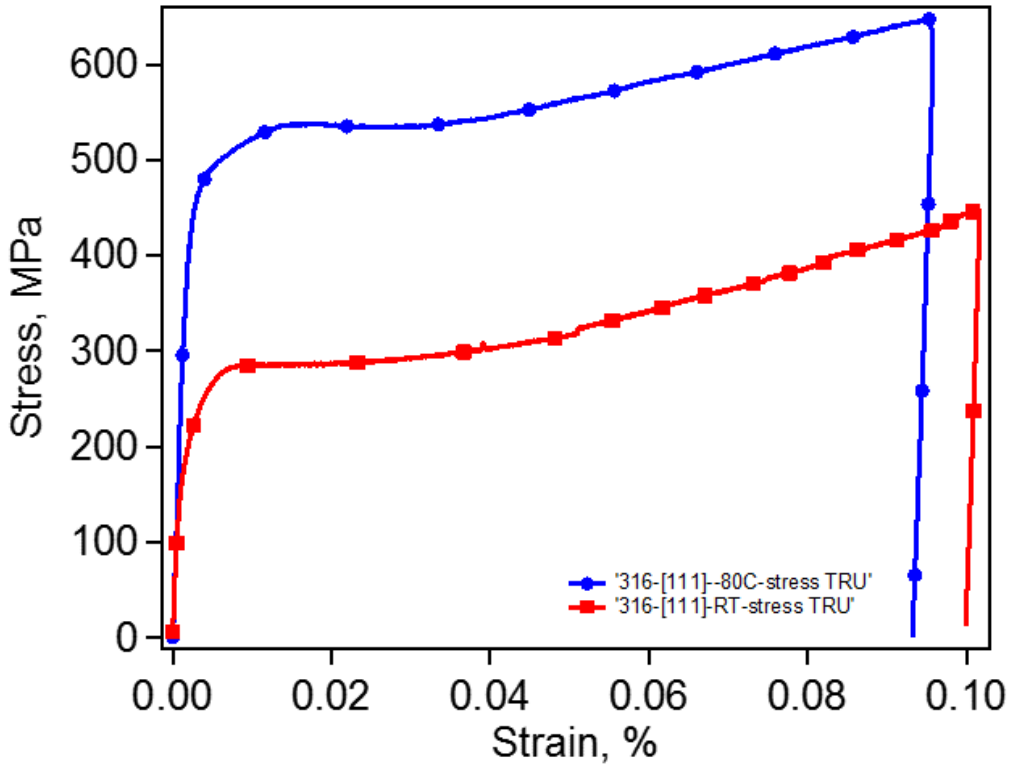

Figure 11 Stress-strain behavior of 316L+N SS at room temperature (red) and at -80°C (blue).

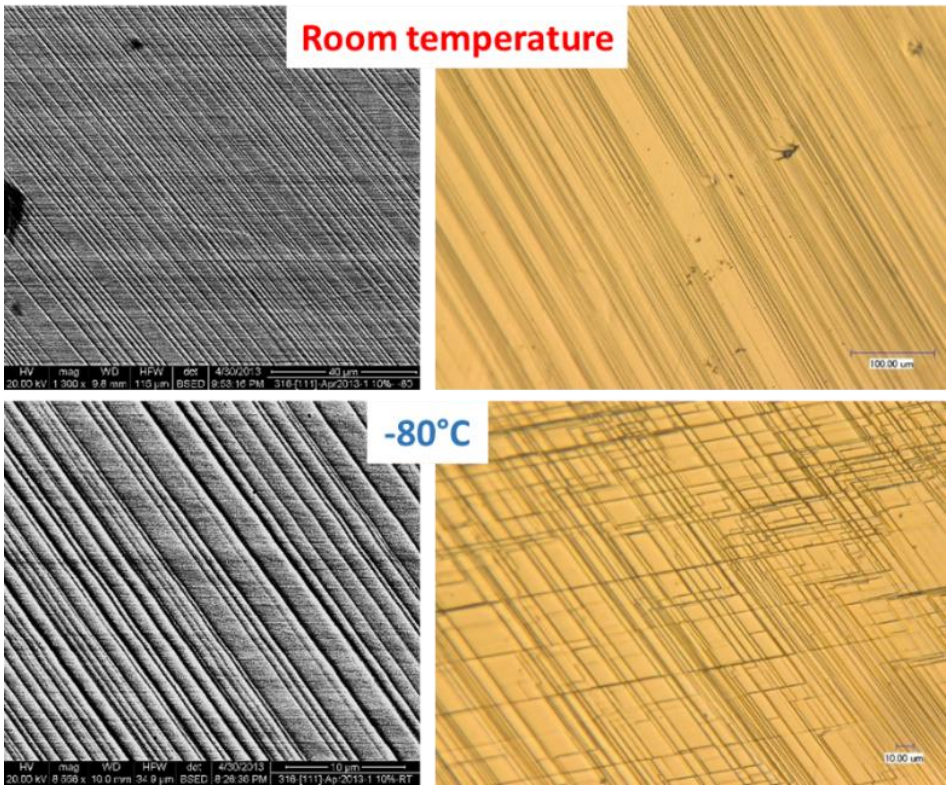

Figure 12 316L+N SS 10% deformed at room temperature and -80°C, OM images showing surface reliefs.

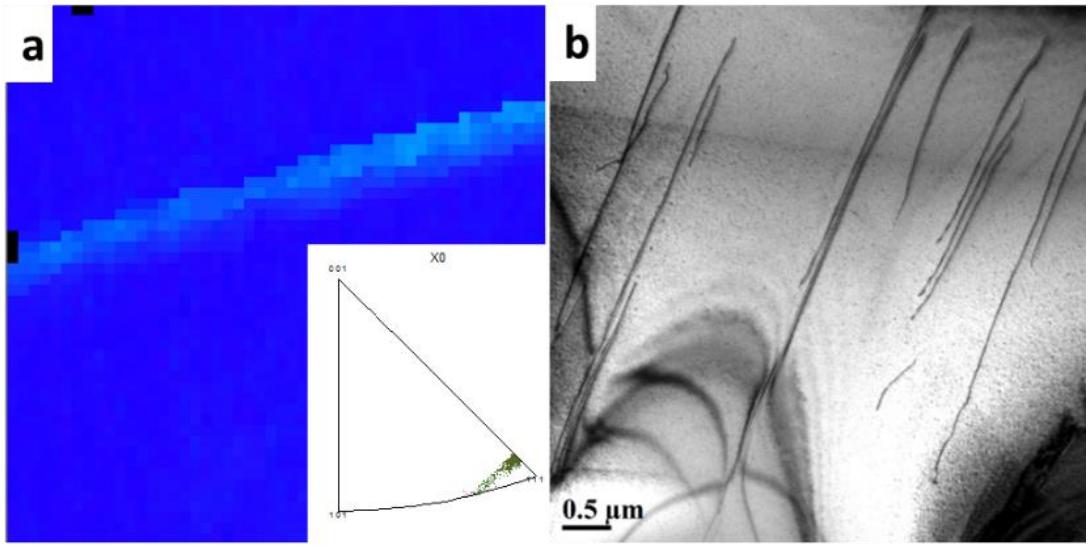

Figure 13 316L+N SS 10% deformed at room temperature and -80°C, a) EBSD IPF and map, b)TEM. No twins can be detected.

- *316 Stainless Steel Single Crystals*

316 stainless steel was selected next, after our first two candidates failed to meet the criteria (which are fully austenitic structure and forming of deformation twins) as a baseline material for studying deformation twins, since it is one of the most widely used structural material that has been reported to show deformation twins. Single crystals of 316 SS were prepared with a composition of Fe-18Cr-9.5Ni-2.5Mo-1.7Mn-0.7Si (wt%) using Bridgman technique. The composition was determined using EDS. Dog bone tensile samples were prepared along [111] direction of the crystals. Uniaxial tensile tests were performed at room temperature to an engineering strain of 10 % and 20 %, with constant displacement rate of 0.04 mm/sec. The stress-strain graph is shown in Figure 14-a. Figure 14-b shows the optical image of the surface relief on the specimen after the uniaxial test of 20%, and parallel features that may be indicative of twins are present on the surface. Figure 14-c shows the EBSD map and associated inverse pole figure of this sample, which clearly indicate the signs of twinning through an abrupt orientation change. In Figure 14-d, transmission electron microscopy image of the samples shows very thin bands of twins. 316 SS single crystals definitely demonstrate deformation twins.

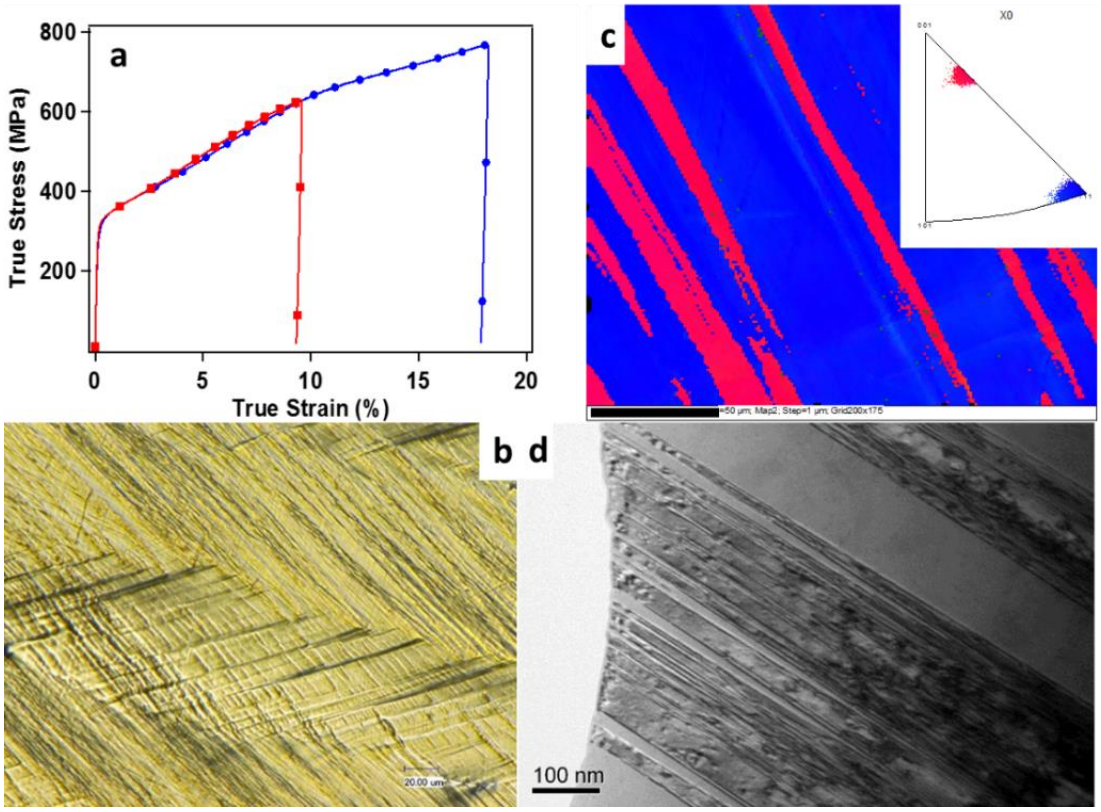

Figure 14 316 stainless single crystals oriented along the [111] direction. a) uniaxial tension stress-strain curve, c) EBSD of 20% elongated sample showing IPF and map, b) OM image of 20% elongated sample, d) TEM image of 20% elongated sample. Twin nano-bands with significant volume fraction were detected.

- *316 SS Polycrystals*

Since 316 stainless steel show twinning as one of the major deformation mechanisms, we will study the stability of the deformation twins at high temperatures to understand their effect on high temperature mechanical response. However, in practical applications, one needs to use polycrystals since single crystals are expensive and polycrystals are stronger. Therefore, one needs to understand the interaction of twins and grain boundaries on the mechanical response, and high temperature stability, and explore the possibility of exploiting these interactions. To begin with, we will study deformation

twins, their thermal stability, and their contribution to mechanical response at room and high temperature in 316 SS polycrystals. Figure 15 depicts IPF map of a fully annealed 316 SS polycrystalline sample, and it shows an equiaxed, fully austenitic structure with random grain orientation. Mechanical response of this alloy is depicted in Figure 16. A sample deformed to 20% tensile strain was studied using EBSD and Figure 17 shows the IPF map, and along with the misorientation angles, the bands of deformation twins can be detected. The TEM image is also depicted in Figure 18, showing a noticeable number of twin bands. This alloy will be used for studying the volume fraction of twins with the extent of deformation, and their thermal stability, as well as their effect on mechanical response, through systematic thermo-mechanical cycles.

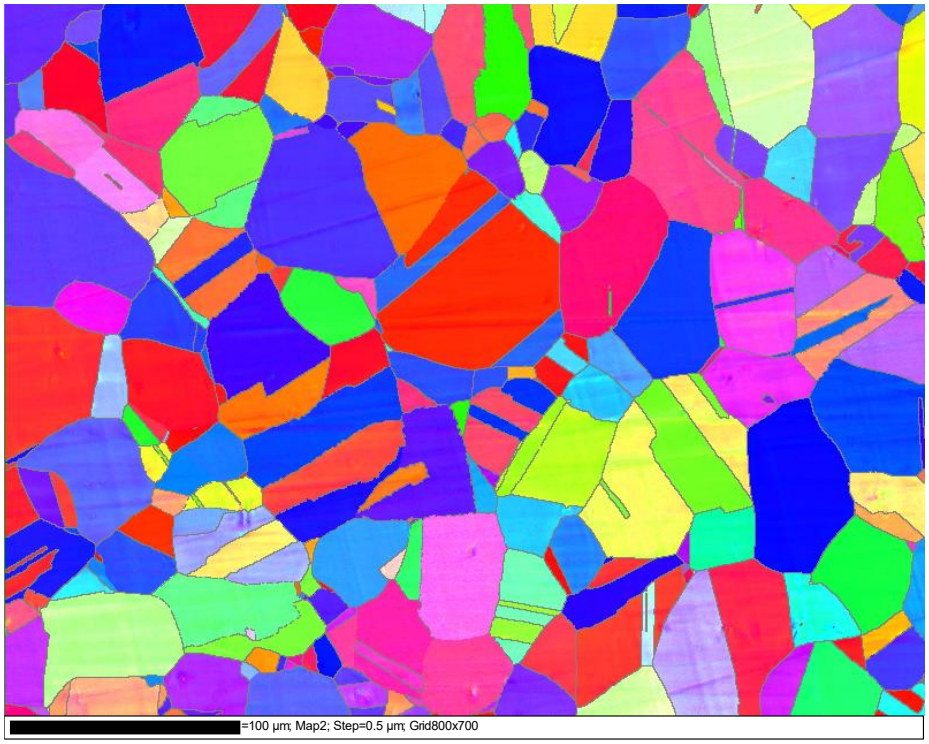

Figure 15 Polycrystalline 316 SS, IPF map, showing homogenous structure with equiaxed grains after annealing.

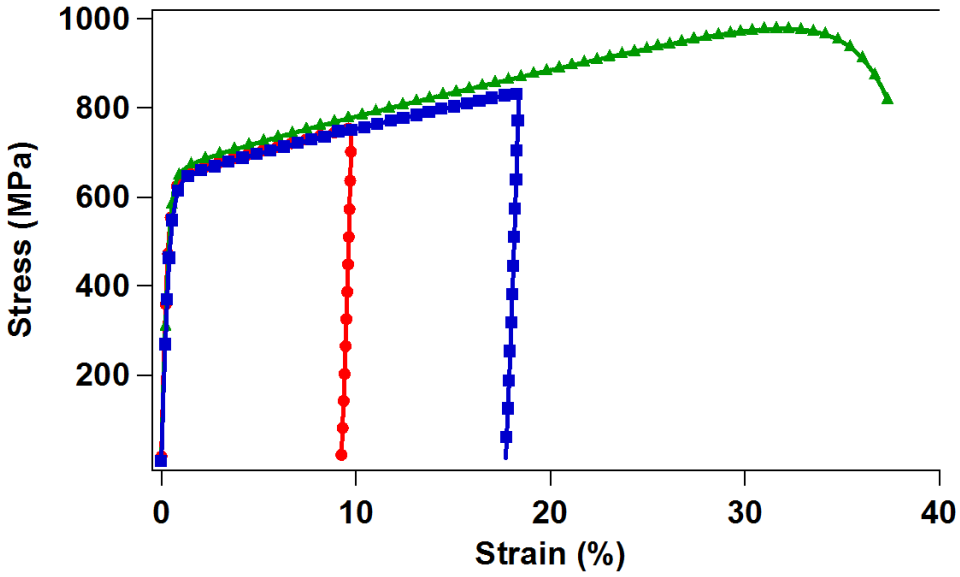

Figure 16 Polycrystalline 316 SS true stress-strain curve to 10% and 20% engineering strains, and to-failure.

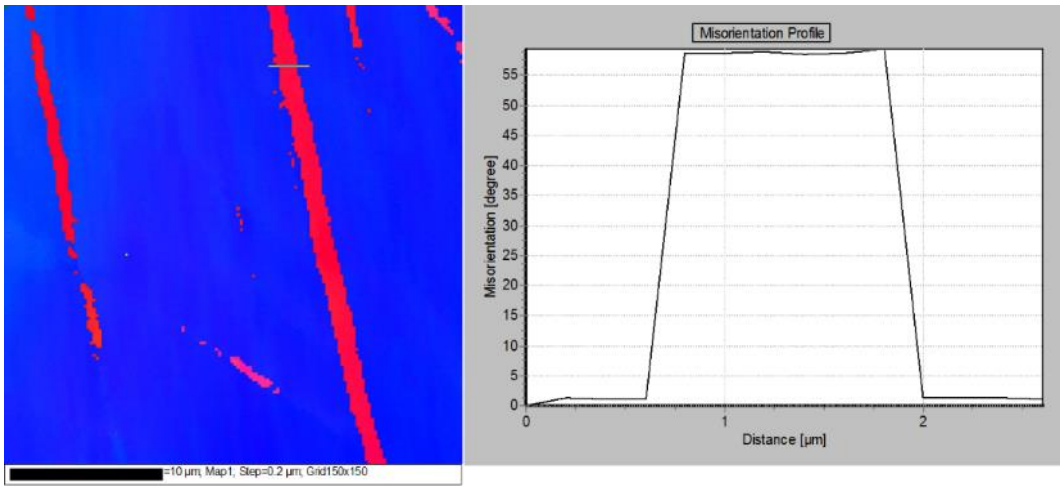

Figure 17 Polycrystalline 316 SS deformed to 20% engineering strain in tension, EBSD IPF map and the corresponding misorientation angle profile along the depicted line, confirming deformation twin.

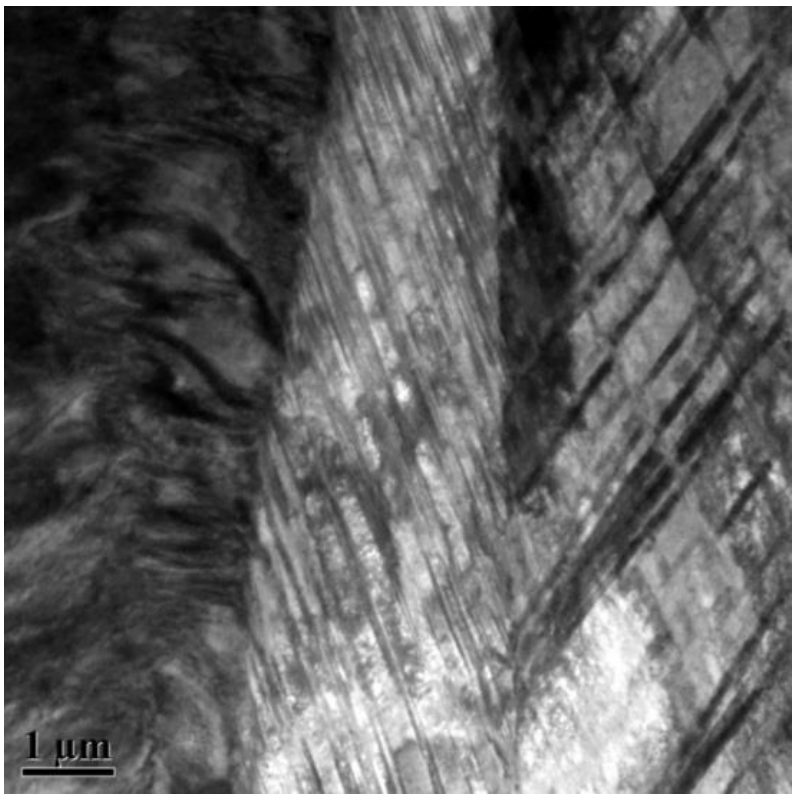

Figure 18 TEM image of polycrystalline 316 SS deformed to 20% engineering strain in tension, detecting twins nano-bands.

Hierarchical Evolution and Thermal Stability of Microstructure with Deformation Twins in 316 Stainless Steel

In order to improve efficiency of current power plants and decrease their CO_2 emission, new structural materials are needed that can perform reliably at higher temperatures. These materials need to maintain their mechanical properties at high temperatures [9, 91]. Aside from the expensive Ni-based superalloys, ferritic steels can be utilized for these applications, due to their low thermal expansion coefficient, high thermal conductivity, and irradiation resistance [92], especially in irradiation environments such as nuclear power plants. In fossil fuel power plants, austenitic stainless steels are the materials of choice based on their good high-temperature mechanical properties and oxidation resistance [93]. Further improvements of creep resistance in austenitic stainless steels have been achieved by adding carbide and carbonitride forming alloying elements [3, 94], which can pin the grain boundaries as well as mobile dislocations by forming nano-scale particles. Another method to improve the mechanical properties of austenitic stainless steels is microstructural engineering through thermo-mechanical processing. Dislocation slip and twinning are two competing deformation mechanisms during plastic deformation in austenitic stainless steels. However, the govering deformation mechanism is dictated by both the intrinsic properties of the steels such as crystal orientation or crystallographic texture, grain size, and stacking fault energy (SFE), and the extrinsic conditions such as strain level, strain rate and temperature [62, 83, 95]. As an intrinsic property of materials, SFE is the main factor controlling the ease of cross-slip or twinning in face-centered-cubic (fcc) metals and it plays a key role in dictating deformation stages

of austenitic stainless steels [96-98]. As the SFE decreases, the separation distance of partial dislocations widens. Thus, cross-slip of dislocations becomes more difficult and mechanical twinning is favored. In austenitic stainless steels (SSs), which commonly have a low to moderate SFE, early stages of deformation are dominated by slip, then stacking faults are formed before twinning dominates the deformation [99]. Formation of twins can provide many interfacial barriers for dislocation motion, reduce the dislocation mean free path which can result in large work hardening coefficients and enhanced tensile strength [78, 83]. Extensive mechanical twinning was observed in 316L austenitic SS under various deformation strain paths such as tension [30, 78, 97], compression [97], and severe plastic deformation (SPD) [30, 31, 60] due to its intermediate SFE. Although deformation twinning behavior during mechanical deformation has been widely studied in 316 [78] and other types of austenitic stainless steels [38, 60, 78, 97, 100, 101], the quantitative information on twins, such as the evolution of the volume fraction and size, under different strain levels, was rarely studied previously [100]. In the present work, we show a hierarchical microstructure evolution in 316 SS due to deformation nano-twins and their bundles, and statistically estimate the volume fraction evolution of these twins at different tension strain levels. Although the formation of deformation twins can significantly enhance the strength, ductility and work-hardening ability are usually sacrificed. Two strategies were recently proposed to achieve a better combination of yield strength and ductility in twinning induced plasticity steels (TWIP), which are based on the thermal stability of mechanically induced twins. One strategy includes the use of partial recrystallization of prestrained materials, either through a cold rolling or dynamic plastic

deformation. With this method, TWIP steels with nano-scale mechanical twins were achieved [60, 102-104]. Another strategy is based on the recovery of cold-rolled TWIP steels with nano scale mechanical twins [38, 100, 101]. Nano scale twins formed during pre-straining process can significantly increase the strength of the materials [105]. It is expected that a subsequent recovery or partial recrystallization heat treatment should increase ductility and work hardening by reducing the dislocation density between the twins. Bouaziz et al. [101] compared the effect of both recovery and recrystallization on the combination of yield stress and uniform elongation for a given TWIP steel composition at room temperature. They showed that the recovery process allows achieving higher strength-ductility combination than that reached via partial recrystallization. It is then suggested that recovery is a more adequate process, able to increase the initial strength values of TWIP steels, while keeping large ductility levels. The recovery strategy presented on TWIP steels has also been successfully applied to 316L SS leading to a noteworthy combination of high yield strength and strain hardening [106]. However, only one deformation-annealing cycle was performed on that 316L SS study. In the present work, the role of several deformation-annealing-deformation cycles on the resulting mechanical response of 316 SS were revealed with the propose of achieving high density of nano scale twins while eliminating dislocations, such that an excellent combination of strength and ductility can be reached. Clearly, thermally stable mechanical twins can play an important role in the enhancement of strength and ductility combination. However, the investigations on the level of thermal stability of mechanical twins are limited. In conventional Fe-Mn-C steels, mechanical twins were shown to be stable up to 550 ºC for

1 hour heat treatments [64]. Bouaziz et al. observed that the nanometer-scale mechanical twins introduced by pre-straining high-manganese TWIP steels at room temperature were stable up to the recrystallization temperature (625 ºC) [38]. They also reported that the deformation twins in 316L SS after cold rolling to 37% reduction were stable after a recovery treatment at 600 ºC for one hour [106]. Growth nano twins in as-deposited 330 SS films can survive at 500 ºC for 1 h [107]. Furthermore, it was shown that the twinning stability can be notably enhanced by microalloying at high temperatures in Fe-Mn austenitic steels with low carbon contents [108]. However, the extent of the thermal stability and the role of these stable twins on the subsequent mechanical response have not been systematically studied. In the present work, various heat treatments are performed on uniaxial tensile deformed 316 SS with different volume fractions of nano-twins. The thermal stability of deformation nano-twins and their effect on the subsequent room temperature mechanical response are studied. The results presented herein can be helpful to exploit new austenitic stainless steels with enhanced performance at elevated temperatures.

Microstructural Evolution During Tensile Deformation, and Static and In-situ Annealing

Representative microstructures of the as-received materials are shown in Figure 19, obtained using OM (Figure 19-a) and TEM (Figure 19-b). Equiaxed grains with an

average size around 60 μm were detected using the linear intercept method. Annealing twins are noted in some grains in the figure. There are few dislocations within grains as shown in Figure 19-b. The Vickers hardness of the AR specimens was measured to be 151.5 ± 4.6. Tensile tests until failure were performed on the as-received (AR) samples (Figure 20). The true uniform elongation was determined to be ~47% ± 1%. Significant work hardening was noticed in the AR samples. Engineering strains of 10%, 20%, 30% and 40% were chosen to study the evolution of the microstructure in the AR specimens during deformation.

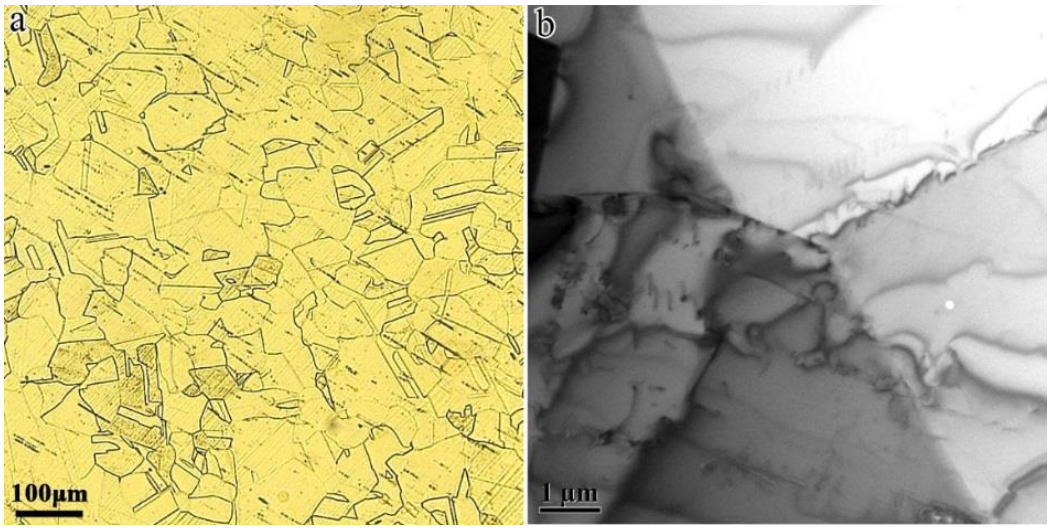

Figure 19 The microstructure of the as-received 316 stainless steel (SS) observed using (a) optical microscopy and (b) TEM. The average grain size is around 60 μm. Annealing twins are visible in some grains.

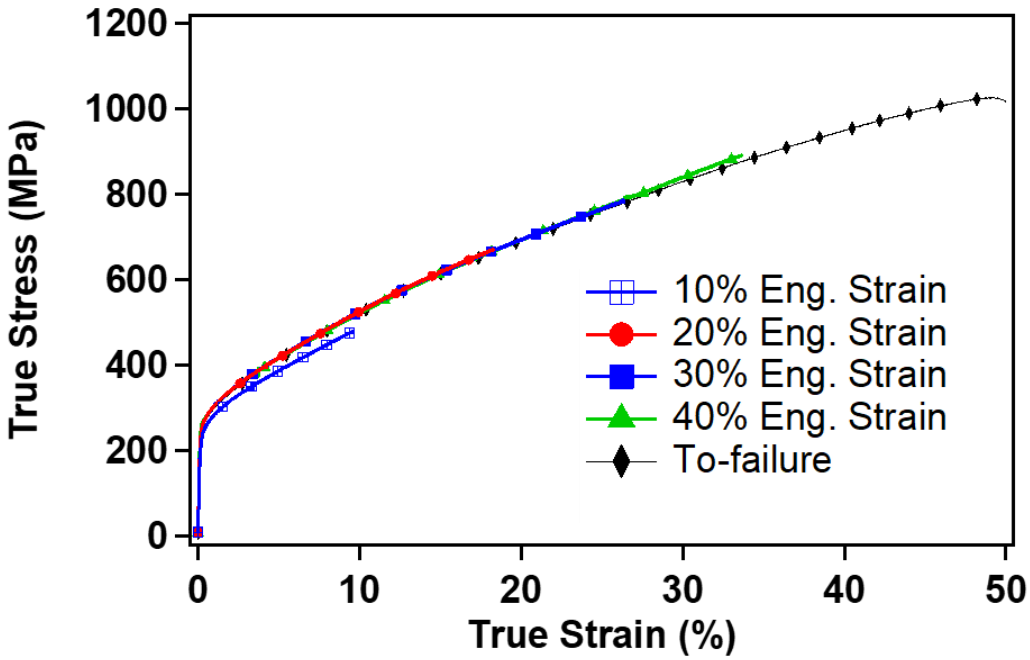

Figure 20 Tensile true stress-strain curves of 316 SS polycrystals, with 10%, 20%, 30%, 40% applied engineering strains (corresponding to 9%, 18%, 26%, and 33% true strain, respectively), and up-to-failure elongation.

After 10% deformation, most of the grains have numerous planar dislocation structures shown in Figure 21-a with a TEM image. In the 20%, 30% and 40% deformed specimens, many nanoscale deformation bands coupled with high density of dislocations were detected as shown in Figure 21-(b-d). These bands were verified as deformation twins using selected area diffraction patterns (SADP) in the inserted image in Figure 21-b which shows these twins to be {111}<112> type. After 800ºC heat treatments (HTs) for 1 hour, most of the dislocations in the deformed specimens were recovered, but the nano-twin bands were preserved, as shown in Figure 22. After 900ºC HTs for 1 hour, some deformation nano-twins still existed, and recrystallization appeared in all the deformed specimens. Microstructure differences were noticed between (20%, 30%)-900ºC HT and

40%-900 ºC HT samples. The major microstructural features in the (20%, 30%)-900 ºC HT samples are deformation nano-twins as shown in Figure 23-(a,b), and the minor microstructural features are recrystallized grains as shown in Figure 23-(d,e). However, in the 40%-900 ºC HT samples, the major microstructural features are recrystallized grains (Figure23-c), and deformation twins still exist in few grains (Figure 23-f). These recrystallized grains are generally several microns in size. Interestingly, some recrystallized grains were captured forming at the intersection of two different twin variants (Figure 24).

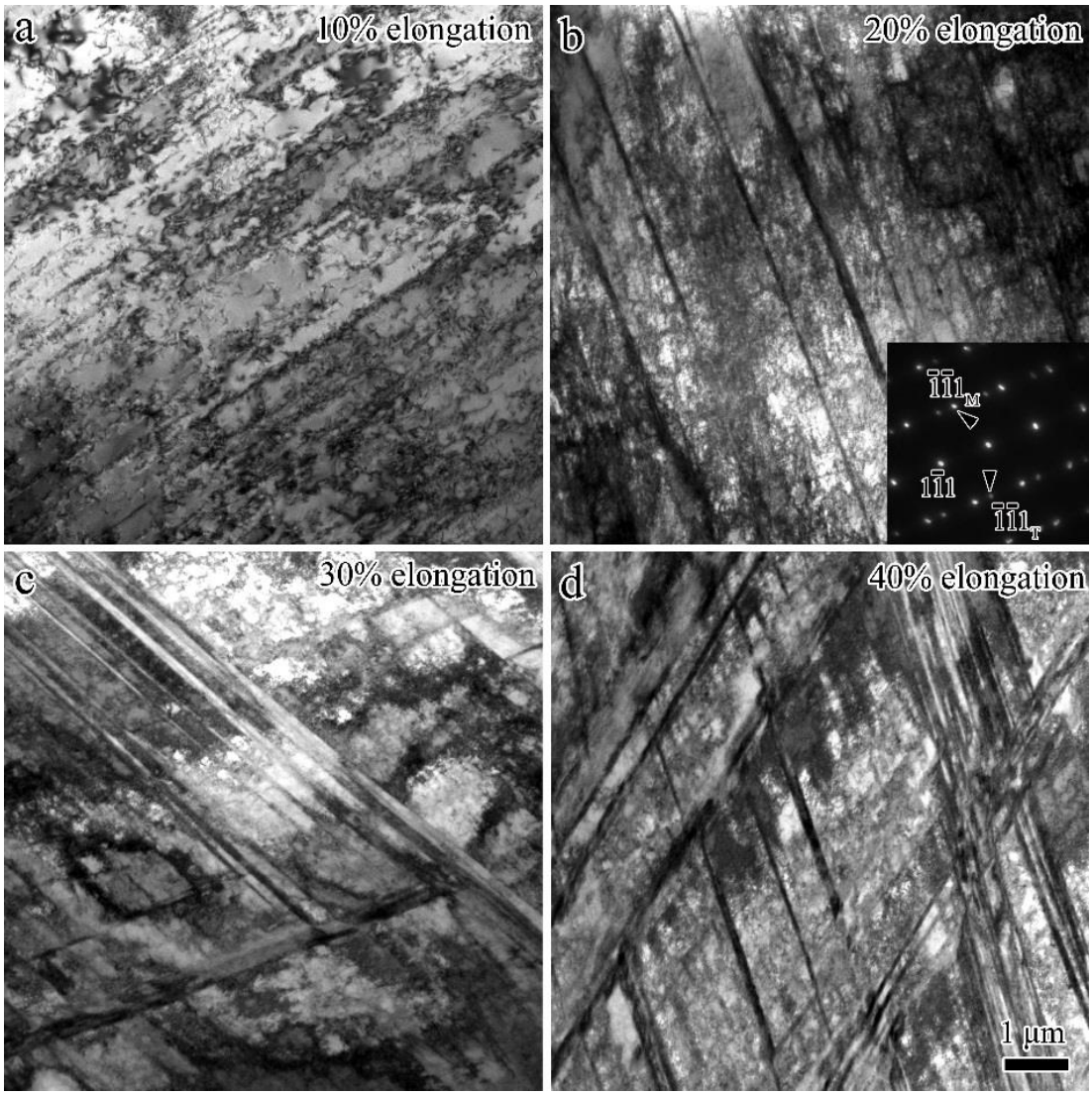

Figure 21 Bright field TEM images of the microstructures after (a) 10%, (b) 20%, (c) 30% and (d) 40% tensile elongations. In the 10% deformed samples, there are numerous planar dislocations. The inserted SADP in (b) shows the observed deformation bands in (b,c,d) to be {111}<112> twin bands. The density of the twin bands increases with increasing strain level.

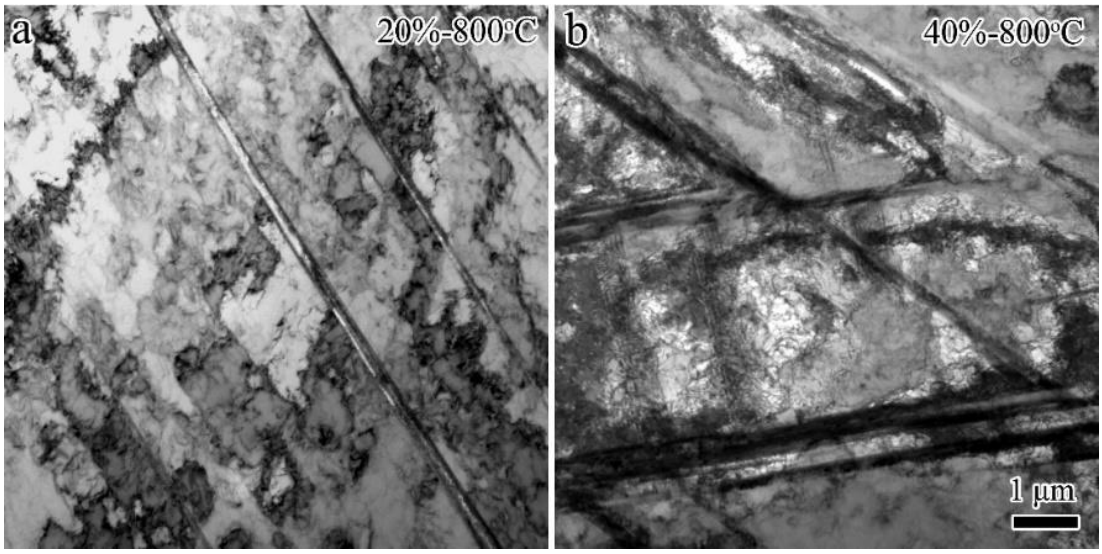

Figure 22 Bright field TEM images of the microstructures of the 316 SS specimens deformed under tension for (a) 20% and (b) 40% after annealing at 800ºC for 1 hour. Many deformation nano-twins survived after the annealing at 800ºC for 1 hour. Dislocation density decreased notably.

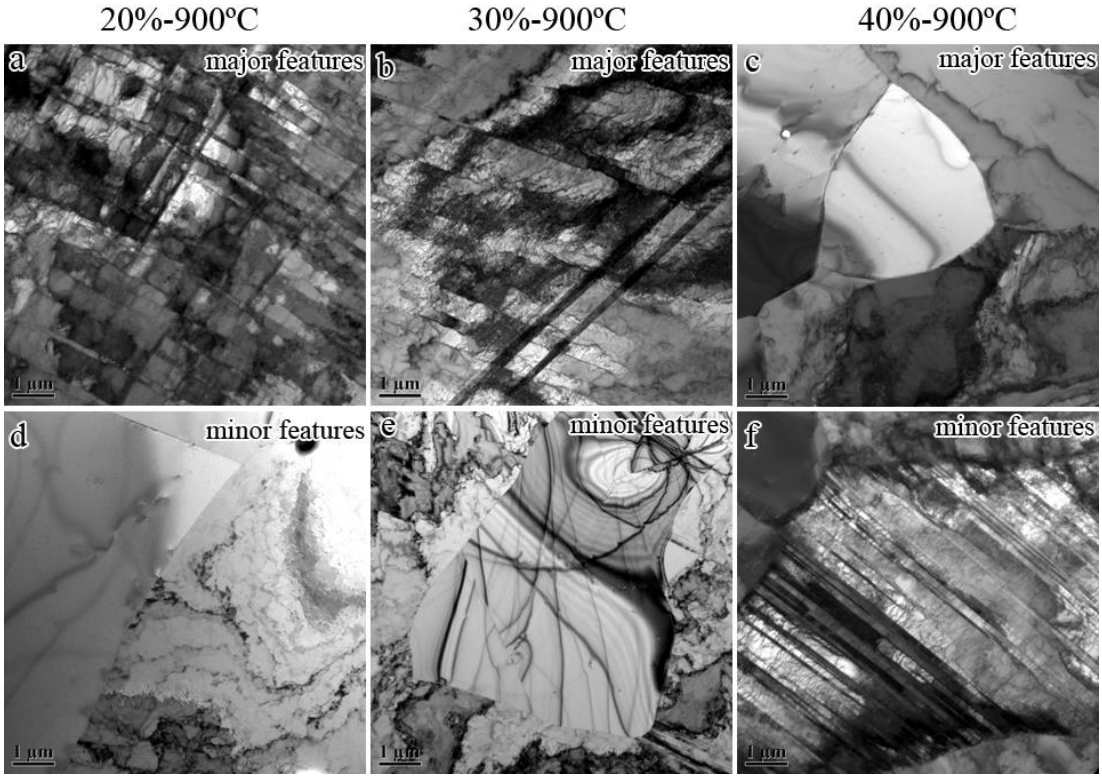

Figure 23 Bright field TEM images of 316 SS showing the major (a-c) and minor (d-f) microstructural features after 900°C annealing for 1 hour of the samples deformed under tension at different strain levels (a,d) 20%, (b,e) 30% and (c,f) 40%. Recrystallization occurs at 900ºC. The major microstructural features remain to be nano-twins in the 20% or 30% deformed samples, while the major part of the samples is recrystallized in the 40% deformed specimens after 900ºC heat treatment.

Figure 24 Bright field TEM image collage of the 316 SS specimen deformed to 30% tensile strain and annealed at 900ºC for 1 hr. The recrystallization starts from the intersection of two different twin variants.

In situ TEM heating experiments were performed to study the microstructure evolution in situ, in particular the thermal stability of deformation nano-twins in tension samples. Figure25-a reveals that there are nano-twin bands and high density of dislocations in the 20% deformed samples at room temperature. The inserted SADP shows these twins are {111}<112> type. Figure 25-b shows the dark field image of these nano twin bands. As the temperature increased, the dislocations disappeared gradually, but

nano-twins were stable up to 900ºC (Figure 25-c). At 1000ºC, disintegration of the thin foil started at the thinnest area near the hole of the TEM samples, but the nano-twin bands still remained stable (Figure 25-d). At first, it was not possible to find an obvious structure to assess what happens to nano-twin bands at this temperature and whether the detwinning occurs in the twin bands of Figure 25-d. After annealing at 1000ºC for about 30 minutes, a characteristic microstructure appeared, labeled by white arrows in Figure 25-(e, f), which is used as a location mark. Comparing the position of this mark and the twin band in Figure 25-e, the nano-twin band was verified to disappear gradually starting from the lower end of the sample. Nano-twin bands completely disappeared after ~37 minutes at 1000ºC as shown in Figure 25-f. To the best of the author's knowledge this is the first in-situ study that demonstrates how nano-twins disappear during annealing of stainless steels and clearly proves the occurrence of detwinning.

Evolution of Mechanical Properties

Heat treatments (HTs) at temperatures from 500°C to 1200°C were performed for 1 hour on the 20%, 30% and 40% strained tension samples of 316 SS, followed by water quenching. The corresponding hardness evolution at room temperature after HTs is shown in Figure 26-a. Hardness remained unchanged or slightly increased after HTs up to 600°C annealing and dropped slightly from 600°C to 800°C. After annealing above 800°C, a significant softening occurred. At 1000°C, the deformed materials were fully recrystallized and the hardness was comparable to the hardness of the as-received materials. Figure 27 provides a comparison of the tensile true stress-strain responses

between as-received specimen and as annealed samples (800/900 °C HT for 1 hour on the 20%, 30% and 40% pre-strained samples). The tensile curves of the 30%-800°C HT and 40%-800°C HT samples show a significant increase in tensile yield strength (from ~254 MPa to ~570 MPa, also see Figure 26-b) and retention of considerable ductility (about ~35%) as compared to the AR specimens. 900°C HT of the 20%, 30% and 40% pre-strained samples and 800°C HT on the 20% deformed samples present less strengthening, but again a retained ductility. The yield strengths of the specimens after heat treatments are summarized in Figure 26-b and compared with the ultimate tensile strengths of the 20%, 30% and 40% deformed samples such that it is possible to see the level of reduction in strength after the annealing heat treatments. The yield strength of the AR specimen is also included for comparison. After 800°C HT, dislocations are mostly recovered so the hardness and strength decrease slightly. After 900°C HT, the hardness and strength of the 30% and 40% deformed specimens dropped considerably as compared to that of the 20% deformed specimens. However, all the hardness and strength levels of the deformed and annealed samples (after 800 and 900°C HTs) are still higher than those of the as-received sample. From the above results, it can be seen that the deformation and annealing cycles can enhance the strength and ductility property combination in 316 SS samples due to the thermal stability of deformation nano-twins. To illustrate this better and quantity the amount of improvement, 30% tensile strain was applied to an as-received sample (red tension curve in Figure28-a). A post deformation annealing process was carried out at 800°C. The annealed sample was then deformed an additional 30% tensile strain (see the blue tension curve in Figure 28-a), unloaded, and annealed again at 800°C. After this

second annealing, the specimen is pulled to failure (dark green tension curve in Figure 28-a). Comparing the three tension tests, the yield strength is significantly increased from ~254 MPa to ~525 MPa (secondary tension) to 635 MPa (third tension). The 2nd and 3rd tension curves were shifted in order to clearly show the strengthening effect of the anneal-tension cycles on the samples as compared to the as-received sample. The ultimate tensile strength before fracture of the sample after anneal-tension cycles is ~1096 MPa which is higher than the ultimate tensile strength of the as-received sample (~978 MPa).

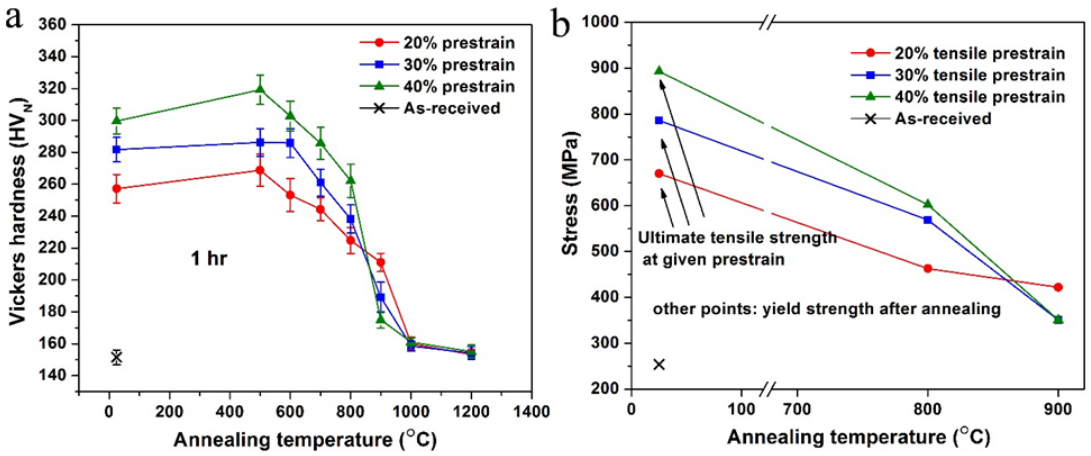

Figure 25 Evolution of Vickers microhardness values (a) and ultimate tensile and yield strengths (b) of various 316 SS samples uniaxially strained to different levels and then, annealed for 1 hour. Softening starts at around 600°C. The hardness drops significantly after annealing above 800°C. At 1000°C, the deformed materials were fully recrystallized and the hardness was comparable to the as-received sample hardness. In (b) the ultimate tensile strength of 20%, 30% and 40% is included for comparison.

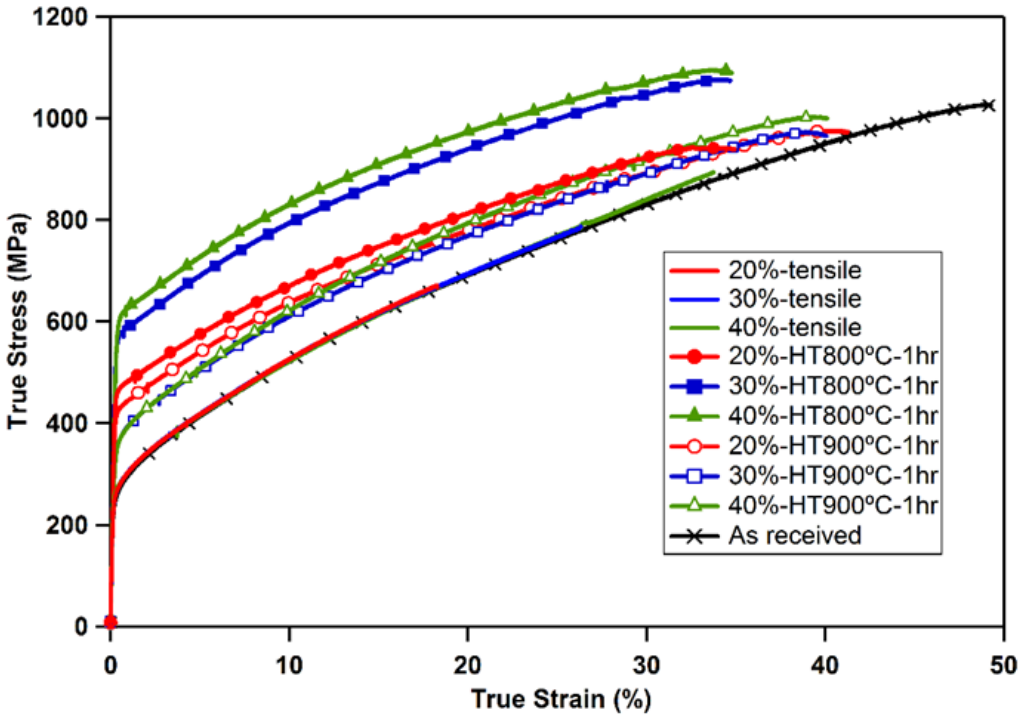

Figure 26 Tensile true stress-strain responses of the as-annealed 316 SS tension samples after various levels of tensile strain. The tensile response of the as-received sample is included for comparison. The marks on the plots were added to distinguish different cases. They do not represent experimental data points.

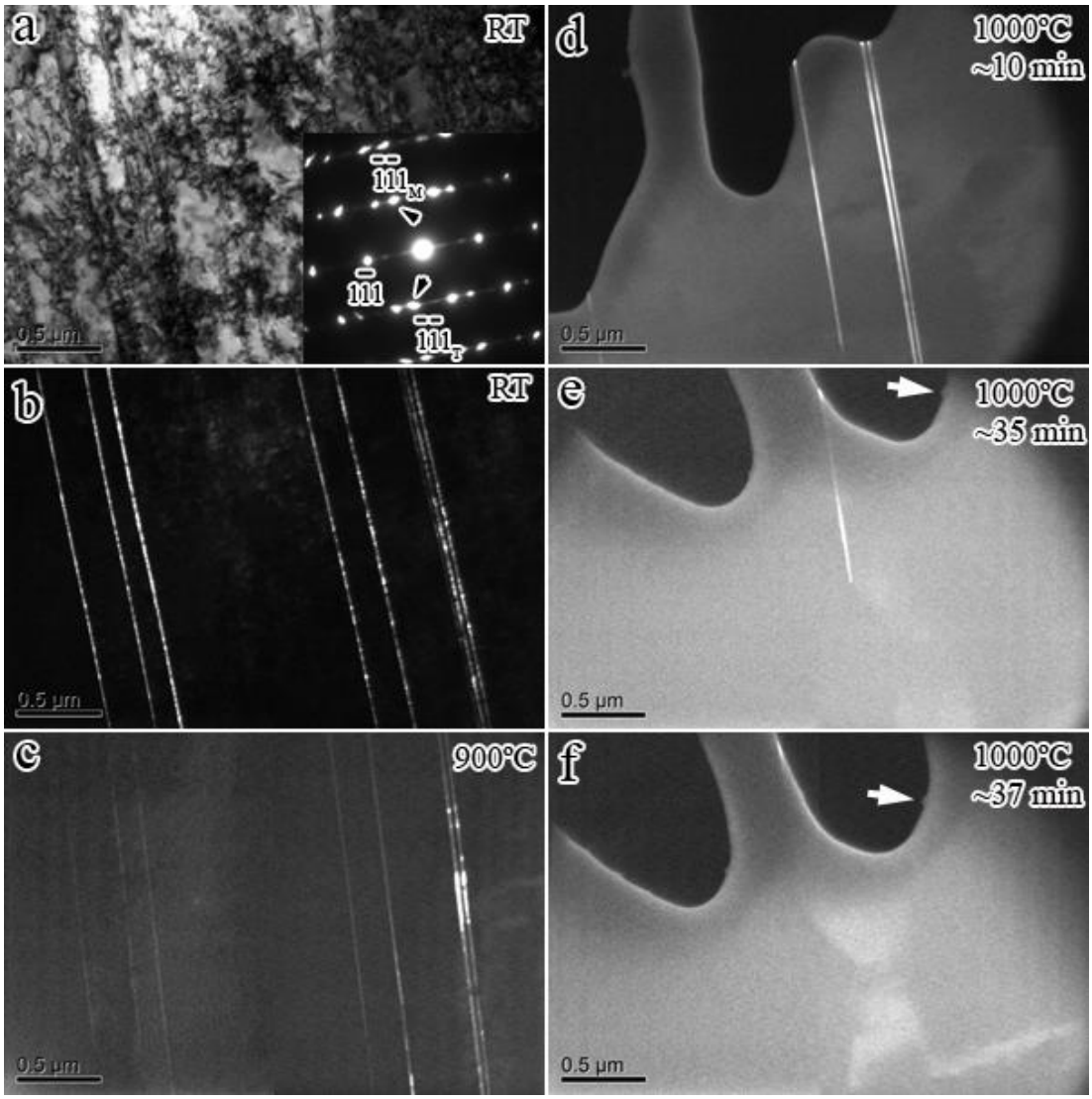

Figure 27 Microstructure evolution under in-situ TEM HT on the 20% deformed sample of 316 SS. (a, b) Bright and dark field images at RT, respectively; (c) dark field images after heating up to 900 ºC, heating up to 1000 ºC and holding temperature for (d) ~10 minutes, (e) ~35 minutes and (f) ~37 minutes.

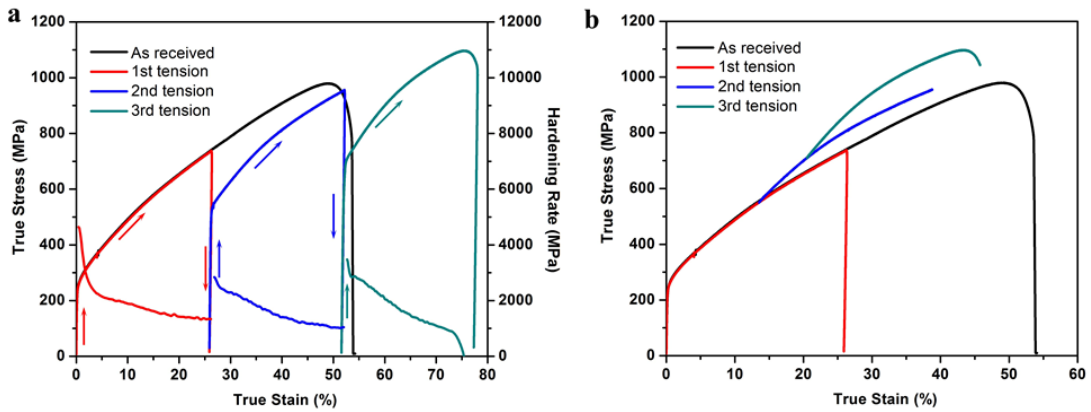

Figure 28 Tensile true stress-strain curves of (a) the 316 SS samples after deformation-annealing-deformation cycles. (b) The 2nd and 3rd tension curves were shifted in order to clearly show the strengthening effect of the anneal-tension cycles samples comparing to the as-received sample. Please see text for details.

Hierarchical Microstructure Evolution Under Different Strain Levels

Microstructural evolution in the samples after 20%, 30% and 40% tensile strains are shown in Figure 29. Numerous parallel bands were formed in most grains at each strain level. These bands were shown to be {111} <112> twin bands via the TEM investigations. Before mechanical twinning was activated, the dislocation slip was the dominant deformation mechanism, and a high density of planar dislocations was generated under 10% strain deformation as shown in Figure 21-a. The formation of planar dislocations can reduce the ability of a material to cross-slip and cause the early onset of twinning. Figure 29-(a_1, b_1 and c_1) show the low magnification SEM images of the microstructures after 20%, 30% and 40% strains, respectively. It is obvious that at 20% elongation, straight deformation twins are already present in more than ~50% of the grains (Figure29-a_1). Generally, only one twinning system was activated in most of the twinned grains which is also evidenced by the TEM image (Figure 21-b), but their volume fraction in each grain

is relatively low. The number density of the twinned grains is estimated as 62.6% ± 4.6% of total grains, determined by counting about 500 grains. The density of twins in every twinned grain is depicted for the 20% deformed samples in Figure 30, the average value is ~6.6% ± 4.7%, calculated using ~70 grains. At a higher strain level, i.e. 30% or 40%, in most of the grains, a second twinning system was activated. There are more interactions between these two twinning systems in the 40% deformed specimens as compared to the 30% deformed specimens as can be seen in Figure 29. The twinned-grain number fractions of the 30% and 40% deformed samples are determined as 77.3% ± 3.1% and 79.5% ± 4.3%, respectively, from about 500 grains, which are close to each other but larger than that of 20% strain sample. However, the twin densities in single twinned grains present a large difference between 30% and 40% deformed samples, as shown in the histograms of Figure 30. The twin density increases from ~11.0% ± 7.3% to 16.2% ± 6.8% with increasing strain level from 30% to 40%. This reveals that the twinning activity is enhanced as the tensile strain increases from 10% to 40%. The measured twin densities are also summarized in Table 2. The twin density in the entire sample is also measured using a total of about 500 grains. The total twin densities in each of the 20%, 30% and 40% deformed samples are determined to be 5.8% ± 1.5%, 9.4% ± 1.6% and 12.5% ± 2.0%. In the 30% deformed sample after the deformation-annealing-deformation cycles, the twinning is activated in almost every grain after the third tensile loading (Figure 28). The final twin density reaches to ~28.4% ± 4.5% which is much higher than 12.5% ± 2.0% of the 40% deformed sample. This shows that the deformation-annealing-deformation cycles can efficiently increase the twin density in 316 SS.

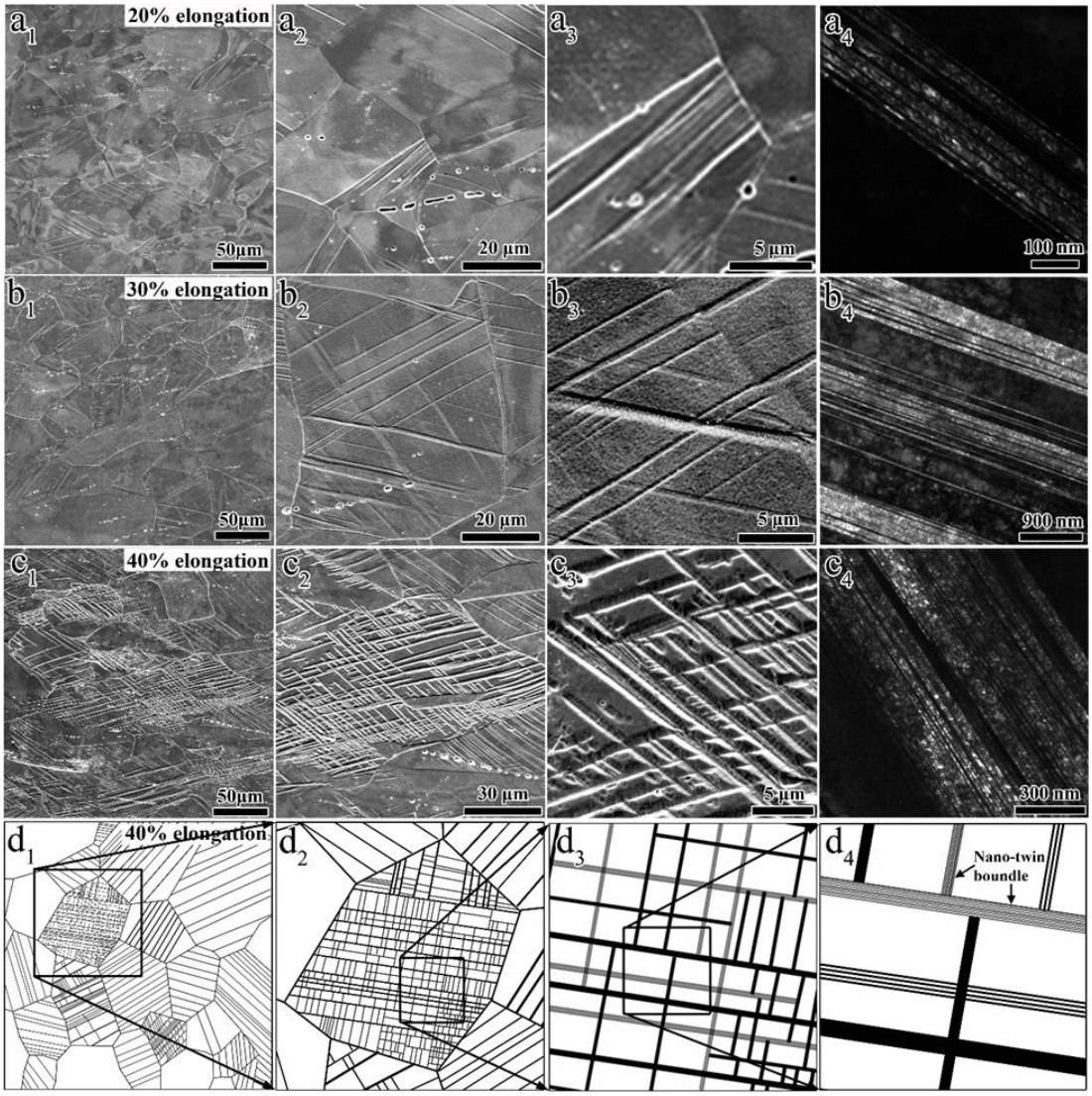

Figure 29 Hierarchical microstructure evolution of 316 SS under a uniform elongation of (a1-a4) 20%, (b1-b4) 30% and (c_1-c_4) 40%. (d_1-d_4) are the schematic representation of these microstructures for the 40% deformed case. The volume fraction of the twinned grains increased with increasing strain level. The volume fractions of twins in individual grains increase correspondingly as well.

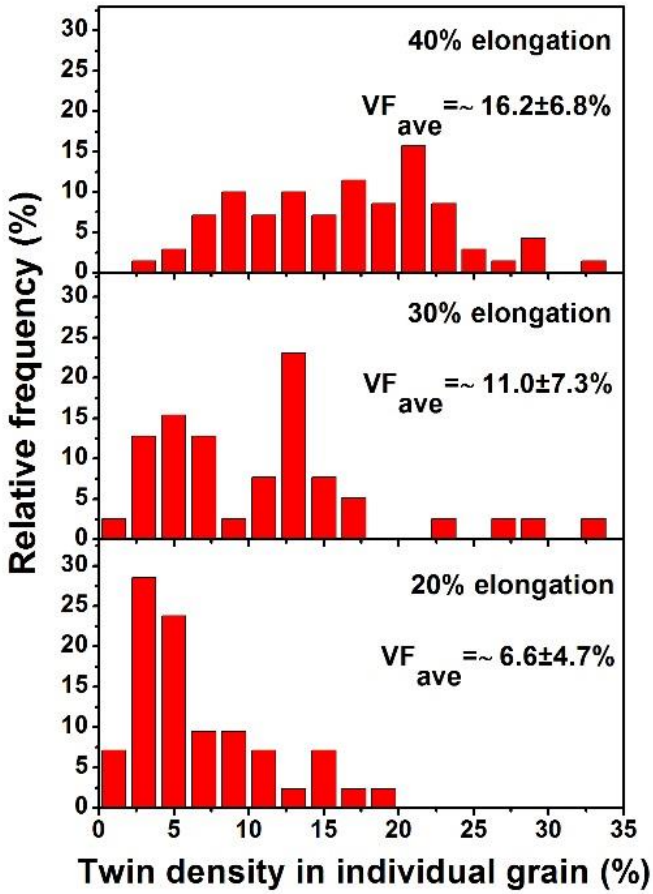

Figure 30 Distribution of twin density within individual grains after tensile deformation to different levels. The average density of twins increases from ~6.6% ± 4.7% to ~16.2% ± 6.8% with increasing strain levels from 20% to 40%, determined from about 70 grains. The maximum twin density in an individual grain was estimated to be around ~33%, which points out the upper limit for the twin density that can be achieved via uniaxial tension deformation.

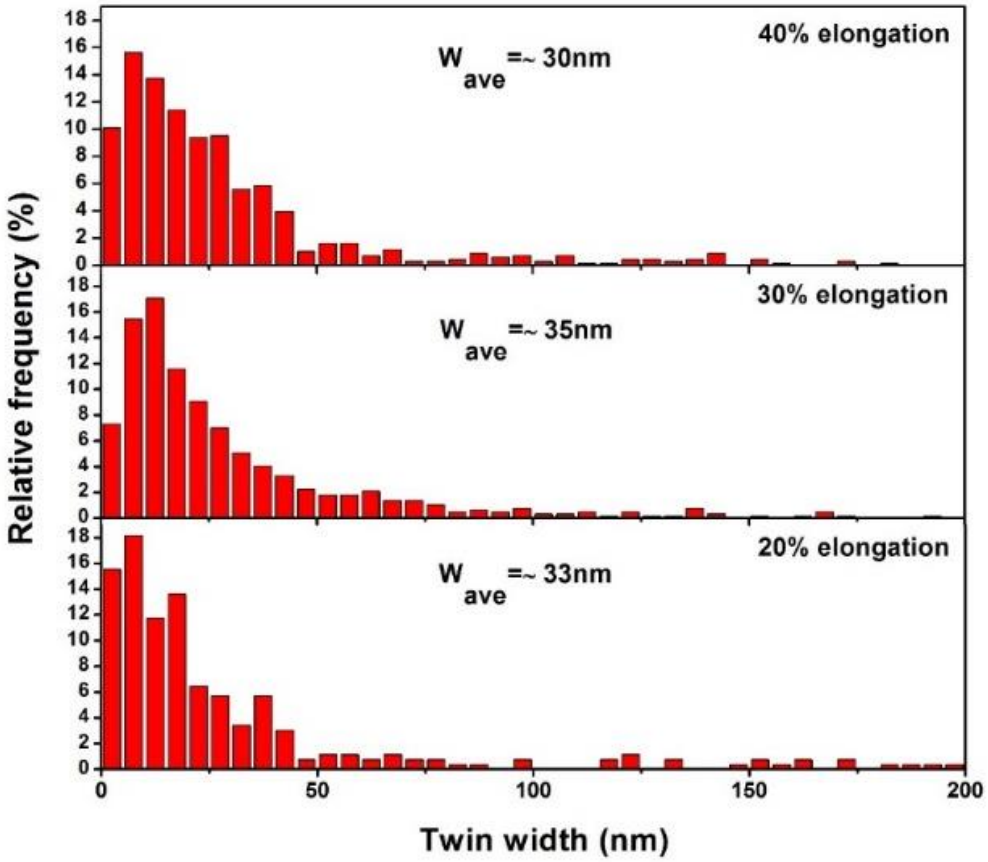

Figure 31 Distribution of the twin width in the tensile deformed 316 SS. Compared to the twin density, the change of twin size with increasing uniaxial strain level was insignificant. More than ~700 twin bands were counted at their edge-on condition in dark filed TEM images.

Table 2 The measured deformation twin densities as a function of applied strain for 316 SS samples deformed under tension to different strain levels.

	Number Density of Twinned Grains (%, from ~500 grains)	Twin Volume Fraction in each Twinned Grain (%, from ~70 Grains)	Twin volume fraction in the Entire Sample (%, from ~500 grains)
20%	62.6 ± 4.6	6.6 ± 4.7	5.8 ±1.5
30%	77.3 ± 3.1	11.0 ± 7.3	9.4 ± 1.6
40%	79.5 ± 4.3	16.2 ± 6.8	12.5 ± 2.0
30% cycles	~ 100%	27.0 ± 6.6	28.4 ± 4.5

In Figure 29- (a_2, b_2 and c_2), a single grain is selected to show the twin morphology at each strain level. It is obvious that within a single grain, the twin band density increases with increasing strain. The maximum twin density in an individual grain was estimated to be around 33% for both 30% and 40% strain, which indicates the approximate upper limit of deformation twin density achieved via uniaxial tensile deformation at room temperature. Figure 29 (a_3, b_3 and c_3) present the submicron scale details of twin bands and their interactions at each strain level. The TEM images shown in Figure 29-(a_4, b_4 and c_4) indicate that the bands seen at submicron scale in SEM images are actually bundles of nano-twins, which are similar to nano-twin bundles shown earlier in 316L austenitic stainless steel after dynamic plastic deformation [60]. These nano scale twin bundles with a high density of parallel twin boundaries are difficult to be traversed by another twin band or bundle. Therefore, there are many bands or twin bundles stopped at one side of another twin bundle. Thin twins and twin bundles are common features of low SFE austenitic

steels, and these microstructures significantly contribute to work hardening [30, 31, 109, 110]. Figure 29-(d_1-d_4) are the schematic representations of the hierarchical morphology of the deformation twins 316 SS. These schematics clearly show the details of twin bands or bundles and their interactions after uniaxial tensile deformation. Furthermore, with the help of dark field (DF) images of twin bands, the twin width is statistically measured as summarized in Figure 31. The average twin widths are on the order of 30-35 nm for all three samples determined by measuring more than 700 nano twin bands at their edge-on condition in DF TEM images. Compared to the twin density, the changes in twin width at different strain levels are insignificant. A previous study demonstrated that twin thickness is dependent on SFE, strain rate, and deformation temperature [111]. Low SFE, high strain rates, and low temperatures were shown to effectively reduce the critical twin nucleus thickness and resist the propagation of twins, resulting in finer deformation twins. Under a strain as high as 116% during equal channel angular extrusion of 316L SS [30], the average twin thickness was about 35 nm which is comparable to that in the present work. This reveals that twin thickness is independent of the extent of deformation. It is well known that martensitic transformation can be induced under plastic deformation at low temperatures in many austenitic stainless steels [112-115]. Seetharaman and Krishnan [116] reported, in 316 SS, a considerable amount of martensite (around 30% vol.%) formed under ~30% true strain uniaxial tension and rolling at -196 °C. However, after the deformation at 25 °C, very little martensite was noticed even at very large strains. In the current work, martensite phase was absent in the uniaxial tension deformed samples verified using TEM and XRD.

Thermal Stability of Deformation Nano-Twins

The thermal stability of deformation twins at elevated temperatures is not well-known, compared with the nucleation and growth mechanisms of deformation twins. Nano scale deformation twins and twin bundles were reported to form during equal channel angular extrusion in 316L SS at temperatures as high as 800°C (0.6 Tm, Tm is the melting temperature in K) [30]. The nano-twins in Cu and 330 SS films were shown to exhibit notable thermal stability. Nano twins remained stable at 800°C (0.79 T_m) in Cu and 500°C in 330 SS films, respectively [107]. In the present study, it's revealed that the nano twins in deformed 316 SS materials can be stable up to 800°C (0.6 T_m), and no detectable coarsening of the nano twins was observed in TEM investigations under edge-on conditions for the twin boundaries. At 800°C heat treatment for 1 hour, recrystallization was not observed in any of the 20%, 30% and 40% deformed samples, but the dislocation density obviously decreased compared with the corresponding as-deformed samples. Due to the higher density of twin bands under higher strain, the yield strength of the post annealed 40% deformed samples is higher than that of the post annealed 20% and 30% deformed samples (shown in Figure 26-b). However, recrystallization starts at 900°C heat treatment for 1 hour (shown in Figure 23). Even though primary recrystallization was locally initiated at 900°C heat treatment, the deformation twins were maintained in the microstructure unless they were consumed by the growth of the recrystallized grains into the deformed matrix, as illustrated in Figure 24. The deformation twins were found to be thermally stable in the non-recrystallization zone even at 900°C heat treatment (see Figure 23-f, 24 and 25-c). In addition, based on the in-situ TEM heating experiments, the nano

twins are clearly stable at 900°C, as no coarsening and detwinning were discerned. The temperature of the heating stage (Model 628-0500) used in these experiments was determined to be accurate to within a few degrees. However, there is greater uncertainty about the actual temperature at the observation location because the thermocouple mounted on the heating stage is not directly contact with specimen. The temperature obtained by the thermocouple is the furnace temperature and should be considered as the maximum as there was no method for independently determining the actual specimen temperature at the position of observation. Based on the previous investigations in the literature, a 50 °C difference between measured temperature of the holder and actual specimen temperature can be expected [117, 118]. Thus, through the in-situ experiments, it can be confidently stated that deformation nano-twins have remarkable thermal stability at least up to 800°C (0.6 Tm) in 316 SS which is consistent with the ex-situ experiments.

Effect of Thermally Stable Deformation Twins on Post-Annealing Mechanical Response

Following Kocks *et al.* [119, 120], the dynamic evolution of dislocation density can be written as:

$$\frac{d\rho}{d\varepsilon} = \left(\frac{d\rho}{d\varepsilon}\right)_{+} - \left(\frac{d\rho}{d\varepsilon}\right)_{-} = \frac{1}{b\lambda} - k\rho \qquad \textbf{Equation 1}$$

where ρ is the dislocation density, ε is the strain, b is burgers vector, λ is dislocation mean free path, and k is the recovery coefficient. The term $\frac{d\rho}{d\varepsilon}$ is the net dislocation storage rate. The first term $\left(\frac{d\rho}{d\varepsilon}\right)_{+}$ is related to dislocation storage and $\left(\frac{d\rho}{d\varepsilon}\right)_{-}$ is the dislocation dynamic

recovery term. The increase of dislocation density arises from the accumulation of immobile dislocations which are actually the dislocations arrested by strong obstacles. In other words, any obstacles blocking dislocation motion will result in strain hardening. These obstacles could be forest dislocations, grain boundaries, twin boundaries, or precipitation particles. Thus, the dislocation mean free path λ can reflect the strengthening mechanism. A small λ value reflects a quick accumulation of immobile dislocation. Applying the rule of mixture, the dislocation mean free path can be written as [121]:

$$\frac{1}{\lambda} = \frac{1}{d} + K\sqrt{\rho} \qquad \textbf{Equation 2}$$

where *d* is effective grain size, and K is a constant. The second term on the right hand side is related to the forest dislocation spacing. When twinning occurs, the effective size of the twinned grain will decrease significantly. In the present case, the low dislocation density and the large grain size of the as-received material results in a large λ value, thus the low yield strength (shown in Figure 27 black curve). However, dislocation tangles or cells and twinning occur during deformation. Thus the blockage of dislocations by as-formed dislocation tangles and twin boundaries can provide further strengthening of 316 SS and postpone necking, which results in a significant work hardening. The onset of necking in the as-received sample is at ~47% true strain (Figure 27). The annealing of 20%, 30% and 40% deformed specimens reduces the dislocation density, but the twin boundaries survive (due to their thermal stability). Thus the yield strengths of the annealed samples are higher, compared to the as-received case. The hardening behavior of the as-received and 40%-800°C and 40%-900°C are given in Figure 32. The strain hardening rate of 40%-800°C and 40%-900°C samples are clearly higher at a given stress level than the as-received

sample due to the higher density of twin boundaries and the positive influence of twin boundaries in reducing the mean free path of dislocations.

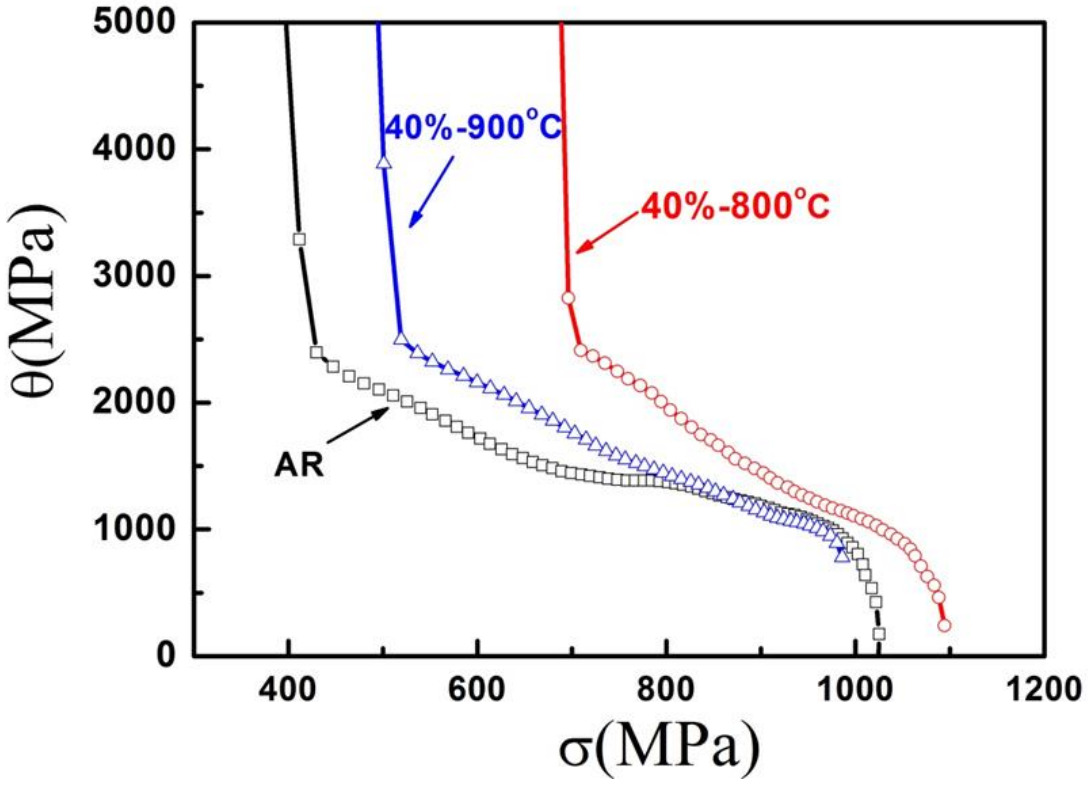

Figure 32 Work-hardening rate (θ) vs. true stress (σ) for the as-received, 40% tensile deformed and 800°C annealed and 40% tensile deformed and 900°C annealed 316 SS samples. The annealing heat treatments were conducted for 1 hour.

Strain hardening rate vs. applied strain response for the as-received material reveals different hardening stages and corresponding microstructure evolution during uniaxial tensile tests. At the initial stages of plastic deformation, the strain hardening is very high and steadily decreases when strain is below ~17% (Figure 32 black square line). The microstructure within this stage reveals a planar arrangement of dislocations

(evidenced by microstructure of 10% deformation sample as shown in Figure21-a) which was noted in previous studies of low SFE materials [109]. With increasing strain, the hardening curve exhibits an almost constant strain hardening rate which is due to twinning. At the onset of this stage, mechanical twinning is activated. Twins can serve as obstacles against dislocation motion. They create a small λ value and thus promote strain hardening. Further straining in this stage is found to produce more twins and twin bundles (Figure29-a_4), and twinned-grain fraction rises from 62.6% ± 4.6% to 77.3% ± 3.1% as true strain increases from 18% to 26% (corresponding to engineering strains from 20% to 30%). After this stage, a second regime of decreasing strain hardening rate appears again when strain is larger than ~27%. Between true strains of 26% and 33% (engineering strain from 30% to 40%), the trend of increase in twinned grain fraction continues but the rate of increase is very low (from 77.3% ± 3.1% to 79.5% ± 4.3%) and twin-twin intersections were observed in this stage. Due to the apparent difficulty of forming more deformation twins with further straining in this stage, the strain hardening rate drops steadily. Figure 33 shows the strength and ductility combination in 316 SS after various processing conditions. For comparison, the data from 316L SS processed by Equal channel angular pressing (ECAP) [31] and dynamic plastic deformation (DPD) [60] were included in Figure 33. Although the strength of 316L SS can be significantly increased by these severe plastic deformation (SPD) methods, the ductility is always sacrificed. The current study illustrates a method which can achieve an excellent ductility with moderate strengthening. This could be applied as a complementary method to SPD and DPD.

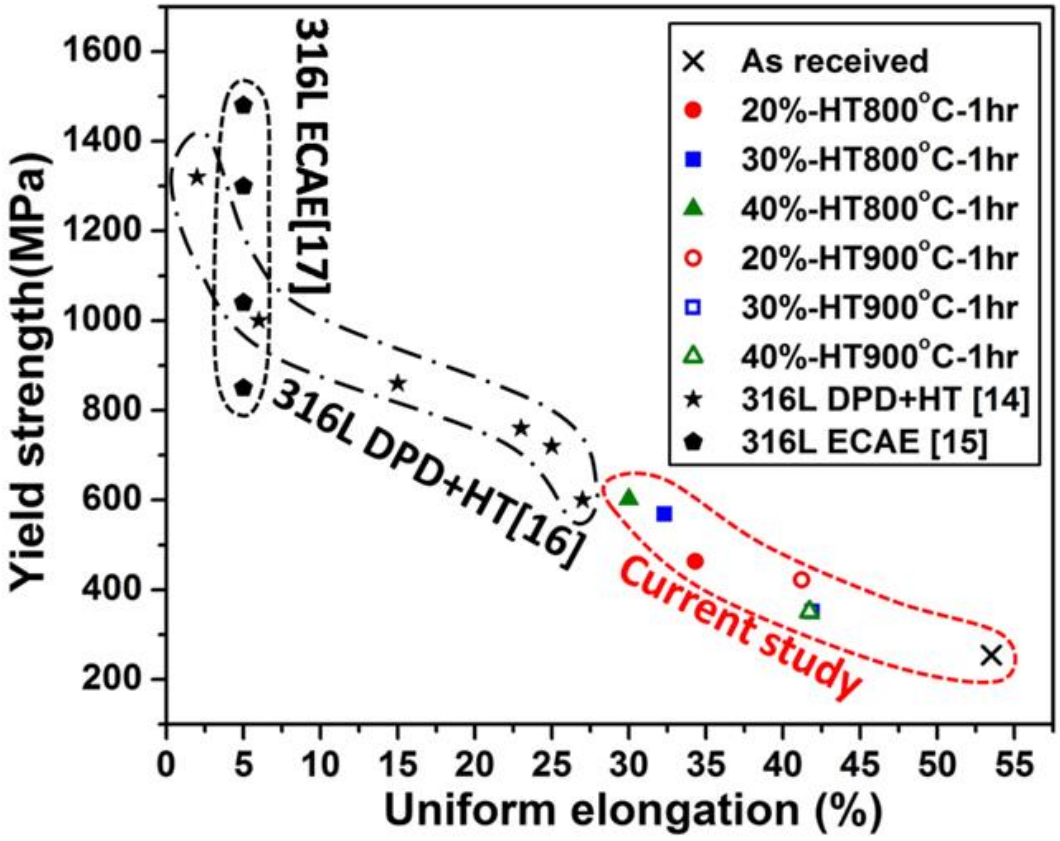

Figure 33 The correlation of yield strength and elongation to failure for the as-received, 20%-800/900°C, 30%-800/900°C and 40%-800/900°C samples of 316 SS samples of the present study. Some literature data for 316L SS [31, 60] are included for comparison.

Summary and Conclusions of Twinning at Room Temperature

In order to investigate the evolution of the deformed structure, 316 stainless steel samples were uniaxially loaded to 10%, 20%, and 30 engineering strains, and studied using detailed quantities SEM and TEM. Deformation features evolve from planar dislocations to single system twinning, then to multi systems twinning and intersections among twin bands or bundles with increase in strain, and with further straining, twin density goes up but twin width remains on the order of ~30 nm. The structure can be

considered to evolve into a hierarchical ensemble of features in different length scales: the nano-scale twins forming sub-micron bundles within micron-scale grains. A series of annealing experiments were performed on the deformed specimens, to evaluate the thermal stability of the deformation twins. TEM studies on the heat-treated samples revealed that after 800°C annealing for 1 hour, the twin density stayed almost at the same level but the dislocation density obviously decreased. Coarsening of the nano twins and recrystallization were not detected in any deformed samples. These nano twins show prominent thermal stability up to ~800°C. Ex-situ heat treatments revealed that at 900°C for 1 hour, recrystallization occurs (from the intersection of two twin variants, if possible) while some nano-twins still remain. Furthermore, in-situ heat treatment in TEM showed the nano-twins start to disappear at 1000°C after some time. Presence of these thermally-stable nano-twins led to a significant increase in tensile yield strength (from ~254 MPa to ~570 MPa) and retention of considerable ductility in the deformed plus annealed samples. After annealing treatments, twin density almost stays the same and the dislocation density drops. Since the dislocation mean free path is reduced due to the twin boundaries, strain hardening is higher at a given stress level due to the better dislocation storage capability. Based on this, a further increased yielding strength was achieved in a deformation-annealing-deformation cycles samples, through maximizing the volume fraction of the twins. The strategy presented in the present work provides a possible method to obtain a high strength for 316 SS without sacrificing ductility.

Role of Thermally-Stable Deformation Twins in High-Temperature Mechanical Response of 316 Austenitic Stainless Steel

In an ultimate motive to increase the operating temperature of working alloys to decrease the CO_2 emission [9, 91], austenitic stainless steels are a good option due to their high-temperature performance (strength, oxidation, creep) [3, 93, 94]. One method to increase the strength of this steel, is creating barriers to dislocation motion through thermo-mechanical processing, and reduce their mean free path, which can lead to high tensile strength and work hardening exponent [78, 83]. One of these barriers can be a twin boundary (created from mechanical deformation or during recrystallization), which is specifically interesting because it is a low-energy, high-angle coincidence site lattice (CSL) boundary [95]. It is believed that since they are high-angle boundaries, they impede with dislocation motion and strengthen the alloy, while they are more stable at higher temperatures due to their lower energy compared to other strength-inducing defects. The purpose of this article is to investigate this belief. In f.c.c. copper, it was found that dislocations can have three distinct interactions with nano-twin bands: slip across twin boundary after pile up, glide in twin or matrix lamellae, or glide of partials parallel to twin boundaries. The dominant mode of interaction mostly depends on the orientation between twin bands and loading direction [122].

Deformation twinning, which is usually in competition with dislocation glide as the dominant deformation mechanism, depends mainly on stacking fault energy (SFE) which is an intrinsic property of the material [96-98]. In austenitic stainless steels, SFE commonly has low to intermediate values, and plastic deformation usually initiates by

dislocation slip, then stacking faults are formed due to formation and separation of dislocation partials, then twinning dominates the deformation [99]. Various deformation methods have created deformation twinning in stainless steels [30, 31, 38, 60, 78, 97, 100, 101]. Nanoscale twins formed by dynamic plastic deformation have been shown to improve the strength of the materials, accompanied with very early necking [105]. The yield strength follows a Hall-Petch relation with the nano-twin thickness [123]. In TWIP steel, through ultra-rapid heat treatment, a nano-twinned structure was created where the twins were stable up to recrystallization temperature (615 °C), after which, the strength dropped noticeably due to recrystallization. Moreover, since the hardening rate in this study appeared to be independent of the heat treatment temperature (as long as it was below 615 °C), it was concluded that the main hardening mechanism is deformation twinning [124]. Grajcar et al. found that the deformation twins formed at higher strain rates have higher dislocation density within twin bands, which leads to higher strength and work hardening exponent [125]. It is known that the ductility decreases as the strength increases, and that this can be reversed to some extent through recovery and recrystallization of the deformed metal. Lu et al. [123] have mentioned that existence of three characteristics in a strength-inducing feature can lead to optimization of strength and ductility: coherency with the matrix, thermal and mechanical stability, and size smaller than 100 nm. Bouaziz et al. [101] discovered that a higher combination of strength-ductility can be achieved through recovery rather than recrystallization in nano-twinned stainless steel. In austenitic stainless steel, it was proposed that thermally stable deformation twins formed during one cycle of deformation-annealing can lead to a nano-

sized structure with high strength without the detrimental effect on strain hardening [106]. Since dislocations can glide along a coherent twin boundary, smaller twin thicknesses may lead to higher ductility [123]. Atomistic calculations showed that the rate of plastic flow is controlled by the rate of slip transfer reactions across twin boundaries [126]. In 316LVM SS, a nanostructure was created through significant plastic deformation followed by annealing under high hydrostatic pressure, and it was discovered that nano-twin and low-angle boundaries has lower mobility during annealing under hydrostatic pressure [127]. More recently in high entropy alloys, the extend of mechanical twinning was found to strongly depend on the orientation of grains, and a mechanism combining early twinning accompanied with multiple-system slip cause higher strength and strain hardening than either multiple-system dislocation slip only or single slip followed by twinning [128]. In medium entropy alloys, nano-twinning was found to be the major reason for enhanced ductility, based on it dislocation storage and resistance to necking capability, especially over high entropy alloys [129].

If deformation twins are to impart strength at high temperatures, they need to be thermally stable. Mechanical twins in conventional Fe-Mn-C steels have been shown to be stable after 1-hour heat treatment at 550 °C [64]. In high-Mn TWIP steels, deformation nano-twins are stable up to recrystallization at 625 °C [38]. Also in Mn austenitic stainless steels, microalloying has stabilized twins [108]. The coherent nano-twins in deposited 330 stainless steel are stable up to 500 °C [107]. In 316L, deformation twins are stable up to 600 °C [106]. Through differential scanning calorimetry (DSC) of high-pressure torsioned (HPT) nanocrystalline 316L SS, El-Tahawy et al. found dislocations are recovered

between ~320 °C to ~470 °C without affecting the average grain size or the phase composition, and α'-martensite in reversed into austenite at ~470 °C to ~680 °C [130]. 316L SS was cold-rolled then heat treated at 750°C for different durations to create a structure of nano-grains and nano-twins surrounded by lamellar coarse grains and recrystallized grains, and an optimal combination of ~1 GPa yield strength and 20% failure elongation was achieved. The martensite that was formed during cold roll (~25% volume fraction) was reversed after the heat treatment. The width of the twin bands formed were no larger than 75 nm, with an average of about 30 nm. Deformed samples showed no tolerance for significant uniform deformation until annealed for at least 10 min [131]. A 316L SS with heterogeneous lamellar structure incorporating nano-sized twin bundles and ultrafine grains showed a good combination of ductility and strength; ductility because of the soft parts of the structure with forest dislocations, and strength because of fine grain size [132]. The nano-twins formed in 316L SS through dynamic plastic deformation were found to have a significant role in increasing the strength and toughness, especially after recovery/recrystallization heat treatment, the crack propagation is limited by the twin bundles since they can deform plastically and absorb energy. Fracture surface analysis shows that fine dimples are formed during failure, and are constricted by twin boundaries, while twin bands are "pulled out" during the fracture from the matrix [133]. In our recent study, we showed that deformation twin bundles ~0.5 μm wide composed of 30 nm twin band, are stable up to 900 °C when recrystallization starts. Then, through cyclic deformation-heat treatment, we increased the volume density of thermally stable deformation twins that survive during a recovery at 800°C. These thermally stable, highly-

twinned structure was found to strengthen the steel without total loss of ductility [134]. Byun et al. [135] studied the mechanical response of different conventional austenitic stainless steels, both annealed and cold worked, at different temperatures in uniaxial tension test, and found that strength and uniform strain decrease with increasing temperature. The hardening rate was found to decrease as strain increased at higher temperatures, but at room temperature and below, an increase in hardening was observed due to formation of martensite. In addition, they found out that the hardening rate and true stress are almost equal at the onset of plastic instability, called this value the plastic instability stress (PIS), and claimed that if the yield strength of cold-worked samples surpassed this PIS of the annealed material, necking occurs right after yielding. The hardening rate at necking was reported to be independent of the microstructure and pre-strain, but sensitive to temperature [135].

More recently, in iron-based superalloys, nano-twins that were formed during a DPD process and survived annealing at 700 °C, were found to both strengthen the structure as well as improve ductility after the annealing due to their reduced dislocation density. The coexistence of nano-twins with γ' nano-precipitates lead to better mechanical response. Using the Bailey-Hirsch formula, and measuring the dislocation density via XRD, they discovered the strengthening by dislocations decreases by almost 100 MPa after aging at 700 °C. The contribution of precipitates after 700 °C aging was found to be 400 MPa. By calculating the contribution of other strengthening mechanisms, they estimated the role of the 50% volume fraction of nano-twins to be around 530 MPa (the most significant contributor), even after the precipitation of γ', which is claimed to be due

to “the structural stability of nano-twins during precipitation”. The work-hardening was also found to increase due to presence of twins, and not a function of dislocation density [136]. In 316L stainless steel, mechanical deformation twins, grain refinement, and strain-induced martensite caused strengthening accompanied with decent ductility, which was contributed to the co-existence of slightly-deformed grains with fine, twinned structure. This structure is believed to give rise to unusual dislocation interactions which leads to evolution of a back-stress field [137].

Experimental Procedure to Design The Thermo-mechanical Process for Increasing Twin Volume Density

The material in this study is a commercial 316 austenitic SS. Initially, forged billets have been considered the as-received condition. Dog-bone shaped tensile specimens were cut from these billets with the gage dimensions of 8 mm × 3 mm × 1 mm using wire electron-discharge machining (EDM). These samples were then heat treated (HT) at 1000 °C for 1 hr, followed by water quenching (WQ), to prepare as-annealed (AA) samples. As presented in the schematic graph in Figure 34, samples from AA condition went through a thermos-mechanical cycling process that consists of two cycles of 30% deformation at room temperature in uniaxial tension, followed by a heat treatment at 800 °C for 1 hr and water quenching. This specific process has been designed to increase the volume fraction of deformation twins in the steel, while decreasing the dislocation density through recovery [134]. Samples after this thermo-mechanical process are highly twinned, and will be referred to as twinned condition (TW). These TW samples, alongside samples from

AA, were then tested in uniaxial tension test until fracture (TTF) at different temperatures. Uniaxial tensile tests were performed on an MTS servo-hydraulic mechanical test frame, with an initial strain rate of 10^{-3} s^{-1}. The temperature was controlled though conduction from heating/cooling the grips; heating by resistive heating-bands, and cooling by passing liquid nitrogen through copper tubing. In order to create a more stabilized atmosphere and temperature, samples were covered in layers of wool glass. The temperature was monitored through thermocouples attached to each grip as well as the center of the tensile samples. Each tension test condition was performed at least 3 times, the median graph was selected to be presented in this work, and values were averaged with standard deviation considerations. Scanning Electron Microscope (SEM) images of the fracture surfaces were performed using a field emission FEI Quanta 600 microscope. Transmission Electron Microscopy (TEM) characterizations were performed using FEI Tecnai G2 F20 microscope operated at 200 kV. The disc specimens for TEM observation were mechanically thinned to >50 μm, and then were prepared using a double-jet electrolytic polishing in a mixture of 10% perchloric acid and 90% ethanol at 20 V and ~-20 °C.

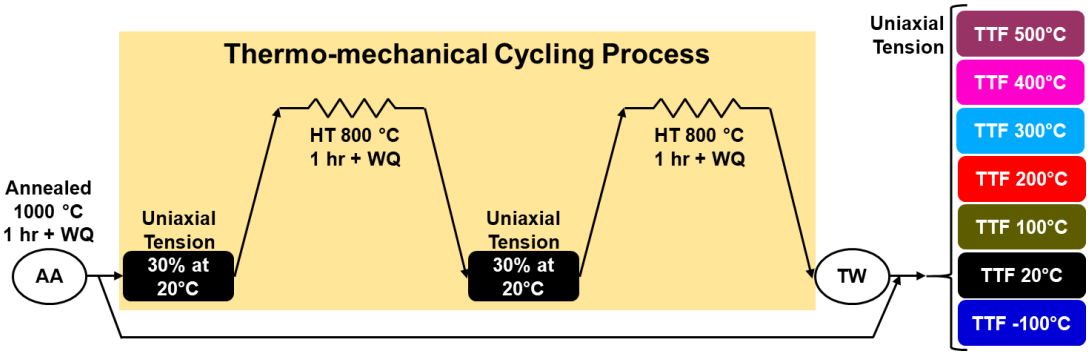

Figure 34 Schematic of the process: several as-annealed (AA) samples went through a thermo-mechanical cycling to create a twinned structure (TW). Both AA and TW samples were tested in uniaxial tension test at different temperatures.

The typical of AA samples and TW samples are depicted in Figure 35. Figure 35-a, shows dog-bone tensile specimen of these two alloys, TW visibly longer than AA. Figure 35-b shows an SEM image of the AA structure, which consists of an equiaxed grains and linear voids that are possibly from the precipitates that exist in this alloy in the form of impurity conclusions. The grain size is ~70 µm. Figure 35-c shows a TEM micrograph of AA and it can be seen that the dislocating density is very low. Figure 35-b, on the other hand, is the SEM image of a TW sample. In this image, it can be seen that the same voids exists, and a structure of elongated grains with almost the same grain size is present. A high volume fraction of surface twins is also visible in this image. Figure 35-c shows the TEM micrograph of this structure accompanied with the related selected area diffraction pattern in Figure 35-f, depicting the presence of twins in an austenitic matrix.

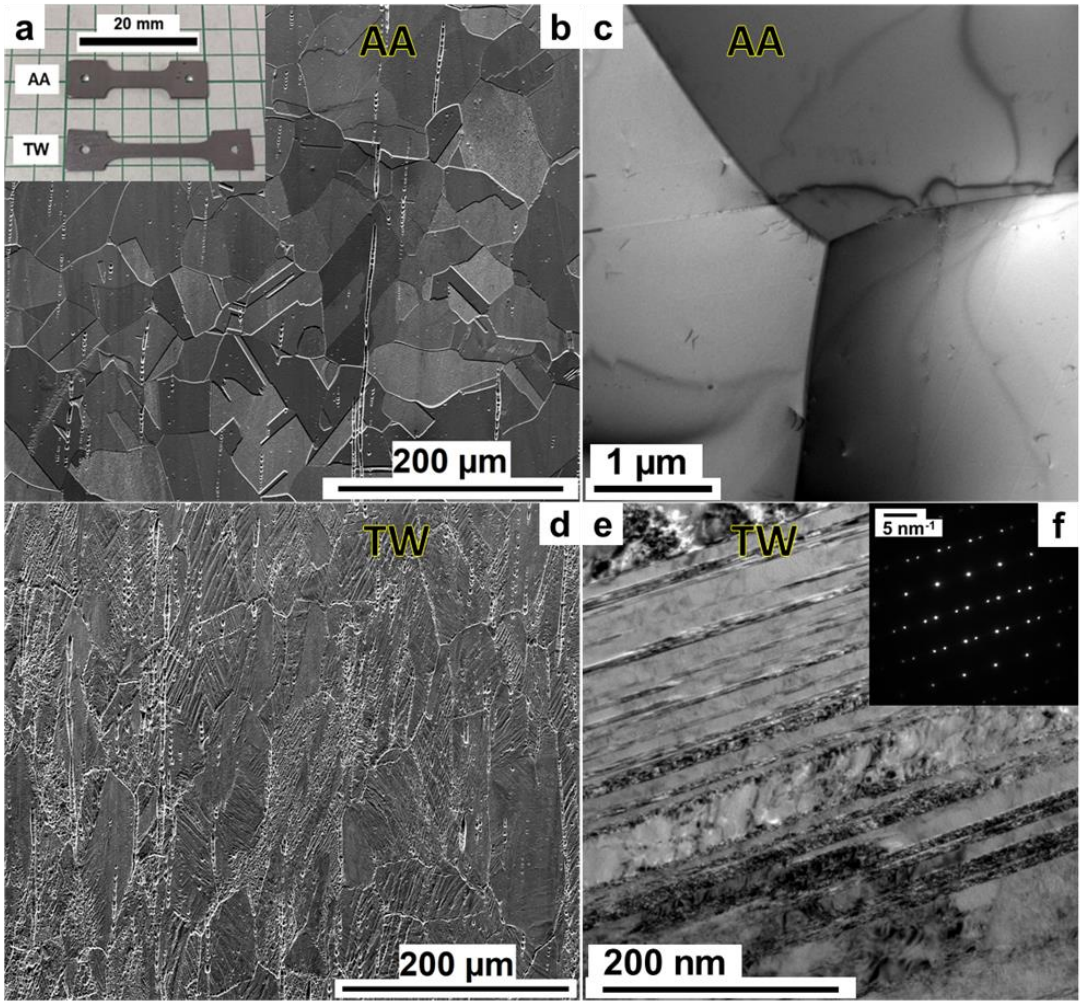

Figure 35 a) tensile dog-boned specimen from as-annealed (AA) and twinned (TW) structure, b) SEM image of AA structure showing large equiaxed grains accompanied with voids from impurities, and c) TEM image of AA showing a very low dislocation density in multiple grains, d) SEM image of TW structure showing elongated grains with almost same grain size as AA and same type of voids plus a high volume fraction of twins, and e) TEM image of TW showing twins accompanied with f) SADF of the twin/matrix structure.

Mechanical Response at -100 °C of Annealed and Twinned Steel

As discussed, tension tests were performed on both AA and TW up to failure at -100 °C and room temperature, and the results are shown in Figure 36. In Figure 36-a, the

true stress vs. true strain is presented. First, it can be seen that as in previous chapter, the TW structure has higher yield strength compared to the AA, at room temperature, as well as lower ductility. At -100 °C, the same trend exists but with yield strength values higher than those at room temperature. The values are presented in Figure 37-a. The increase in yield strength at both temperatures is due to TW structure formed during the thermos-mechanical process. Figure 36-b shows the hardening curve of the AA and TW structure at -100 °C, and the trend witnessed is similar to what is witnessed when transformation of austenite to martensite under stress occurs, especially in austenitic steels [135, 138]. This shows that TRIP effect occurs in both AA and TW at lower temperatures. This TRIP effect is probably the reason for increased ductility of both AA and TW at this temperature. It is also the reason that the UTS of AA is almost as high as that of TW, as shown in Figure 37-b. It is interesting that the TW structure also shows TRIP effect despite the presence of nano-twins and dislocations. It is also witnessed that twinning also happens in the AA samples at -100 °C. Figure 36-c and d show the TEM image of the AA sample after test at -100 °C, where a structure consisting of twins and martensite packets are observed. In Figure 36-e to g, twin bands from the thermo-mechanical process is observed, alongside small martensite packets.

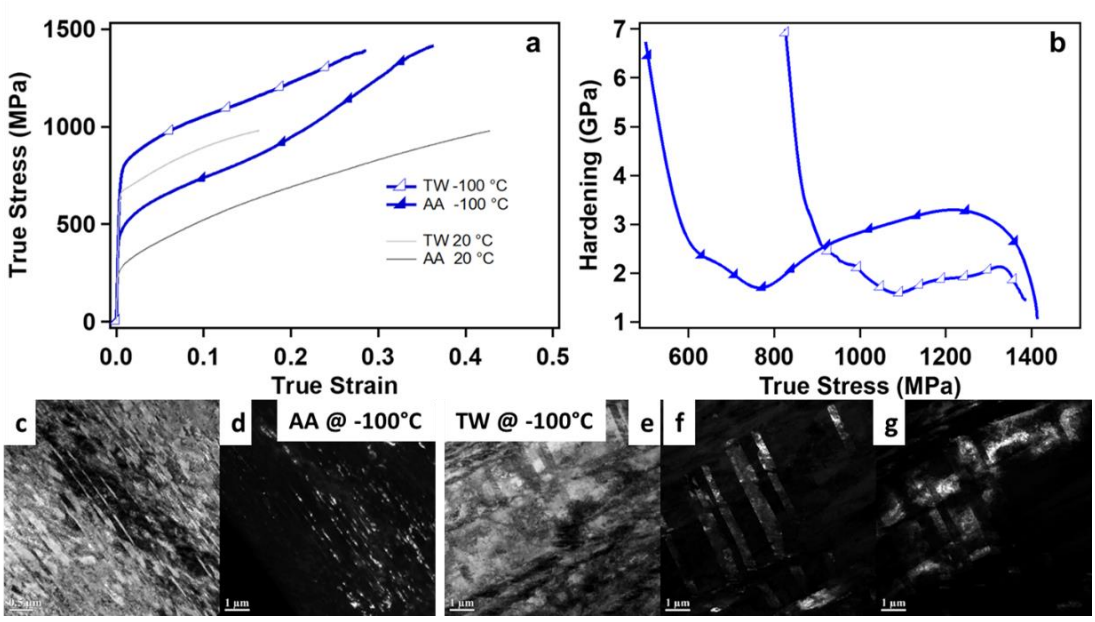

Figure 36 a) True stress vs. true strain of tension tests of AA and TW at room temperature and -100 °C, b) hardening (dσ/dε) vs. true strain of tests at -100 °C showing TRIP effect, c) TEM bright field of AA samples tested at -100 °C with d) dark field of the twin bands, and e) TEM bright field of TW samples tested at -100 °C with f and g) two twin systems.

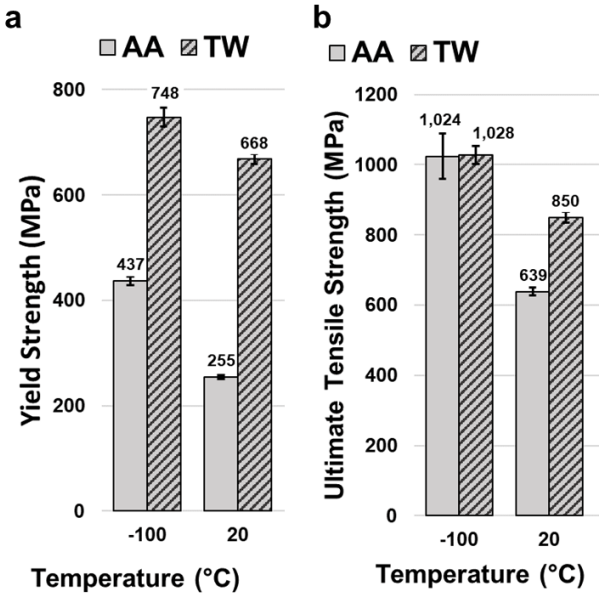

Figure 37 a) Yield strength values for AA and TW at room temperature and -100 °C, b) Ultimate tensile strength of AA and TW at room temperature as well as -100 °C.

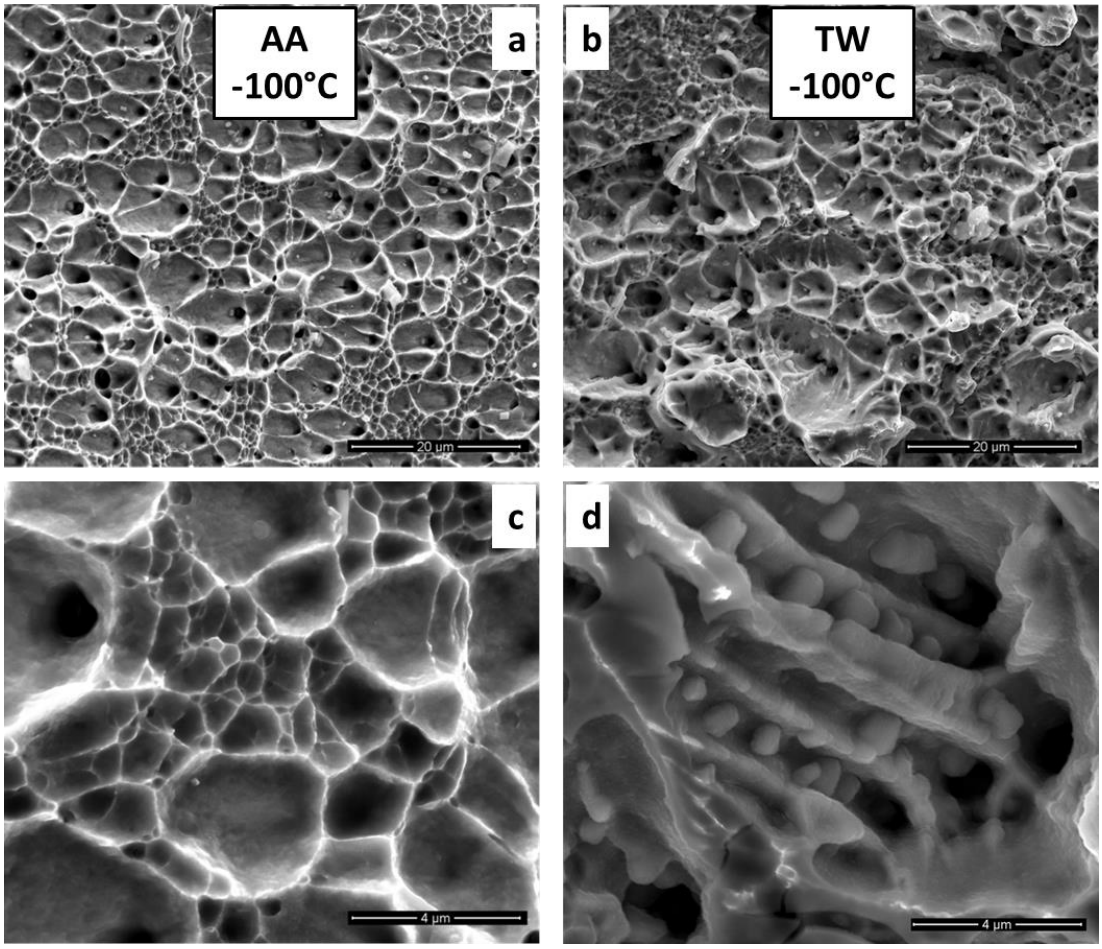

Figure 38 Fracture surfaces after tension tests at -100 °C for a) AA and b) TW and the same at higher magnification c) and d). The fracture surfaces suggest both failures mechanisms were similar.

Figure 38 shows the fracture surfaces of AA and TW samples after tension tests at -100 °C. Comparing Figure 38-a with b, it can be speculated that the fracture mechanisms are similar for AA and TW. Both samples show signs of void formation and coalescence. However, it can be said that the AA sample has a surface with dimples with two significant sizes, as better shown in Figure 38-c. The TW fracture surface has unusual voids on the

surface, as shown in Figure 38-d, which could be due to presence of twins and formation of martensite during tension at -100 °C.

Mechanical Response at Elevated Temperatures of Annealed and Twinned Steel

The mechanical response of the as-annealed samples (AA) and twinned samples (TW) after uniaxial tension test until fracture is presented in Figure 39. Figure 39-(a) shows the engineering stress (*s*) vs. engineering strain (*e*) of the AA samples. Similarly, Figure 39-(b) is the engineering stress (in MPa) vs. engineering strain of the TW samples. Both of these figures are drawn to the same scale, for comparison. The yield strength (YS) and ultimate tensile strength (UTS) values from these tests are reported in Figure 40-(a) and Figure 40-(b), respectively.

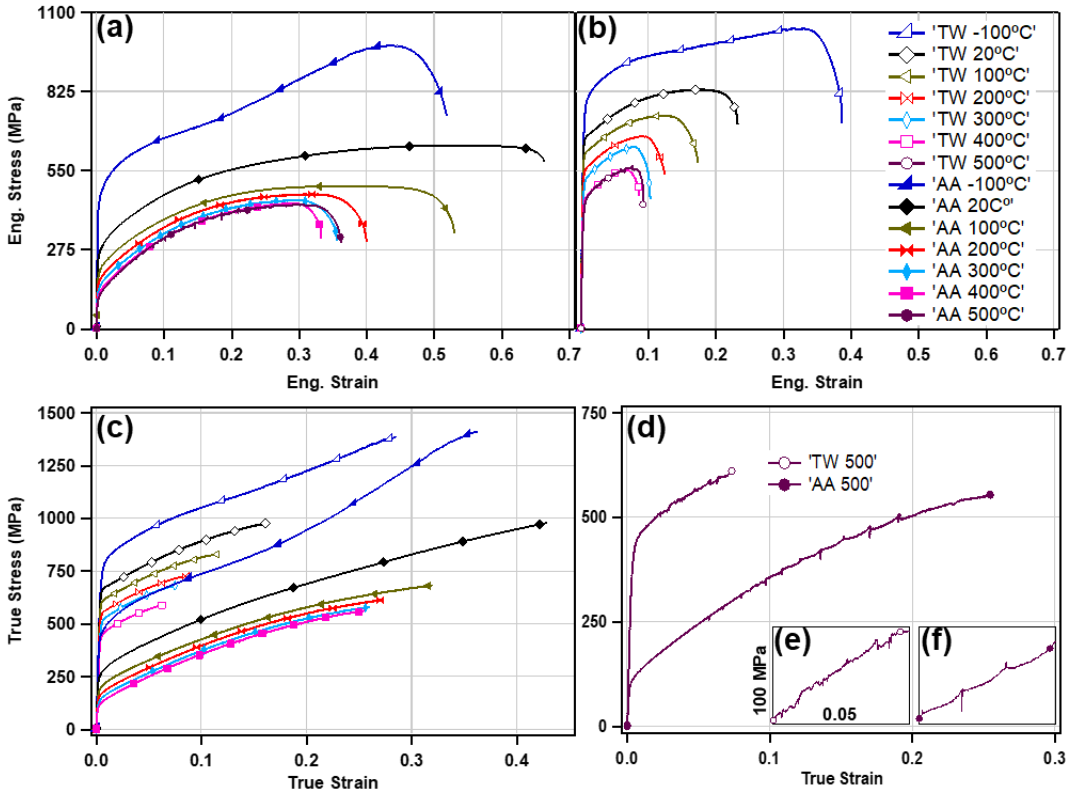

Figure 39 a) Engineering stress vs. engineering strain at extreme temperatures for AA, and b) for TW, c) the true stress vs. true strain of AA and TW at extreme temperatures excluding 500 °C, d) true stress vs. true strain of AA and TW at 500 °C with a magnification of the serrations shown in e) and f).

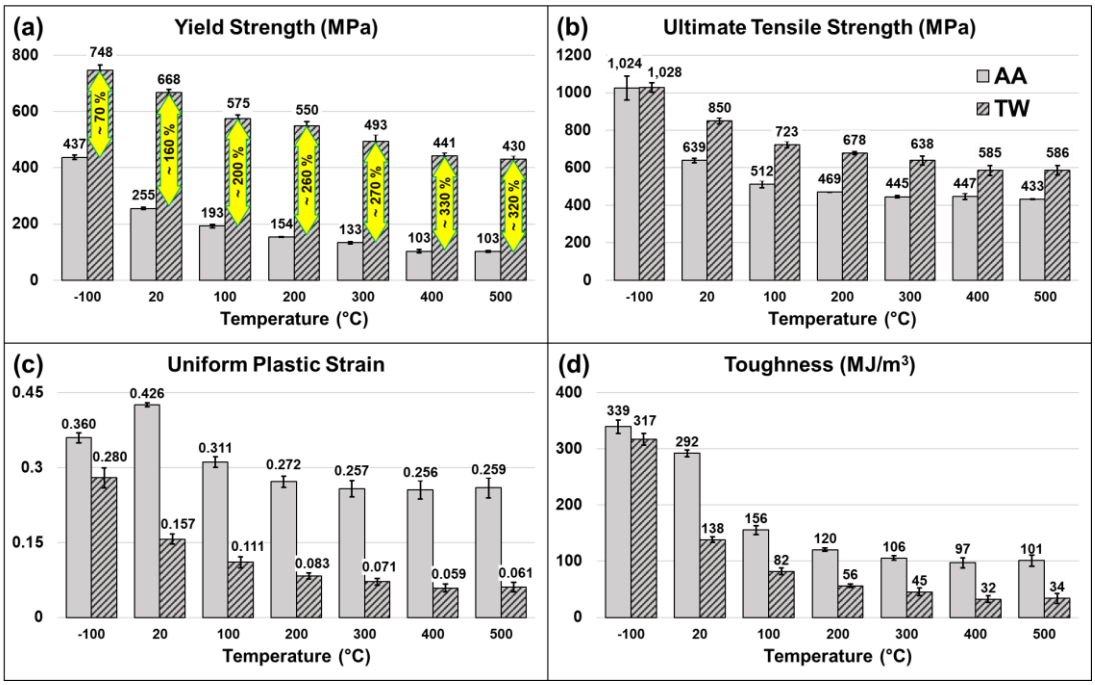

Figure 40 Results of tension tests of AA and TW at extreme temperatures, showing a) yield strength, b) ultimate tensile strength, c) uniform plastic strain, and d) toughness.

It can be seen that, as a general trend, YS decreased by increasing the temperature. This trend, however, is different in AA compared to TW. In AA, a noticeable drop from -100 °C to 25 °C occurs: almost 40% decrease in YS. The decline in YS continues as temperature is increased up to 400°C. For 500 °C, the YS is almost equal to that of 400 °C (~100 MPa). As a matter of fact, their corresponding *s-e* graphs overlap almost perfectly, as seen in Figure 39-(a). Totally, the yield strength of AA drops by ~75% as the temperature is increased from -100 °C to 500 °C. In TW, on the other hand, the initial drop of YS is not that noticeable, almost 10% decrease in YS from -100 °C to 20 °C (vs. 40% of AA). As temperature is further increased, the YS keeps decreasing similar to AA, but not as rapidly. A total decrease of ~40% is witnessed in the yield strength of TW as the

temperature goes from -100 °C to 500 °C (vs. 75% of AA). Therefore, it can be said that the thermally stable twins in TW increase the thermal resistance of the yield strength. In other words, all other factors being the same, the hierarchical structure makes the steel stronger against increasing the temperature. It is notable that the proposed thermo-mechanical process causes a ~70% increase in YS at -100 °C, and a ~160% increase at 20 °C, which continuously soars up to ~320% at 500 °C, as shown by the arrows in Figure 40-(a). The increase in yield strength caused by the process is due to three contributions: a shorter effective grain size because of presence of twin boundaries, a higher dislocation density because not all the dislocations were recovered during the recovery HT (1 hr at 800 °C), and the changes in the texture as result of 30% deformation at room temperature twice. This can be presented as:

$$\uparrow YS|_{T}^{AA\rightarrow TW} = \Delta(k.d^{-n}) + \Delta(\alpha.\mu.b\sqrt{\rho}) + \Delta(\bar{M}\tau) \qquad \textbf{Equation 3}$$

where $\uparrow YS|_{T}^{AA\rightarrow TW}$ is the increase in yield strength due to thermo-mechanical process at each temperature, $\Delta(k.d^{-n})$ is the Hall-Petch change due to decrease in effective grain size based on the presence of twins, $\Delta(\alpha.\mu.b\sqrt{\rho})$ is the increase in dislocation density, and $\Delta(\bar{M}\tau)$ is the change in texture of the sample, k is the strengthening coefficient from the Hall-Petch equation, d is the effective grain size, α is a proportion constant, μ is shear modulus, b is Burgers vector, and ρ is dislocation density, $\bar{M}$ is the Taylor's factor depicting texture, and τ is critical resolved shear stress. This equation basically models the yellow arrows in Figure 40-a. More importantly, based on this model, we can see why this twinned, hierarchical structure is resistant against increase in temperature in terms of yield strength. In the last term (concerning texture), Taylor's factor in is independent of

the temperature where the test was performed; it's only due to the texture created in the steel due to the thermomechanical process. Also in this term, the critical resolved shear stress decreases as the temperature is increased. Similarly in the second to last term (concerning dislocation density), shear modulus decreases as temperature is increased. Dislocation density is also expected to decrease at higher temperatures due to recovery. Burgers vector magnitude may increase due to volume expansion as temperature is increased, but is expected to be negligible compared to other factors. As a result, it can be stated that the increase in yield strength in the TW structure, and the fact that this increase is resistant against increase in temperature (rises from 160% at 20 °C to 320% at 500 °C), is mainly due the effective decreased in grain size which leads to a Hall-Petch increase in the flow stress. In other words, the proposed thermo-mechanical process in this work can strengthen a structural alloy against elevated temperatures.

As for the ultimate tensile strength (UTS), the details of which are provided in Figure 40-(b), it can be seen that, except the case of -100 °C which will be discussed later, a general and reasonable decrease in is strength is present as the temperature is increased. It can be said that increasing the temperature from 20 °C to 500 °C causes the UTS to drop by ~30% for both AA and TW. On average, an increase of 30-35% in UTS is observed as a result of thermally stable deformation twins. Another interesting fact about these graphs is the hardening behavior of the samples tested at -100°C, can be related to martensitic transformation.

True stress (σ) and true strain (ε) values of the tests were calculated and plotted and shown in Figure 39-(c). For ease of comparison, all AA and TW plots are shown in

the same graph, except those at 500 °C, which overlap the corresponding curves at 400 °C. The σ-ε curves of AA and TW at 500 °C are shown separately in Figure 37-(d). As it can be seen from these graphs, the proposed thermo-mechanical process increases the strength of the steel without a total loss of ductility. This is achieved through creating thermally stable deformation twins that impede with dislocation glide, while partly recovering the dislocations during heat treatment. Moreover, twin boundaries, based on their type of reactions with the dislocations (emitting sessile/ glissile dislocations or glide along the twin boundary) are better in maintaining ductility compared to regular grain boundaries [62, 83, 123, 126, 139]. The uniform plastic strain (ε_p^u), calculated as true strain up to necking minus the elastic region, is reported in Figure 40-(c). It is observed that, excluding AA at -100°C, as the temperature increases, the ε_p^u decrease rapidly at first, then slowly, until it reaches an almost constant value. This decrease is simply because the geometrical instability (necking) occurs sooner at higher temperatures. Increasing the temperature from 20 °C to 500 °C causes a drop of ~40% and ~60% in ε_p^u for AA and TW respectively. On average, introducing the deformation twins in the matrix, causes a decrease of ~70% in the ε_p^u. Keep in mind that this decrease in TW means necking occurs sooner, partly because the stress at the onset of necking is 30-35% higher than that of AA. It is interesting that, despite the increase in strength and decrease in ε_p^u, TW samples still show considerable measures of ductility after yielding, considering it has been reported that in conventional austenitic stainless steels, annealed and cold-worked then tested at different temperatures, “the cold-worked specimens failed by prompt necking at yield when the yield stress reached the PIS [plastic instability stress] of annealed material”

[135]. In other words, in tension tests at temperatures above 100 °C, since the yield strength of cold-worked 316LN reaches (and theoretically tends to be larger than) the true stress at the onset of necking of annealed 316LN, the cold-worked samples neck right after yield. While it can be seen that in the results obtained here, TW samples have a higher yield value that the UTS values of the AA in the corresponding temperatures, up to 300 °C. Moreover, above this temperature, TW samples still show significant uniform plastic deformation even after their flow stress passes the maximum true stress on the AA sample at the same temperature. For example, at 200 °C, the AA necks at around 615 MPa, TW at 200 °C shows at least 6% strain after surpassing 615 MPa. This interesting feature of this unique TW structure could be explained through the nano-scale size of the twins as well as their coherency with the boundary. As explained by Lu et al. [123], if a feature exists in the structure which can act as a strength inducing operator (e.g. in this work twins) has the following three characteristics, it can lead to an optimized combination of strength and ductility. These features are: 1. coherency with the matrix, 2. thermal and mechanical stability, and 3. sizes smaller than 100nm. All of these characteristics are believed to present in the thermally-stable deformation twins created by the thermos-mechanical process in this work. To complete this analysis, the toughness (a measure of energy absorbed during plastic deformation) was calculated by measuring the area under the plastic region of σ-ε curves, and reported in Figure 40-(d). The toughness continuously decreases as the temperature is increased, simply because both strength and uniform plastic strain of the steel decreases, especially in uniaxial tension test. Except -100 °C which is believed to be TRIP effect, TW samples have almost 50-65% smaller toughness.

The true stress vs. true strain graphs of both AA and TW at 500 °C are presented in Figure 39-(d). Their behavior is very similar to that of their counterparts at 400 °C. The curves at 500 °C, however, start to show serrations which are known to be due to dynamic strain aging (DSA) [140]. At a closer look, as presented in Figure 39-(e) and (f), it can be seen that the serrations seem to be of different types. For the AA, as shown in Figure 39-(e), the serrations appear to be type A, accompanied by type B, as explained by Rodriguez [141]. Type A are repeated rises followed by drops in the σ-ε curve, which correspond to locking of dislocations in the deformation bands that form. Type B appear as oscillations due to discontinuous motion of dislocations in within a band, and usually appear alongside type A with increasing strain. As for TW in Figure 39-(f), the serrations appear less orderly; it is possible to distinguish a pattern of type A underlying, with the presence of type B, and even a general trend that may be considered as type D. Type D serrations are increases in strength followed by plateaus that are believed to be similar to Luders band formations. Similar behavior has been reported in tensile behavior of 316 SS at elevated temperatures, especially when grain size is decreased from 125 μm to 40 μm [141-144]. Since these serrations only appear at higher temperatures, they are unlikely to be due to formation of twins during deformation at such temperatures [145-147]. In this work, we believe that the change in the serration type is not only due to formation twin bundles with nano-twins (and DSA occurs preferably at boundaries at elevated temperatures [148]), but also the hierarchical structure, that creates general length-scales of two very different magnitudes (one in μm between bundles and GBs, one in nm between nan-twin bands). This theory also sounds likely when considering that DSA occurs due to pinning of

dislocations by solute atoms (C, N, etc.) or vacancies. Depending on whether the domain where the diffusion of these species are occurring is large or small, the rate of their diffusion (and thus the rate of DSA) can change.

Fracture Surface of Annealed and Twinned Steel at Elevated Temperatures

Figure 41 shows the fracture surfaces of AA and TW samples after tension tests at 500 °C. It appears that the fracture surface of the AA samples has a general cup and cone shape, which can be expected since it is more ductile and can undergo significant necking. The neck region is also clearly visible in Figure41-a. The mechanism of the fracture appears to be a ductile fracture with void formation and coalescence, which is again expected from stainless steel at 500 °C. The voids, in different grains, have different orientations. As for the TW fracture surface shown in Figure 41-b, significantly smaller necking is observed, and the fracture surface appears to be on a flat plane perpendicular to the loading direction. On a closer look, however, this surface also shows dimples signifying ductile void formation and coalescence. Given the fact that a TW samples is noticeably deformed, has many microstructure features such as nano-twins and texture and higher dislocation density compared to AA, in addition to the fact that it fails under a higher stress on a sample with a thinner cross-section, it is interesting to see that the TW samples also fails in a ductile manner. This can also be considered as another sign of the optimum combination of strength and ductility imparted by the structure created through thermo-mechanical process. It must be noted that in a similar study [133], the twin bands formed with noticeable dislocation density inside them were found to behave as hard

particles which were pulled out from the surface during fracture. The twin bands in our work, nowhere in the temperature range tested, demonstrated a similar behavior.

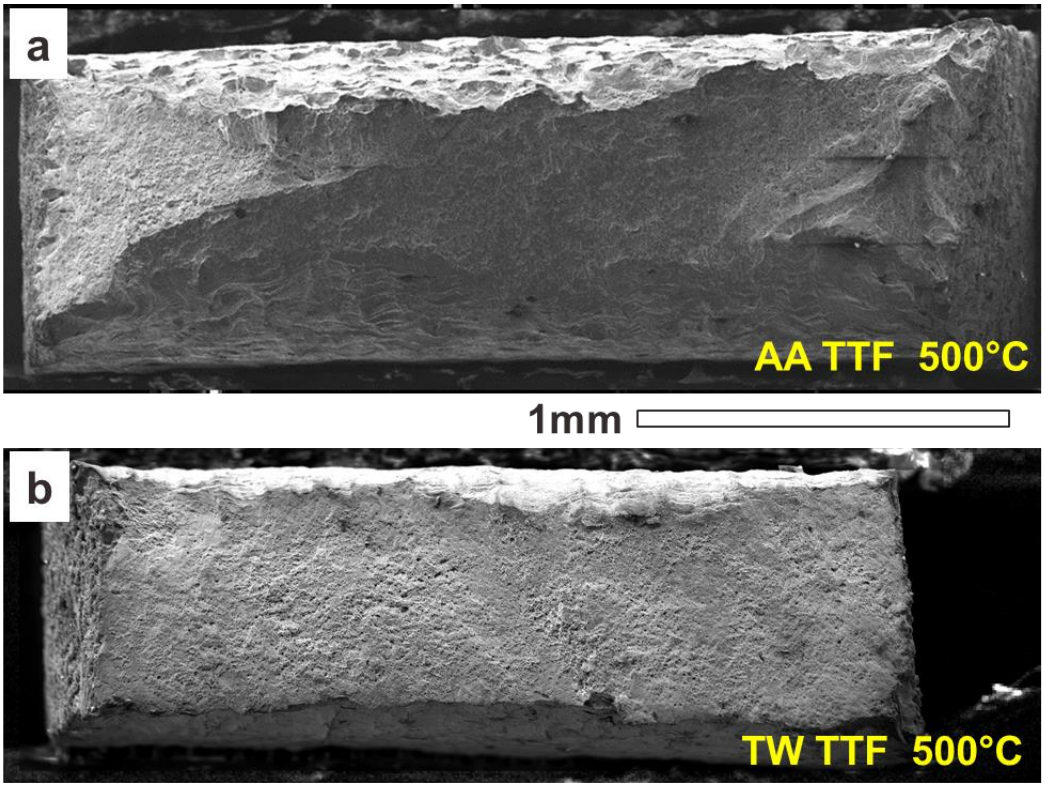

Figure 41 Fracture surface of a) AA, and b) TW samples after tensions test at 500 °C, both surface show dimples, while AA also has a cup-cone fracture.

Hardening Rate of Annealed and Twinned Steel at Elevated Temperatures

Figure 42 shows the hardening rate (i.e. $\theta=d\sigma/d\varepsilon$) of the AA and TW at 20 °C, 100 °C, and 200 °C. For AA, a small plateau can be seen right after yielding, which can be attributed to primary twinning as proposed by El-Danaf et al. [96], and this plateau grow smaller as the temperature is increased to 100 °C and then to 200 °C, suggesting that the extent of twinning decreases as temperature increases. In figure 43, a TEM micrograph of

an AA samples deformed at 100 °C is presented to show that twinning does occur at this temperature. As for the TW, it can be seen that this plateau is more pronounced, as it happens at a higher stress (since yield strength of TW is higher than that of AA), while the hardening values are not noticeably higher for TW compared to AA. This plateau is believed to expected behavior for primary twinning. Especially for the TW case, the change in graphs as the temperature increases is similar to the behavior that De Cooman et al. [149] presented based on the model developed by Kim et al. [150], where a higher twinning kinetics (which leads to a higher volume fraction of twins) cause a larger fall-and-rise in the hardening curve. This model is based on a dynamic Hall-Petch behavior, which is a direct function of mean free path of dislocations or the effective grain size suggested by Equation 2. It must be noted that in an attempt to discover the change in structure, a TW samples was tested at 100 °C up to a strain of ~3%, just beyond the fall-and-rise response seen in the Figure 42, but no noticeable change in the structure was not witnessed. It is possibly because a very small fraction of twins formed during this 3% strain. Keep in mind that as it was shown in Figure 21, no observable twins were witnessed at 10% deformation for AA at room temperature, so it can be expected that a 3% strain doesn't create significant twins, albeit at a much higher stress level. In addition, the fall-and-rise depicted by Kim [149, 150] starts at 5% and finished at around 10% while in the case presented here, it started at around 1% and finished around 3% strain. Another explanation for this fall-and-rise could be based on the fact that the dislocation density has decreased after the last heat treatment in the thermo-mechanical process leading to TW, and during initial stages of loading right after yielding on the TW samples, the material

experiences a larger mean free path in some orientations, depending on the location of a dislocation with respect to grain boundaries and twin boundaries. Such dislocation will be easily mobile, especially under a stress ~400 MPa higher for TW compared to AA. This easy glide can potentially cause a large drop in hardening on the onset of glide. Then as these dislocations meet boundaries and other barriers, the hardening rate increases. In case of either of these reasons responsible for this behavior, the underlying cause is the unique hierarchical structure present in the TW samples.

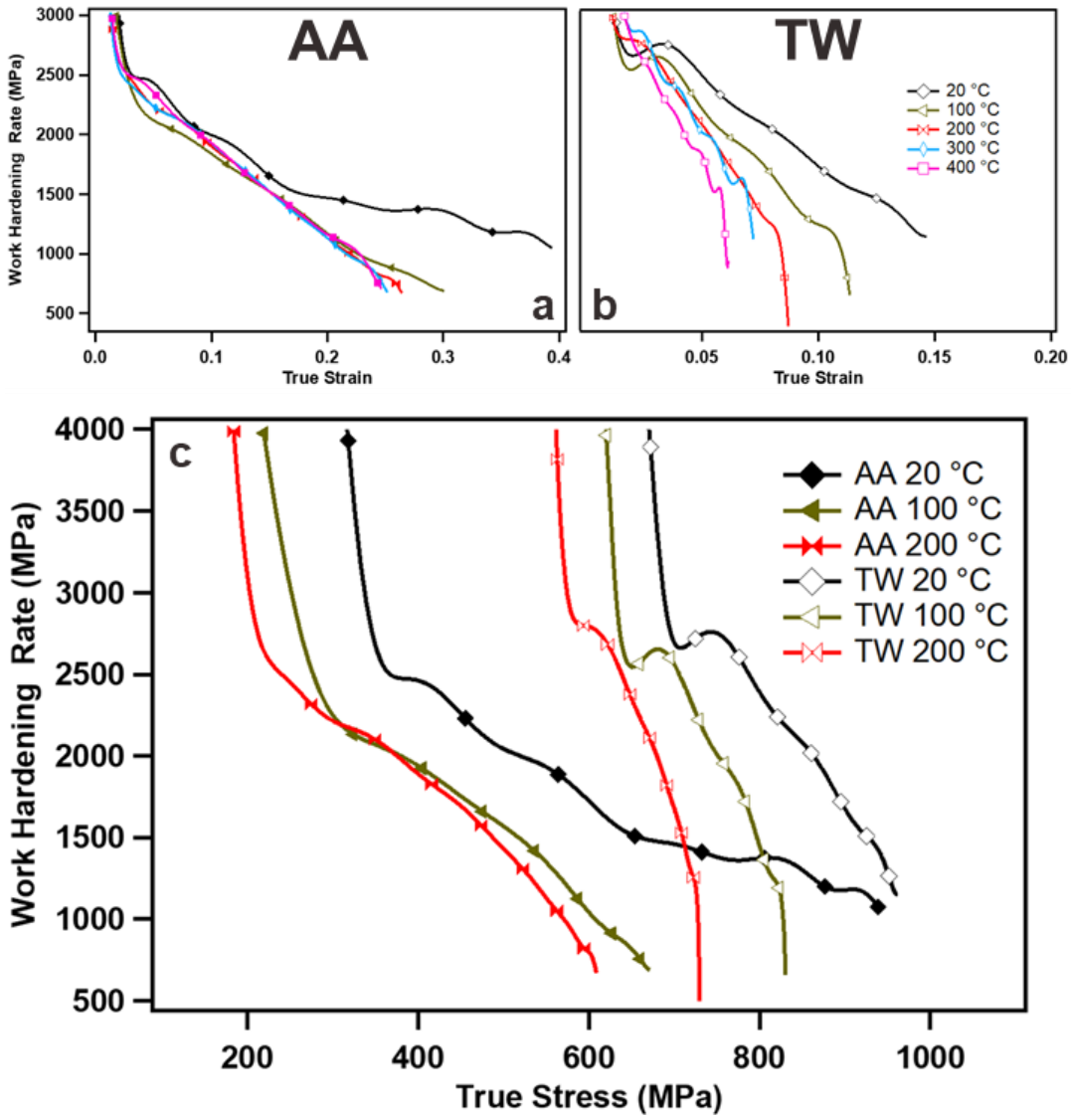

Figure 42 Hardening rate (θ=dσ/dε) for a) AA vs. true strain, b) TW vs. true strain, and c)AA and TW vs. true stress, a sharp fall-and-rise feature in TW samples at temperatures up to 200 °C as a result of the hierarchical structure is present.

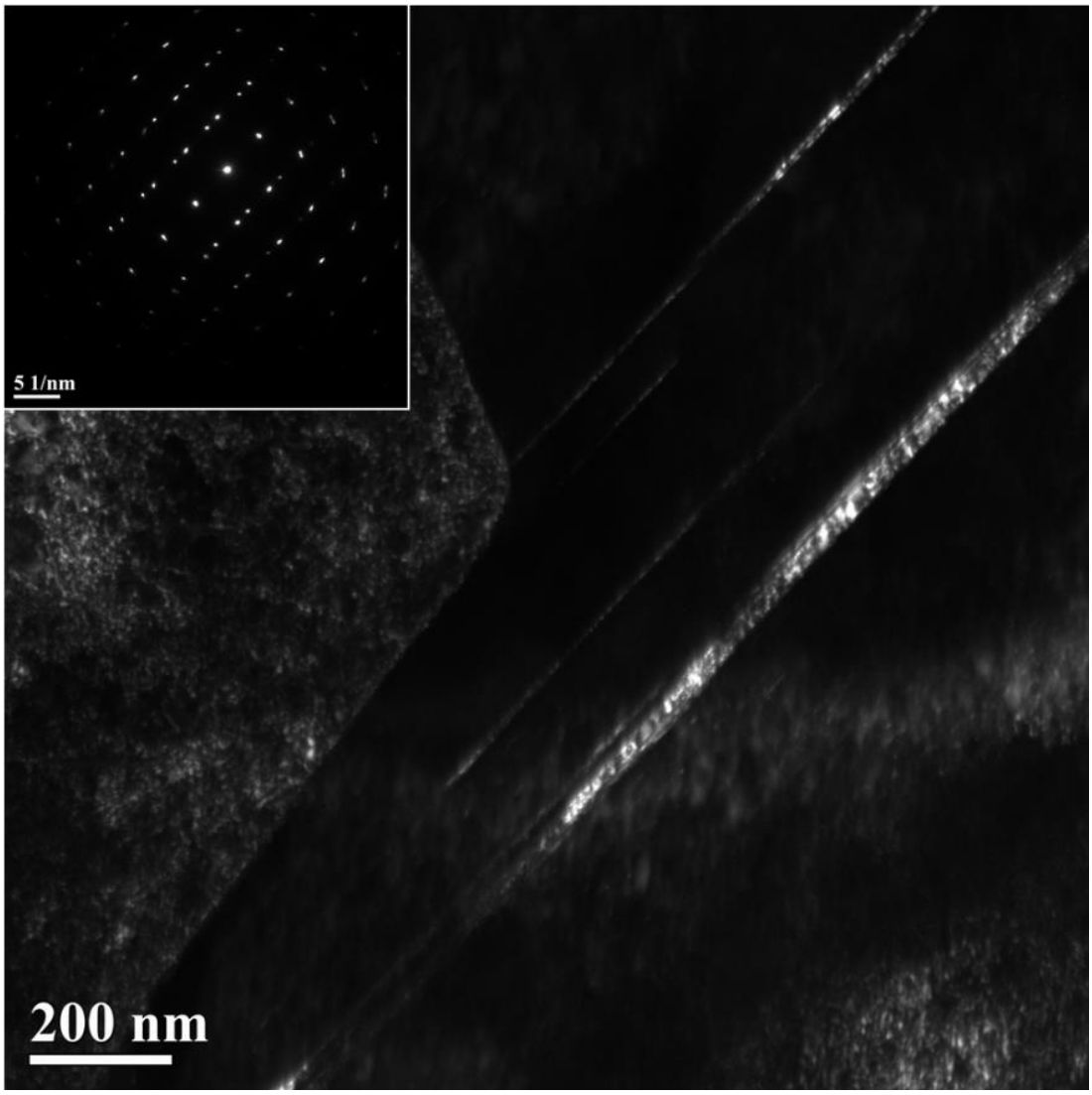

Figure 43 TEM image of AA deformed to failure at 100°C, showing the SADF as the inset of the image corresponding to twinning and the DF image of the twins.

Summary and Conclusion of Role of Thermally-stable Twins on Mechanical Response at Extreme Temperatures

Based on previous results, a thermos-mechanical process was devised that creates a highly-twinned structure alongside a rather low dislocation density. This structure (TW), was tested at extreme temperatures range: -100 °C to 500 °C and compared with fully

annealed structure (AA). At -100 °C, both structures showed martensitic transformation. For AA, a more noticeable TRIP effect was witnessed, compared to TW, possibly due the hierarchical, twinned structure. AA also showed twinning. While the yield strength of TW was higher than that of TW, the UTS values were quite close which in potentially because AA was capable of more TRIP effect. The elongation of both AA and TW were also similar; AA showed slightly larger ductility than TW. The surface fractures of both structures showed signs of ductile fracture, although TW was slightly more irregular. At room temperature and above, TW showed noticeably higher yield strength than AA. This was contributed to the unique structure produced by the thermo-mechanical process. This increase in yield strength appeared to be resistant against increase in temperature, which was contributed to mostly to presence of thermally-stable twins. The UTS values of TW was also larger than those of AA at every temperature. The uniform plastic strain was lower for TW compared to AA, although a total loss of ductility was not observed. The fracture surfaces of AA and TW showed that while AA undergoes a larger extent of necking, the fracture behavior of both structures created almost similar fracture surfaces. Additionally, the serration on the stress/strain graph at 500 °C was observed: for AA, they were typical type A and B, while for TW, they were more random, which can be due to bi-modal length scale of the hierarchical structure in TW.

The high volume fraction of thermally-stable twins were found to beneficial at increasing the high temperature strength of steel, especially without a total loss of ductility. This method can be simply to any structural alloy as long as they form deformation twinning which is thermally stable. This method will also have potential

benefits in improving the creep resistance of materials, since twins have lower energy compared to regular grain boundaries. In addition, this method can be combined with precipitation strengthening. Twin bands can act as nucleation spots for precipitates [93] since they have a slightly higher energy level, as suggested by the recrystallization balloon in Figure 24. This becomes more of interest when take into account that some precipitates, especially intermetallics such as Laves phases that are precipitated in an alloy may over grow and coarsen at high temperatures during long exposures which will lead to a loss in mechanical strength [151]. However, if the precipitation was helped and controlled by the presence of a high fraction of nano twin bands and boundaries, a structure of twin boundaries pinned by precipitates is created which can be expected to be more thermally stable. In addition to high temperature applications, this method may even utilized in applications such as controlled precipitation for prevention of hydrogen embrittlement.

CHAPTER IV

OXIDATION RESISTANCE

In this part, the ability of different alloys to form alumina scale will be studied. For an alloy to meet the criteria, it needs to be fully austenitic, with controllable precipitates, and preferably have low or intermediate value for SFE in order to be able to also show deformation twins, in addition to potentially exhibiting alumina formation.

Table 3 Nominal composition of first generation alloys

wt%	Fe	Ni	Cr	Mn	Nb	Si	Al	Ti	Mo	V	C	N	B
Alloy 1	Ba.	20	14	2	0.86	0.15	2.5	0	2.5	0	0.08	0	0.01
Alloy 2	Ba.	12	14	10	1	0.2	2.5	0.3	2.5	0.5	0.08	0.01	0
Alloy 3	Ba.	17	14	10	1	0.2	2.5	0.3	2.5	0.5	0.08	0.01	0
Alloy 4	Ba.	10	16	10	0	0.5	3	0	2.5	0	0.05	0	0

First Generation Alloys Designed Empirically

Table 3 lists the nominal composition of the first generation alloys chosen for this study. Alloy 1 is based on the published literature where the alloy has been demonstrated to show alumina scale formation [3]. This alloy is chosen as the baseline system. Alloy 2 is based on Alloy 1 but with lower Ni content to decrease the SFE and the cost. Mn content was increased in this alloy to stabilize the austenite (to compensate the reduction in Ni content) and reduce SFE, and Ti and V were added in order to promote the formation of carbides. Nitrogen was added to modify strength and SFE. Alloy 3 is basically Alloy 2 but with more Ni content to make certain of austenite structure. Alloy 4 is somewhere between 316 SS (which shows deformation twinning), and Alloy 1 (which shows alumina formation).

Alloy 1, Based on a Previously-Known Alloy

Figure 44 is the Backscatter Electron (BSE) image of the as-received condition (hot forged) of the alloy. A relatively large precipitate phase with bright contrast can be seen in the image. This precipitate was found to be Nb carbide using WDS. In order to dissolve this precipitate so that we achieve a fully solutionized structure where precipitates can be controlled, samples were heat treated at 1200°C for 1 hr followed by water quenching. Figure 44-b shows that the Nb carbides still persists after this heat treatment and were not dissolved. Heat treatment at 1300°C could not dissolve these carbides either (not shown). Figure 44-c is the XRD spectrum of the heat treated alloy and it depicts the presence of a single austenitic phase. However, the fact that we cannot control the Nb carbides in this alloy is a disadvantage, because they exist in the structure in the form of big particles that would negatively impact the mechanical response and would not help for the creep resistance at high temperatures at a desired level that smaller, nano-sized particles would provide. This alloy, thus, will be used as a control sample for alumina-formation studies.

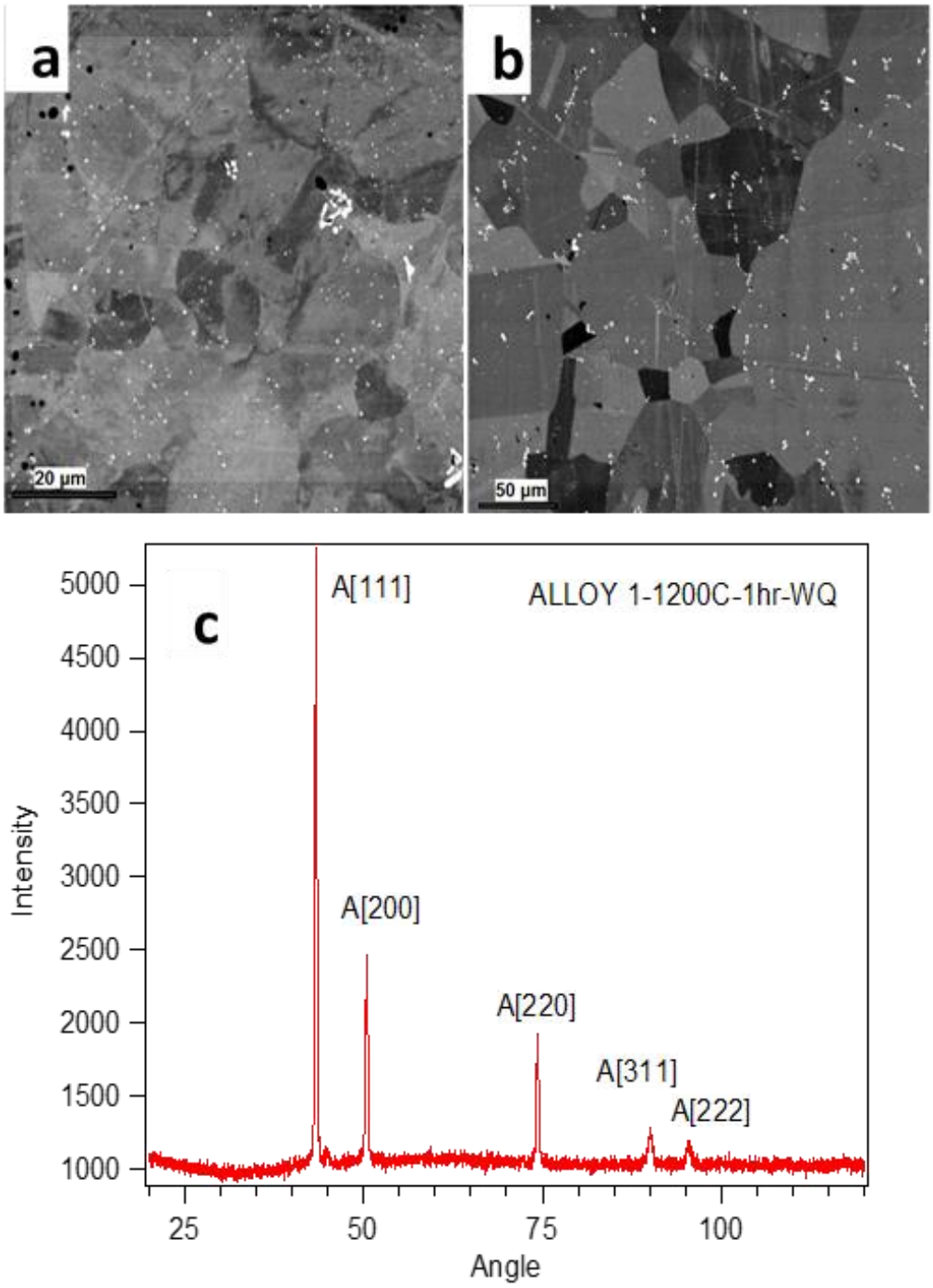

Figure 44 Alloy 1, a) BSE image of the as-received, b) BSE image after heat treatment at 1200°C for 1 hr followed by water quench, c) XRD of the heat treated sample. A fully austenitic structure was detected, but precipitates (NbC) weren't fully dissolved after heat treatment.

Alloy 2 With Lower Nickel Content

This alloy is based on Alloy 1 but with empirically lower Ni content in order to decrease the SFE, and higher Mn to stabilize the austenite and lower the SFE further, as well as nitrogen to enhance strength. The theoretically calculated phase diagram, using ThermoCalc, is presented in Figure 45, and it can be seen that a fully austenitic structure cannot be achieved, although it must be noted that these calculation may be inaccurate on occasions. Figure 46-a shows the OM image of the as-received condition. A dual phase can be clearly seen. In spite of this, in an attempt to homogenize the structure, samples were cold rolled to an 80% reduction in thickness (Figure 46-b). Figure 46-c is the XRD spectrum of this structure and presence of ferrite can be seen. Then the cold rolled sample was heat treated at 1200°C for 1 hr followed by water quenching, and the OM image is presented in Figure 47-a. The dual structure still persists in the structure and the XRD results (Figure 47-b) show that both austenite and ferrite exists in the structure. So it can be deducted that this alloy is not capable of showing a fully austenitic structure, which is a requirement for the alloy design. The significance of this finding lies where it pints out the low effectiveness of a purely empirical approach to alloy design. Moreover, the presence of Nb,Ti-rich carbides were confirmed in the sample using WDS, as well as the Nb-rich Laves phase, emphasizing the default in dissolving and controlling these precipitates. Therefore, based on the fact that this alloy does not meet all the criteria (not fully austenitic and uncontrollable precipitates exist), it is not considered as a good candidate and will not be studied further.

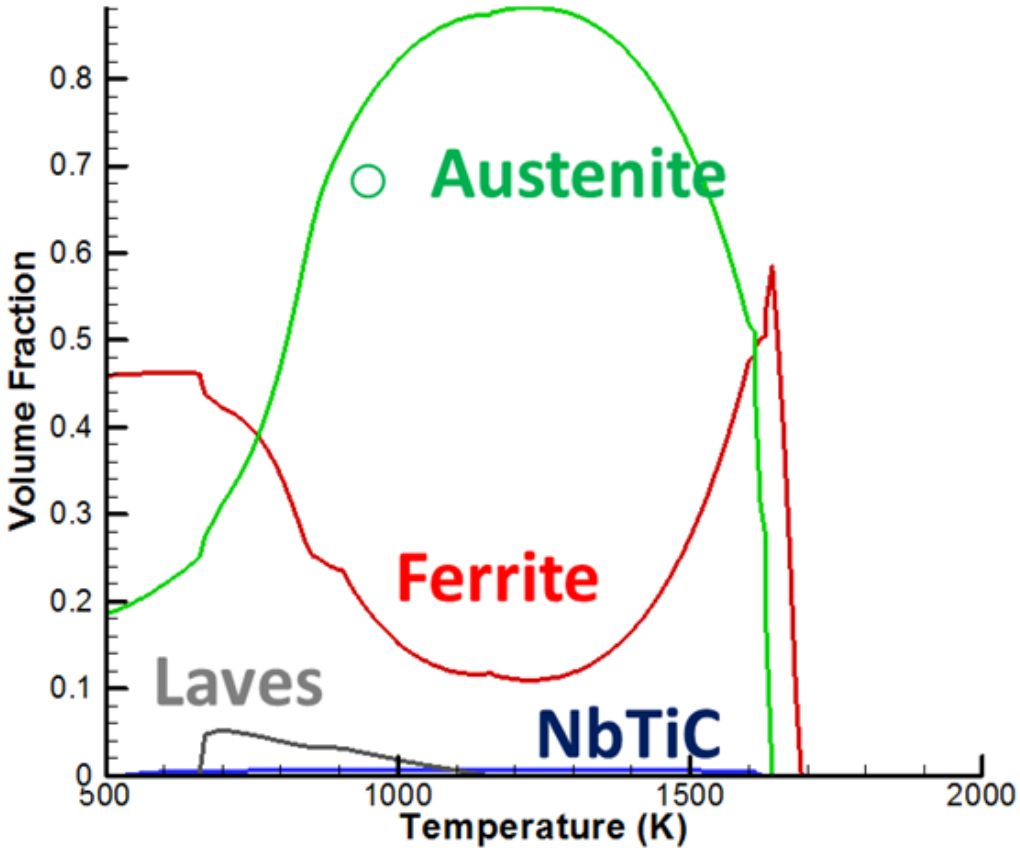

Figure 45 Phase prediction of Alloy 2 using thermodynamic calculations, a fully austenitic matrix is not expected.

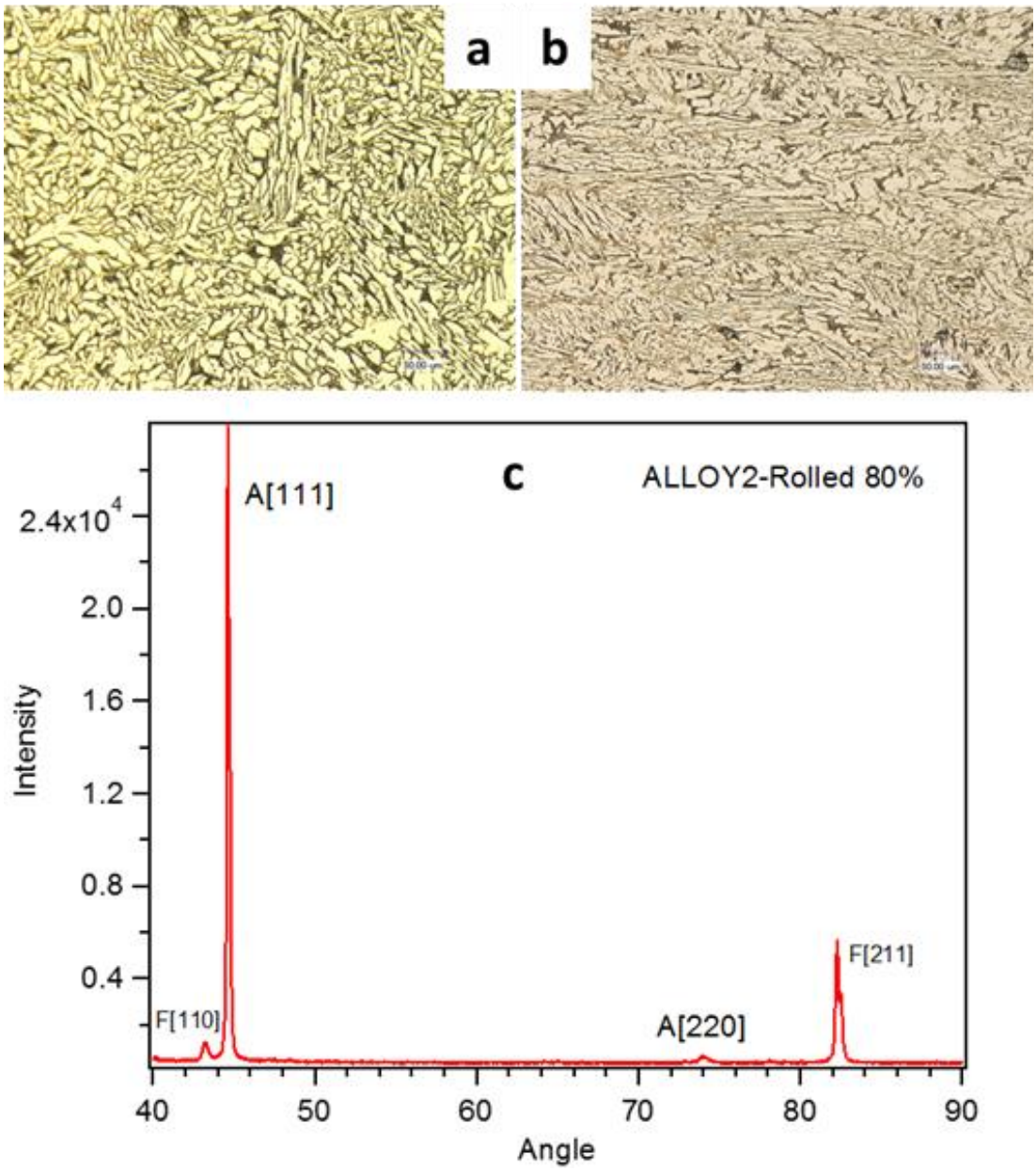

Figure 46 Alloy 2, a) OM image of as-received sample, b) OM image of the sample cold rolled to 80% thickness reduction, and c) XRD of the cold rolled sample. Two continuous phases were detected to be austenite and ferrite.

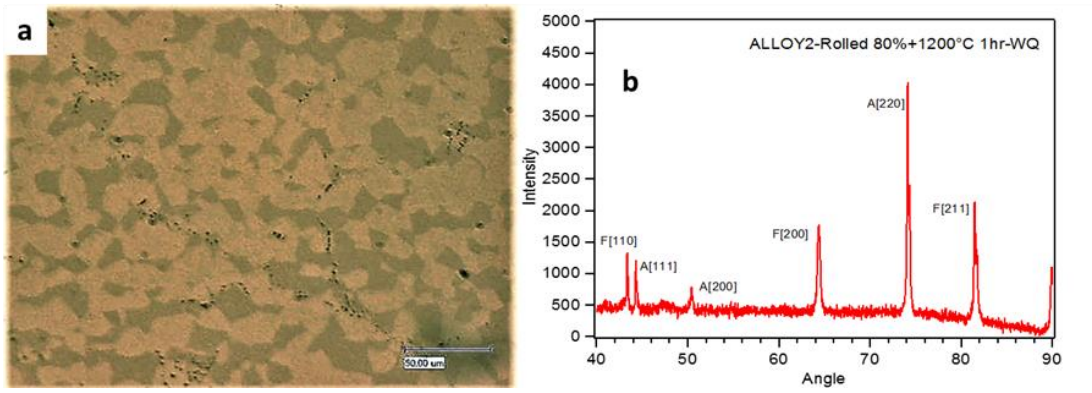

Figure 47 Alloy 2, heat treated at 1200°C for 1 hr then water quenched, a) OM image, b) XRD. Ferrite phase still exists after the heat treatment.

Alloy 3 With Higher Nickel Content

Alloy 2 wasn't fully austenitic, thus we added more Ni and created Alloy 3. Alloy 3 is similar to Alloy 2, only with 17 wt% Ni contents instead of 12 wt% as in the case of Alloy 2. Figure 48-a shows that the as-received condition is heavily dendritic. Therefore, samples were cold rolled to a reduction of 80% in thickness and then heat treated at 1200°C for 1 hr followed by water quenching. The OM image of this structure (Figure 48-b) shows a single phase structure with noticeable amounts of precipitates. WDS (not shown) confirmed that two types of precipitates exist: rod-like aluminum nitrides, and round Nb,Ti-rich carbonitrides. The XRD (Figure 48-c) shows that the structure is fully austenitic. As a result, it can be deduced that due to absence of ferrite, more aluminum is available in the matrix and forms nitride with nitrogen. This phenomenon is not completely favorable because Al needs to be present in the matrix in order to form Alumina on the surface. In addition, this notable amount of precipitates in a water quenched sample show the difficulty to control the successive precipitation. Ideally, one

would prefer precipitate free solution heat treated microstructures such that the subsequent precipitate size and volume fraction could be controlled with proper heat treatments. Furthermore, cold rolled samples were heat treated at 1300° to get rid of the precipitates, but the OM image of the obtained structure (Figure 49-a) shows that the precipitates still remain in the structure, mostly around grain boundaries. Even heat treating at 1150° for 24 hrs then water quenching (Figure 49-b) could not dissolve the precipitates. Despite the presence of sizeable precipitates, this alloy will be studied further for oxidation behavior, based on its fully austenitic structure.

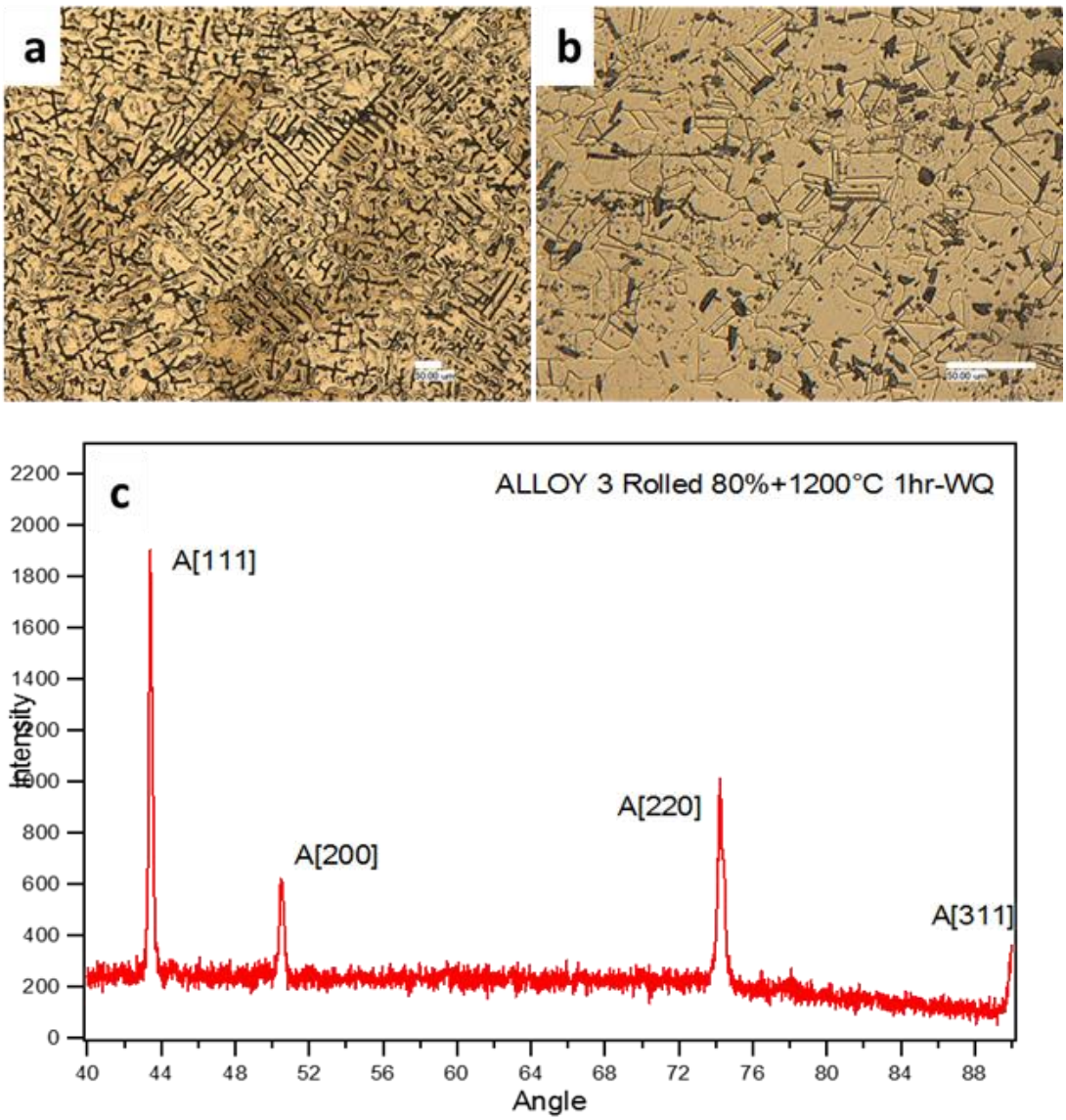

Figure 48 a) Alloy 3, OM image of as-received condition, b) OM image of cold rolled 80% sample, then heat treated at 1200°C for 1 hr followed by water quenching, c) XRD of sample shown in b. Cold rolling + heat treatment created an austenitic matrix, with significant fraction of precipitates: aluminum nitrides and Nb,Ti-rich particles.

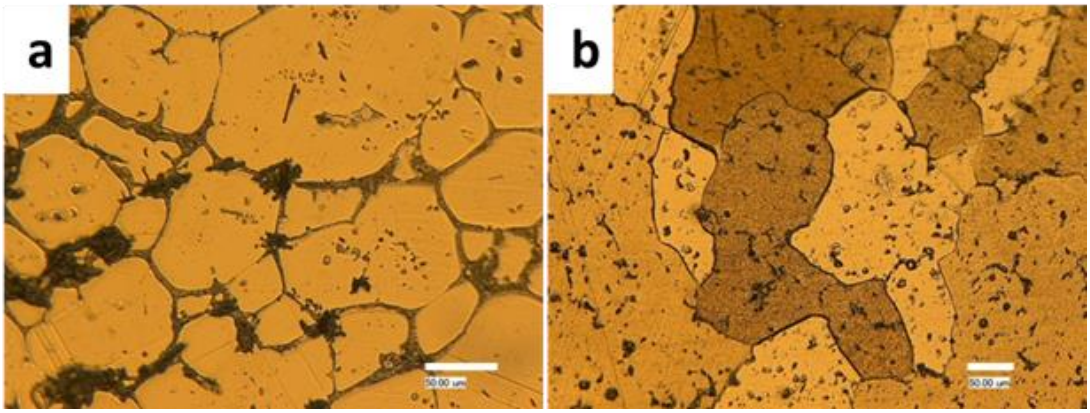

Figure 49 Alloy 3, a) OM image of cold rolled 80% sample, then heat treated at 1300°C for 1 hr followed by water quenching, b) OM image of sample heat treated at 1150° for 23.5 hrs followed by 1200°C for 0.5 hr then water quenching. Volume fraction and size of precipitates have decreased.

Alloy 4 Designed Between Alloy 1 and 316 Stainless Steel

Alloy 4 has a composition between Alloy 1 (which forms alumina scale) and 316 stainless steel (which forms mechanical twins). This alloy has half the Ni content of Alloy 1, similar to 316 SS, and to keep SFE low. We added more Cr than Alloy 1 to get closer to the composition of 316 SS, but still less than that of 316 SS. Mn content was much higher than that for both Alloy 1 and 316 SS, to stabilize austenite. Si content was increased from the value of Alloy 1, but still smaller than 316 SS. Mo content is the same for all 3 alloys. Nb and B was removed from the composition to be similar to 316 SS, in addition to eliminate the possibility of forming dissoluble precipitates. Figure 50-a shows a BSE image of the as-received (as-cast) condition, and it can be seen that it has a dual phase structure. Heat treating at 1200° for 50 hrs followed by water quenching does not homogenize the sample (Figure 50-b). Samples were severely plastically deformed using ECAE at 900°C (Figure 50-c) and then heat treated at 970°C for 0.5 hr followed by water

quenching. This temperature was selected because based on thermodynamic phase diagrams, austenite has the highest fraction at that temperature (~75%). The structure shows a dual phase of ferrite and austenite (Figure 50-d). The reason is lack of enough Ni to stabilize austenite over ferrite and the additional Mn is not sufficient to stabilize austenite. Therefore, this alloy is not a good candidate for this study.

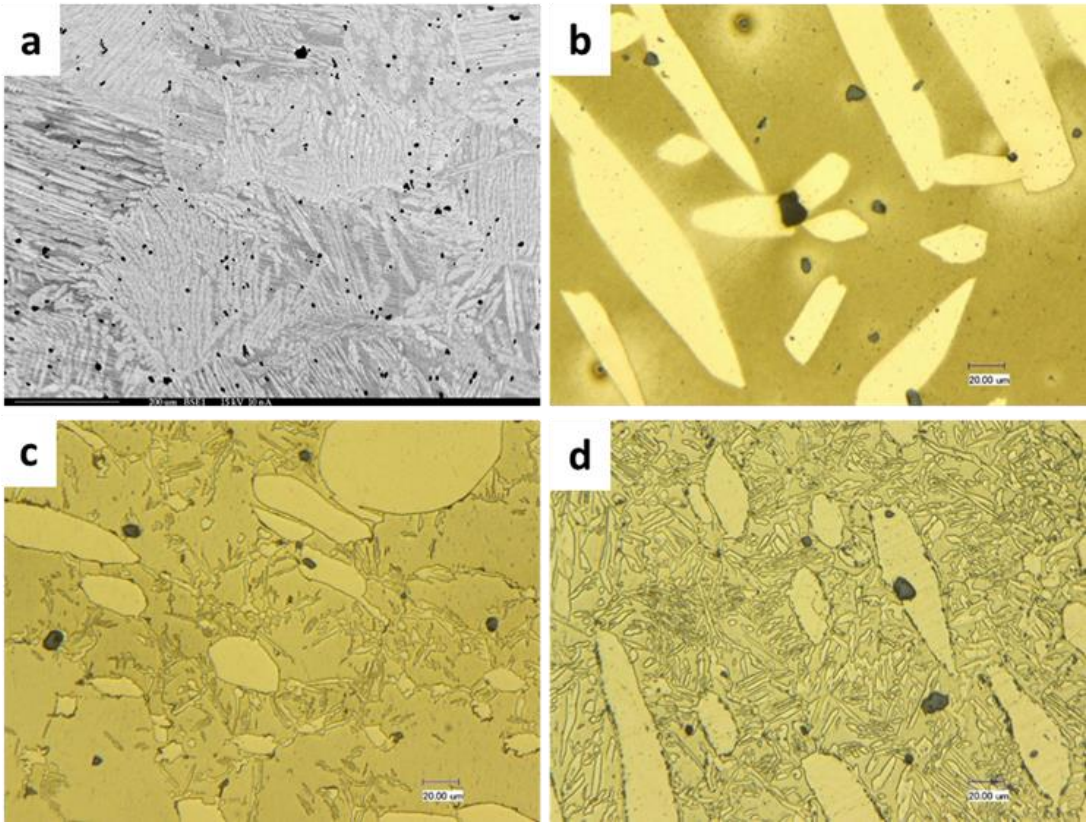

Figure 50 Alloy 4, a)BSE of as-received samples, b)samples heat treated at 1200°C for 50 hr followed by water quench, c) after ECAE at 950°C, then d) samples heat treated at 970°C for 0.5 hr followed by water quenching. Dual structure exists after extrusion + heat treatment.

Second Generation Alloys Designed Based on an Oxidation Model

We have shown that the first generation alloys with the selected composition We have shown that the first generation alloys with the selected composition listed in Table 3 shows no success in satisfying the all alloy design criteria, i.e. stable austenite structure, and controllable precipitates. As a result, new alloys were designed using the thermodynamic models and free energy calculations that's supposed to be able to from alumina scale, while being fully austenitic. The nominal composition of this designed alloy is presented in Table 4, and it can be compared with the nominal Alloy 1 composition that should exhibit alumina formation. This alloy was fabricated 3 times to check the repeatability of reaching the target composition, and is shown in Table 5. In this table also we can see the measured composition of Alloy 1.

Table 4 Nominal composition of Alloy 1 as the baseline material and the designed alloy.

wt%	Fe	Ni	Cr	Mn	Nb	Si	Al	Mo	C	B
Alloy 1	Ba.	20	14	2	0.86	0.15	2.5	2.5	0.08	0.01
PGAA2	Ba.	17.15	15.3	9	-	0.19	3.11	2.24	0.088	-

Table 5 Actual composition of Alloy 1 and the designed alloy fabricated three different times (three batches). Measurements were done using Wavelength Dispersive Spectroscopy and Galileo OHN.

Alloy	Fe	Ni	Cr	Mn	Nb	Si	Al	Mo	C	B	N	S	Comment
Alloy 1	58.78 ± 0.66	19.26 ± 0.46	14.26 ± 0.15	2.06 ± 0.07	0.4 ± 0.12	0.16 ± 0.01	2.64 ± 0.09	2.39 ± 0.13	?	?	?	0.04 ± 0.01	WDS+OHN on AR
PGAA2-1	50.92 ± 0.14	17.40 ± 0.07	16.98 ± 0.03	8.93 ± 0.09	-	0.42 ± 0.01	2.81 ± 0.06	2.50 ± 0.05	?	-	292 ppm	0.04 ± 0.01	WDS+OHN on HT
PGAA2-2	50.75 ± 0.10	15.17 ± 0.05	17.37 ± 0.12	8.96 ± 0.06	-	0.24 ± 0.01	4.53 ± 0.05	2.94 ± 0.06	?	-	18.73 ppm	0.05 ± 0.01	WDS+OHN on HT (Dark Phase)
	51.47 ± 0.10	17.90 ± 0.10	15.04 ± 0.08	9.40 ± 0.02	-	0.22 ± 0.02	3.91 ± 0.08	2.04 ± 0.05	?	-		0.03 ± 0.01	WDS+OHN on HT (Light Phase)
PGAA2-3	52.18 ± 0.16	17.13 ± 0.12	15.56 ± 0.05	9.38 ± 0.06	-	0.22 ± 0.01	3.25 ± 0.12	2.26 ± 0.05	?	-	45.09 ppm	0.03 ± 0.01	WDS+OHN on HT

The as-received condition of first model alloy, PGAA2-1, shows the presence of a dendritic second phase. In an attempt to homogenize the structure, samples were cold rolled to 80% reduction in thickness, then heat treated at 1080°C for 23 hr then 1150°C for 1 hr followed by water quenching. The image (Figure 51) shows a high contrast BSE image of this structure, and a single phase structure can be witnessed. Some precipitates still exist in the structure. These precipitates were studied in more detail using EDS. Two major types of precipitates were detected: first is aluminum rich precipitates with sharp corners which WDS determined them to be nitrides, and the second circular precipitates are rich in Mn and Mo, which are probably the Laves phase. Figure 52 shows sample that was heat treated at 1200°C for 50 hrs followed by water quenching, in an attempt to homogenize the samples further. The OM image shows a single phase structure with rather sizeable precipitates. The EDS analysis of the location shown in the SEM image depicts that there exists rod-like Al-rich precipitates (Aluminum nitrides) which have evolved due to presence of Nitrogen impurity in the alloy. This evolution causes the Al content in the matrix to decrease lower than the intended value. Also Mn, Mo rich round precipitates that have some sulfur impurity in them exist as validated by EDS.

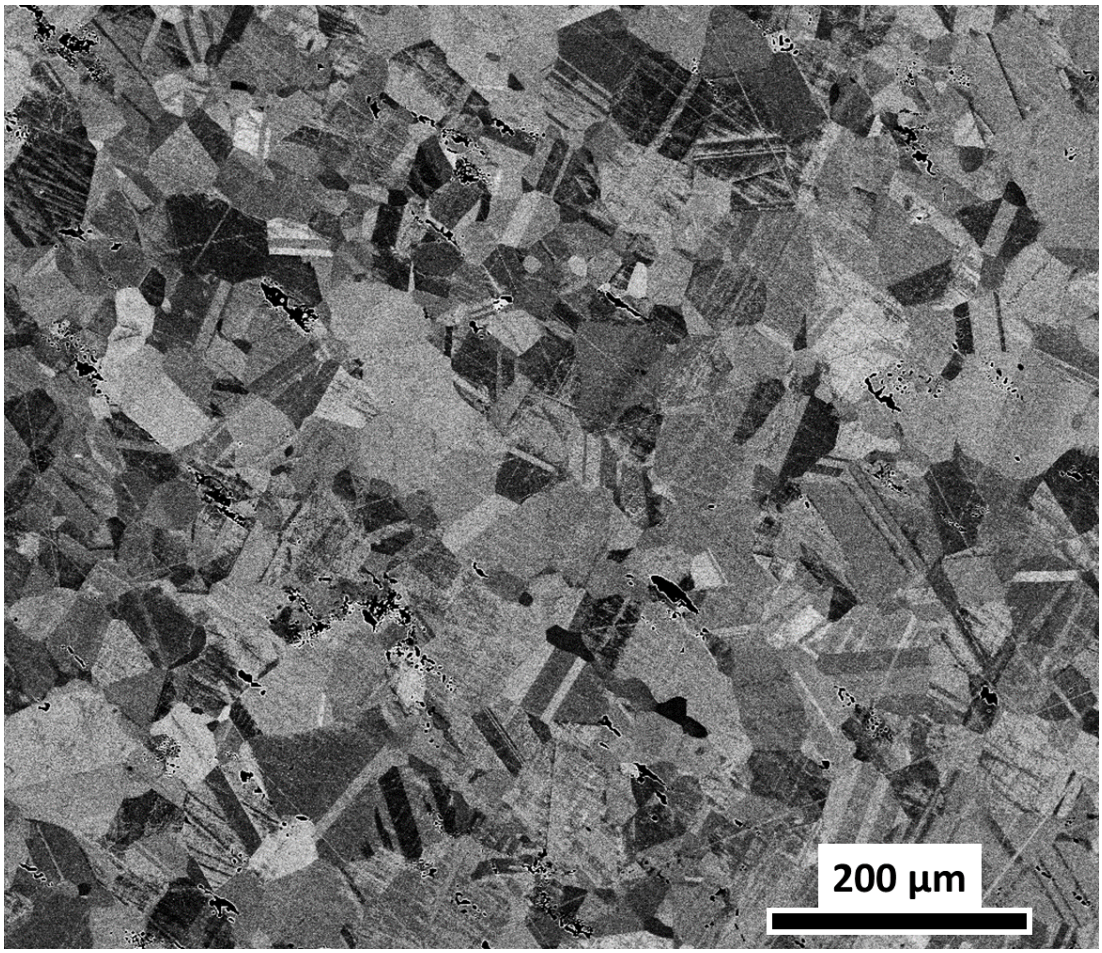

Figure 51 PGAA2-1, High contrast BSE image of sample 80% cold rolled then heat treated at 1080°C for 23 hr then 1150°C for 1 hr followed by water quench, showing a single-phase structure.

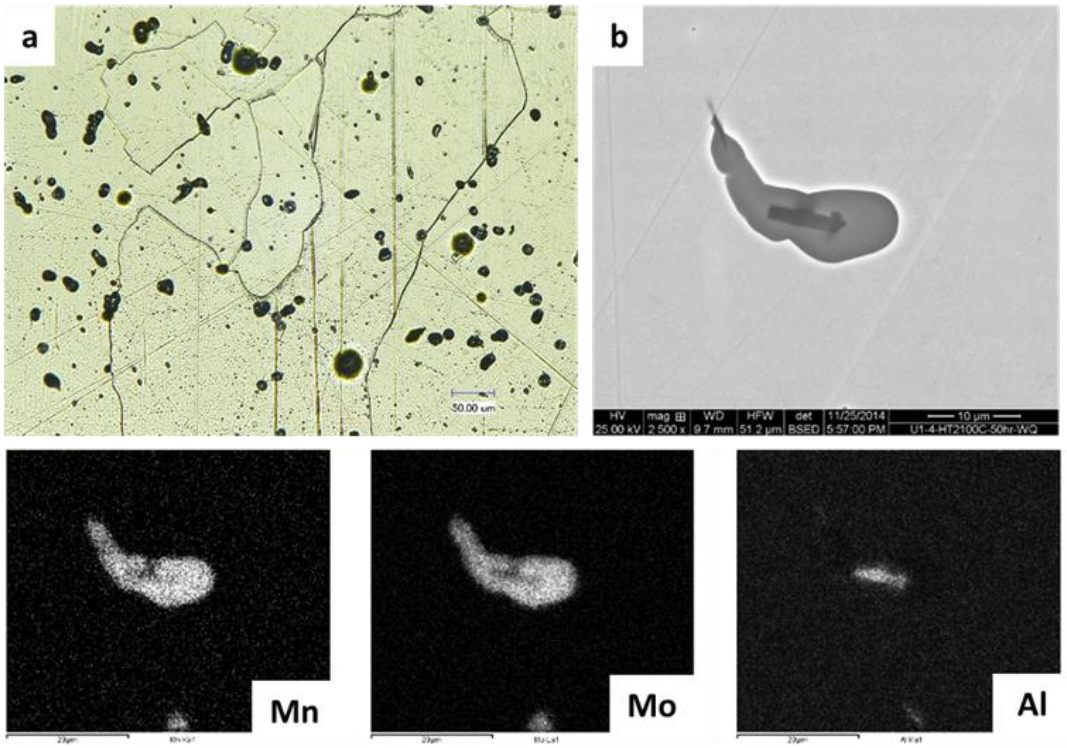

Figure 52 PGAA2-1, heat treated at 1200°C for 50 hrs, followed by water quenching, a) OM image, b) SEM image and elemental maps. In the austenite matrix, rather big precipitates exist that are frequently AlN surrounded by Mn/Mo-rich precipitates.

The as-cast PGAA2-2 alloy structure had a dual phase structure. Heat treating at 1150°C for 72 hrs followed by water quenching still produces a dual phase structure, as depicted in Figure 53. Heat treating at 1200°C for 50 hrs followed by water quenching also has a dual phase structure (a light phase and a dark phase with compositions mentioned in Table 5), and the XRD analysis confirms presence of ferrite and austenite in the structure. The reason for the difference between the two batches of the alloy with the same nominal composition is the higher Al content present in the matrix in the latter batch, which stabilizes the ferrite. That is why two different rows for composition are reported in Table 5 for this alloy batch. It is clear that the melting practice makes a significant

difference in the results and shows the importance of the chemistry control. This dual phase structure is unfavorable for the set alloy design criteria, which makes this alloy unfit for oxidation studies.

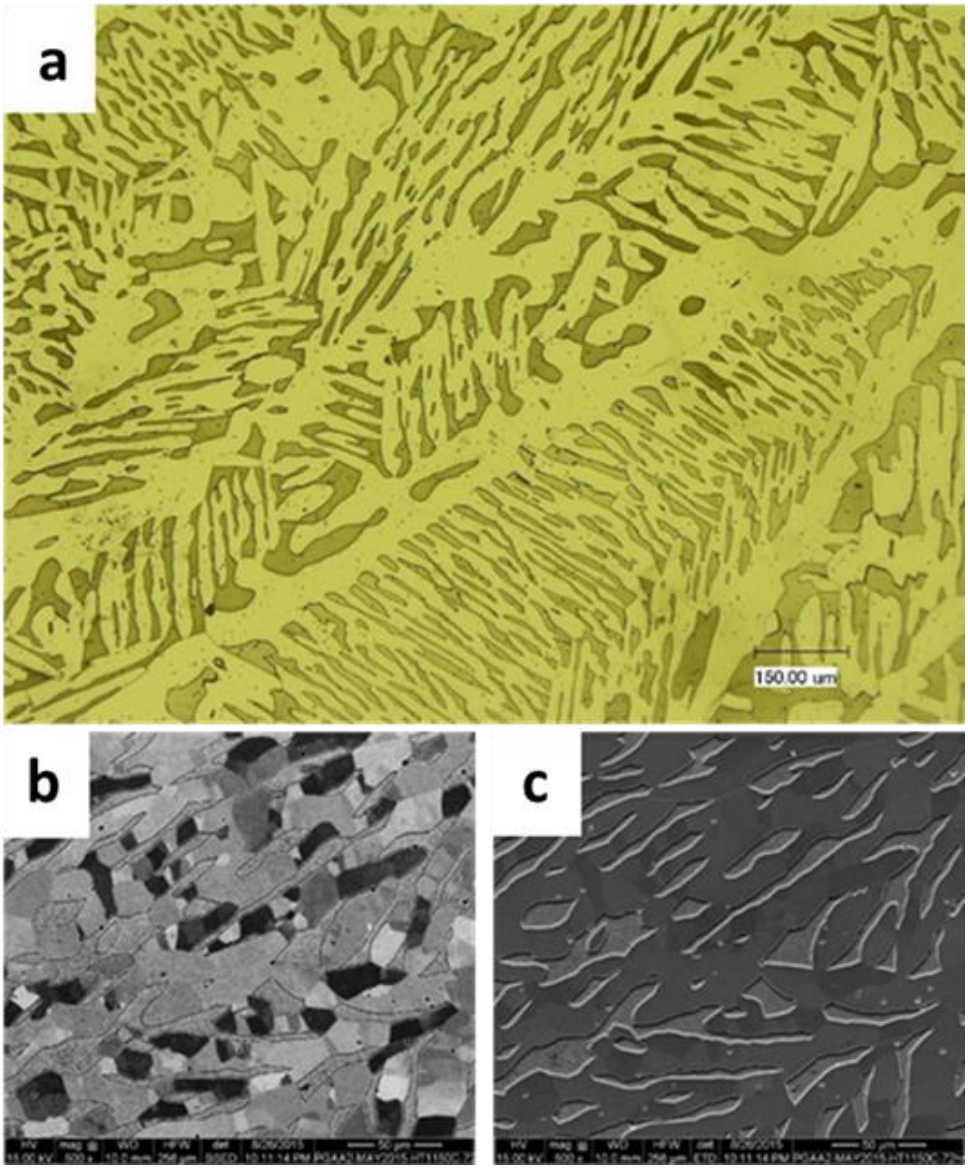

Figure 53 PGAA2-2, a) OM of heat treated at 1150°C for 72 hrs followed by water quenching, and b) BSE and c) SEM image. Dual phase structure exists: a light phase and a dark phase.

PGAA2-3 was fabricated with better compositional precision, and Figure 54 shows the structure of this alloy after heat treatment at 1200°C for 24 hrs followed by water quenching. It can be seen that a single phase exists with the composition close to the model suggestion. This alloy shows promise for the required criteria, and will be used for oxidation investigations.

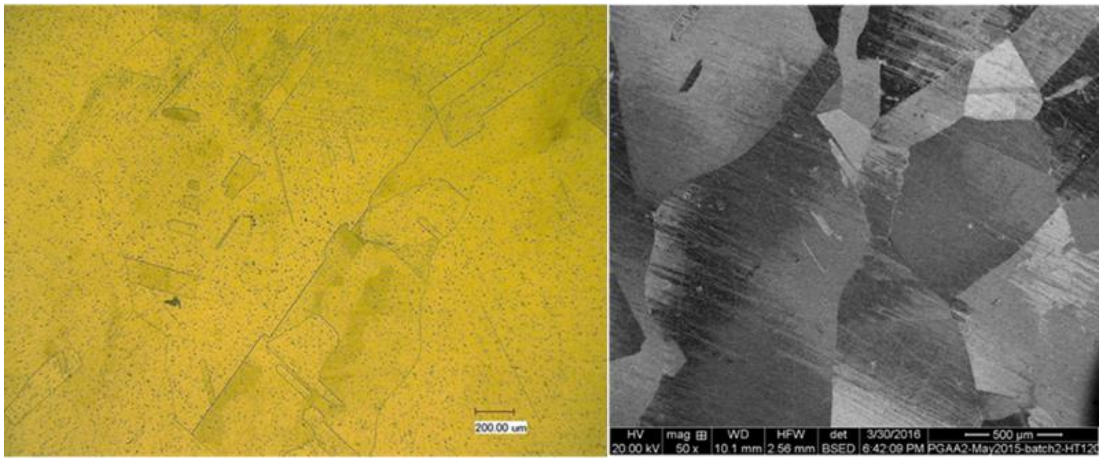

Figure 54 PGAA2-3 heat treated at 1200°C for 24 hrs followed by water quenching, OM and BSE. A fully austenitic and homogenized structure exists.

Short-term Oxidation Test of Model Alloys vs. Control Alloy

The passivation scales of conventional stainless steels (mostly chromium oxide) are usually unstable at high temperatures, especially in presence of water vapor, since they turn into volatile oxy-hydroxides. Aluminum oxide, or alumina, on the other hand, is more stable at such conditions, therefore, alumina-forming steels have been recently introduced and gained significant research interest [66, 152, 153]. The major challenge for this type of alloys is to satisfy the minimum Al requirement to form an alumina scale, while

maintaining an austenitic matrix, as Al is a ferrite stabilizer. The first successful implementation of Alumina-Forming Austenitic Stainless Steels (AFA-SSs) was introduced by Yamamoto *et al.* where a 20Ni-14Cr-2.5Al-1Nb AFA-SS was developed. This alloy forms protective alumina scale after oxidation experiments at 800°C for 72 hours [3]. In this alloy, Ni content was kept high to counter the ferrite-stabilizing effect of Al [70]. Alternatively, manganese addition has been investigated as a substitute for Ni as an austenite-stabilizer due to its lower cost, and high-Mn alloys have been shown to form Mn-rich protective alumina scale after 1000 hr oxidation tests at 700 °C and 800 °C [154]. Since AFA-SSs, designed for high temperature applications, are expected to achieve high creep strength at high temperatures, various beneficial precipitates are necessary, such as B2-type β-(Ni, Fe)Al, $L1_2$-ordered Ni_3Al precipitates, and nano-carbides, which are the result of the presence of constituents like Al, Nb, V, Ti, Zr, Y, Cu, B, C, etc. [73, 74, 154-157]. These alloying elements also indirectly affect the alumina forming capability of these steels. For example, the presence of Ti and V in steels is detrimental to alumina formation [158]. Due to strong exothermic interactions with Al, they increase the required Al content to form alumina scale and this negatively impact the austenite stability. In another study, it was shown that higher Al content improves the oxidation resistance as expected, but not because it increases the Al content in the austenite, but instead, due to the formation of more B2-NiAl precipitates that act as Al reservoirs. A B2-denuded zone was detected [159] right below the scale after the oxidation tests, that supports this conclusion. Interestingly, calculated chemical compositions show that the Al content of the austenite does not increase proportionately to the overall Al content, but the relative

Cr content in austenite increases which has been claimed to be due to the formation of Al and Ni rich precipitates, "effectively enriching the matrix in Cr" [159]. This Cr-enrichment should help with the formation of protective alumina through third-element effect. Third-element effect suggests that in an A–B–C alloy system (if A is the most noble, B has an oxygen affinity between A and C, and C is the most reactive component), the addition of B reduces the critical concentration of C required to form an external scale of C-oxide. In this case, Cr, which has an oxygen affinity between Al and Fe, decreases the required Al content necessary for alumina scale formation [160]. These examples point out the complexity of designing an alloy that eventually satisfies multiple constraints, including alumina formation. The presence of Nb has been reported as necessity for alumina formation in an alloy containing ~20wt.% Ni and 2.5-4 wt.% Al [158]. This is due to the positive role of Nb in promoting B2-NiAl precipitates at higher Nb contents (0.2 to 1 wt.%), which can act as Al reservoir for alumina formation. Similarly, Nb slightly decreases Al solubility in austenite, and increases the relative Cr content in the matrix that helps with alumina formation due to the third-element effect [161]. The effect of the austenite composition, however, is more important in dictating the alumina formation than the potential role of the precipitates as the Al reservoirs [71]. On the other hand, addition of more than 1 wt.% Nb has detrimental effects on creep resistance, due to the stabilization of Fe_2(Mo,Nb) Laves phases and formation of coarse, undissolvable carbides [24]. The alloying elements also influence the structure of the scale that forms during oxidation, which in turn defines the oxidation resistance. A general trend of multi-layer scale formation is observed in AFA-SSs, albeit with different structures depending on the

alloying elements. The cross-section elemental mapping of a 25Ni-15Cr-(3 to 4)Al-2.5Nb alloy showed a dual-layer scale: an outer oxide layer of Al,Cr,Fe,Mn,Nb and an inner layer of Al oxide [159]. The oxidation resistance of a 20Ni-14Cr-3Al-0.6Nb-0.1Ti AFA-SS in supercritical water vapor showed improvement due to formation of a multilayer scale which consists of an outer Fe-rich oxide (hematite) layer over an inner Al,Cr,Fe-rich oxide protective layer, followed by a Ni-rich layer in the bulk of the alloy [162]. Corrosion study on a 25Ni-14Cr-4.3Al-Nb AFA-SS in supercritical water showed that it forms a dual scale: an Fe-rich scale on top of a layer rich in Al-Cr; the latter layer grows at a slower rate which is beneficial for corrosion resistance [163]. The scale formed on a high-Nb alloy consists of an outer layer of Fe,Mn-rich oxide on top of a Cr,Al-rich layer [71]. Addition of Mn leads to the formation of a discontinuous (Mn,Cr,Fe)-rich outer scale on top of a (Al,Cr)-rich oxide, with (Cr,Mn)-rich and Nb-rich nodules and AlN precipitates [164]. This general trend of multi-layer oxide formation appears to follow this order: an outer oxide scale rich in elements that diffuse fast to the surface and/or have a higher rate of oxidation, on top of an Al-rich scale that provides oxidation resistance, commonly followed by a denuded zone.

In summary, addition of different alloying elements to AFA-SSs has been studied for their effects on alumina formation and precipitation, and it was shown that each alloying element imparts various complexities in the structure of the alloy/scale. In the present work, we investigate the oxidation response of a custom AFA-SS alloy we have recently designed [165]. The design framework utilized here is schematically presented in Figure 1. The design process of this alloy starts with a random alloy composition in the

range of Fe-(10-20)Cr-(10-20)Ni-(0-10)Mn-(1-4)Al-(0-2.5)Mo-(0-0.5)Si (in wt.%) without any Nb or Ti. The goal is to keep the Ni content as low as possible while keeping the fully austenitic structure at room temperature. Thermodynamic calculations is then performed to assure a fully austenitic structure, and no sigma phase formation, using ThermoCalc® software through its TQ Interface that uses the databases TCFE7 and MOBFE1 for the prediction of the stable phases as a function of temperature. Martensite start temperature below room temperature was also considered as a criterion for fully austenitic structure, and was calculated using the Ishida model [166, 167]. Additionally, the third element effect considerations for the oxide formation, combined with the calculated driving forces for the formation of alumina scale and oxide transport properties, were employed to generate a design parameter that is an indicator of the alumina scale formation. The values of this parameter was calculated for the known AFA-SSs and for those that do not form alumina reported in the literature. Then, a threshold value was found empirically, based on the known alumina formers versus non-alumina former alloy systems. For any alloy proposed by the model, the value of its custom parameter must be above the threshold value to be considered as alumina-forming alloy. Then, the alloy composition has been optimized using a Genetic Algorithm based on the design procedure to have the smallest number of alloying elements, and lowest amount of alloying content possible in order to create the simplest AFA-SS that would still form alumina while maintaining the austenitic structure and stability. The goal was to design a low-alloyed AFA-SS that theoretically forms alumina scale, and the purpose of the present work is to experimentally verify the capability of the designed alloy to form alumina scale.

The samples out of both alloys were mechanically polished down to 0.25 μm. For the oxidation experiments, the samples were placed in a furnace in regular lab atmosphere, similar to the work in [3] where Alloy 1 has formed alumina scale after oxidation test at 800 °C for 72 hours. After the oxidation test, the samples were carefully removed and mounted in a conductive sample holder, and mechanically polished down to 0.05 μm. Energy Dispersive Spectroscopy (EDS) elemental mapping and linescans, as well as Secondary Electron Microscopy (SEM) was performed on the cross-section of the samples using a Tescan Lyra SEM under a voltage of 20 kV.

Alloy 1 (Control) Oxidized at 800 °C for 72 Hours

Figure 55 shows the SEM image of the cross-section of Alloy 1, after oxidation test at 800°C for 72 h, together with a few of the corresponding elemental maps. It can be seen that an O-rich layer exists on top, which is the oxide scale. In this oxide layer, at the outermost exists a layer rich in Fe and Mn, which is in agreement with the multi-layer scale formation trend witnessed in literature. The Mn diffuses quickly to the surface and form an oxide, in a mixture with Fe-oxides. These oxides are non-protective at high temperatures. Below this layer exists another layer rich in Cr, suggesting a chromia layer, which is also not stable at high temperatures. Below this layer, an Al-rich layer is determined which is the protective alumina layer. The O elemental map shows no noticeable signs of internal oxidation. Further down the substrate, precipitates rich in Al are detected. The line shown in Figure 55-a is where EDS linescan has been performed, the results of which are shown in Figure 59.

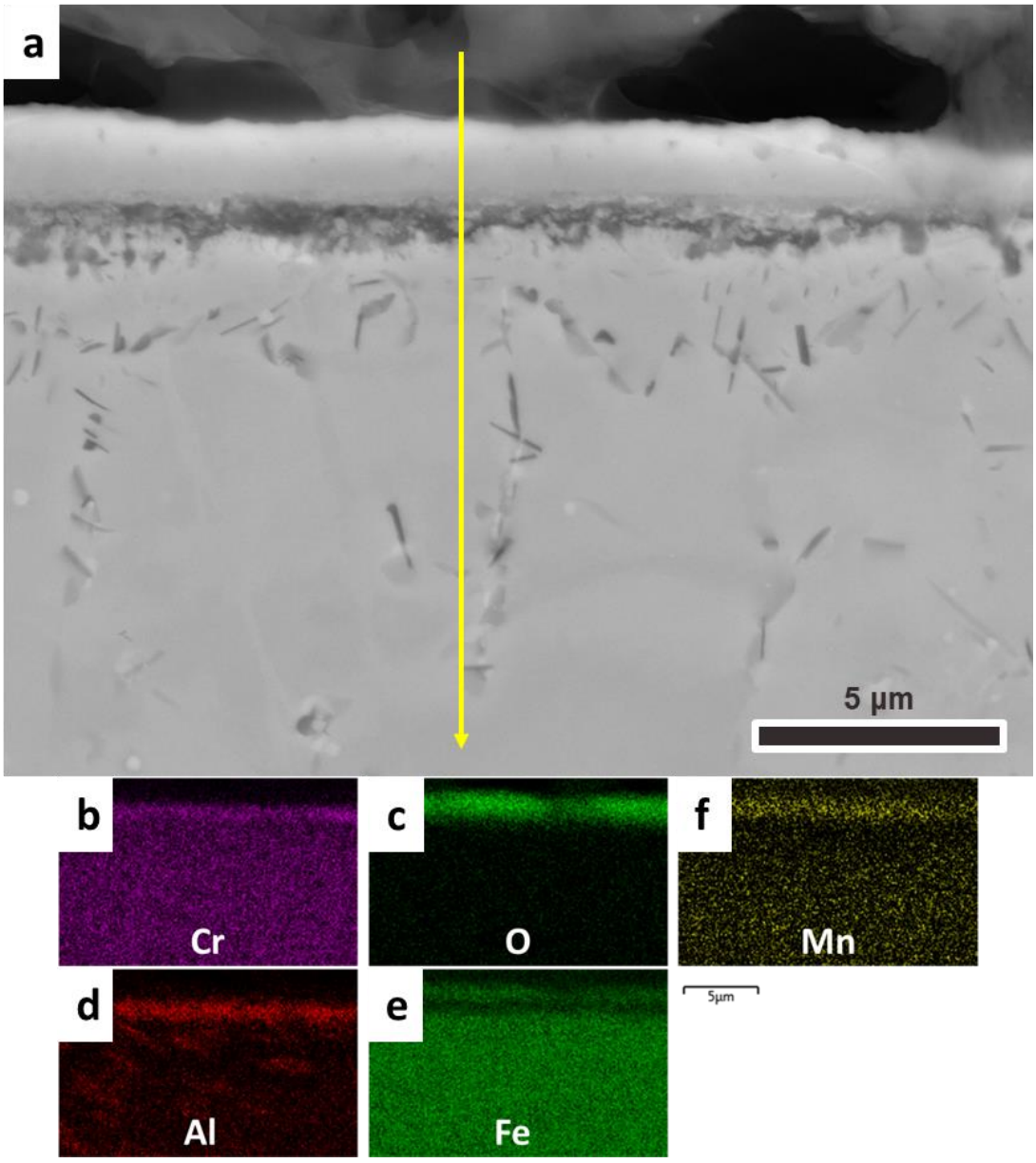

Figure 55 Alloy 1, oxidized at 800°C for 72 h: (a) SEM of the cross-section, and the corresponding elemental maps for (b) Cr, (c) O, (d) Al, (e) Fe, and (f) Mn. A multi-layer scale of Fe oxide on top of Al,Cr layers is formed. The yellow line denotes the linescan, the results of which are shown in Figure 59.

PGAA2-1 Oxidized at 800 °C for 72 Hours

Figure 56 shows the SEM image of the cross-section of PGAA2-1, after oxidation test at 800°C for 72 h, together with a few of the corresponding elemental maps. An oxide scale exists on the surface which is rich in Mn on the outmost layer, followed by a Cr-rich layer. The next layer is an Al layer. An Fe oxide is not apparent in the scale. Al-rich and Cr-rich particles exist a few microns underneath the scale. The layer rich in Al appears to be denuded of Mn and Cr.

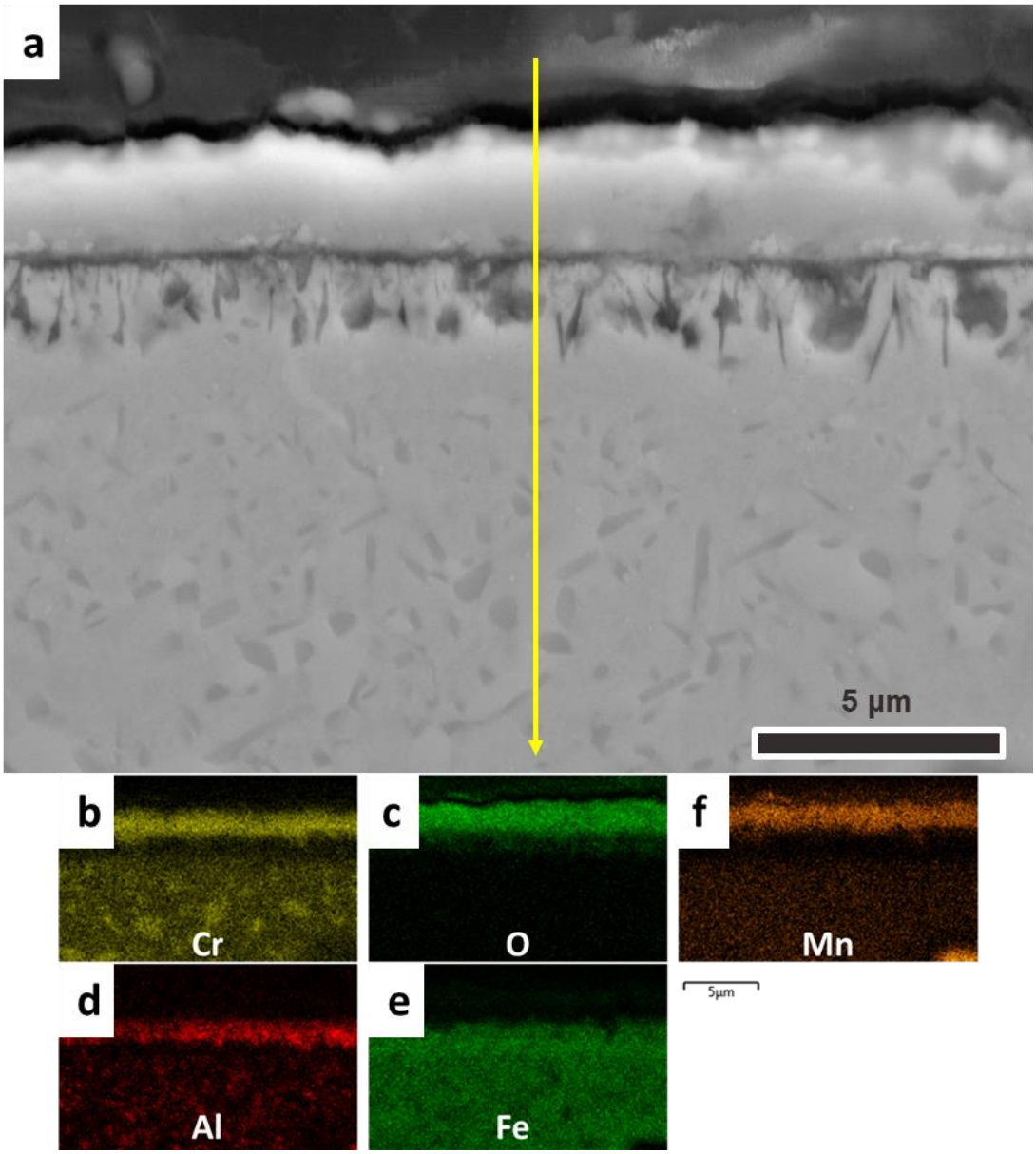

Figure 56 PGAA2-1, oxidized at 800°C for 72 h: (a) SEM of the cross-section, and the corresponding elemental maps for (b) Cr, (c) O, (d) Al, (e) Fe, and (f) Mn. A Cr oxide on top of Al,Cr layers is formed. The yellow line denotes the linescan, the result of which are shown in Figure 59.

PGAA2-2 Oxidized at 800 °C for 72 Hours

Figure 57 is similarly an SEM image of PGAA2-2 after oxidation test at 800°C for 72 h, together with a few of the corresponding elemental maps. The scale is a mixture of Mn,Cr oxide, followed by an Al-rich layer alongside an oxide layer. This layer is also denuded from Mn and Cr. It is interesting that while this alloys was found to be a mixture of ferrite and austenite, as shown in Figure 53, the cross-section shows only a single phase present near the surface. It is possibly because the Al content diffuses towards the surface and leaves the matrix, which is austenite at 800 °C, then when cooled down, since the Al content is lower now, it will not turn into ferrite. It must be reminded here that the model that predicted the oxidation assumed that an austenite matrix is stable over all temperatures.

PGAA2-3 Oxidized at 800 °C for 72 Hours

Figure 58 is similarly an SEM image of PGAA2-2 after oxidation test at 800°C for 72 h, together with a few of the corresponding elemental maps. Again, the scale layer on the surface is Cr/Mn oxide on the outmost followed by Al-rich layer. A much thicker oxide scale is visible in the model alloys. Just below the oxide layer, a thin Al-denuded layer is seen, which is due to outward diffusion and oxidation of Al. Further down the substrate, precipitates rich in Al are present, similar to other alloys, which can act as reservoirs for aluminum in order to maintain the alumina scale. The thick alumina scale is preserved and maintained through the outward Al diffusion from the bulk.

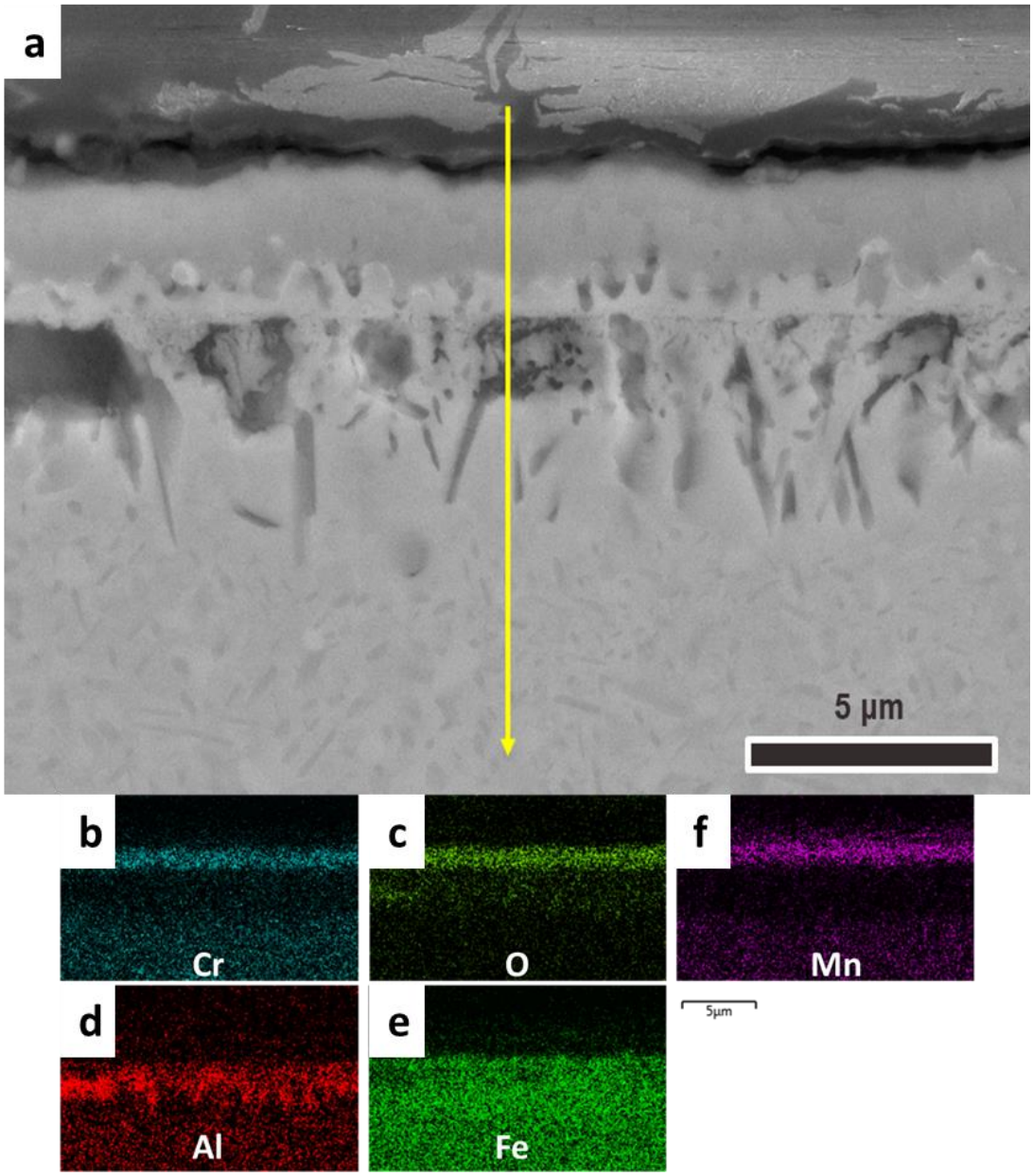

Figure 57 PGAA2-2, oxidized at 800°C for 72 h: (a) SEM of the cross-section, and the corresponding elemental maps for (b) Cr, (c) O, (d) Al, (e) Fe, and (f) Mn. A Cr oxide on top of Al oxide layer is formed. The yellow line denotes the linescan, the result of which are shown in Figure 59.

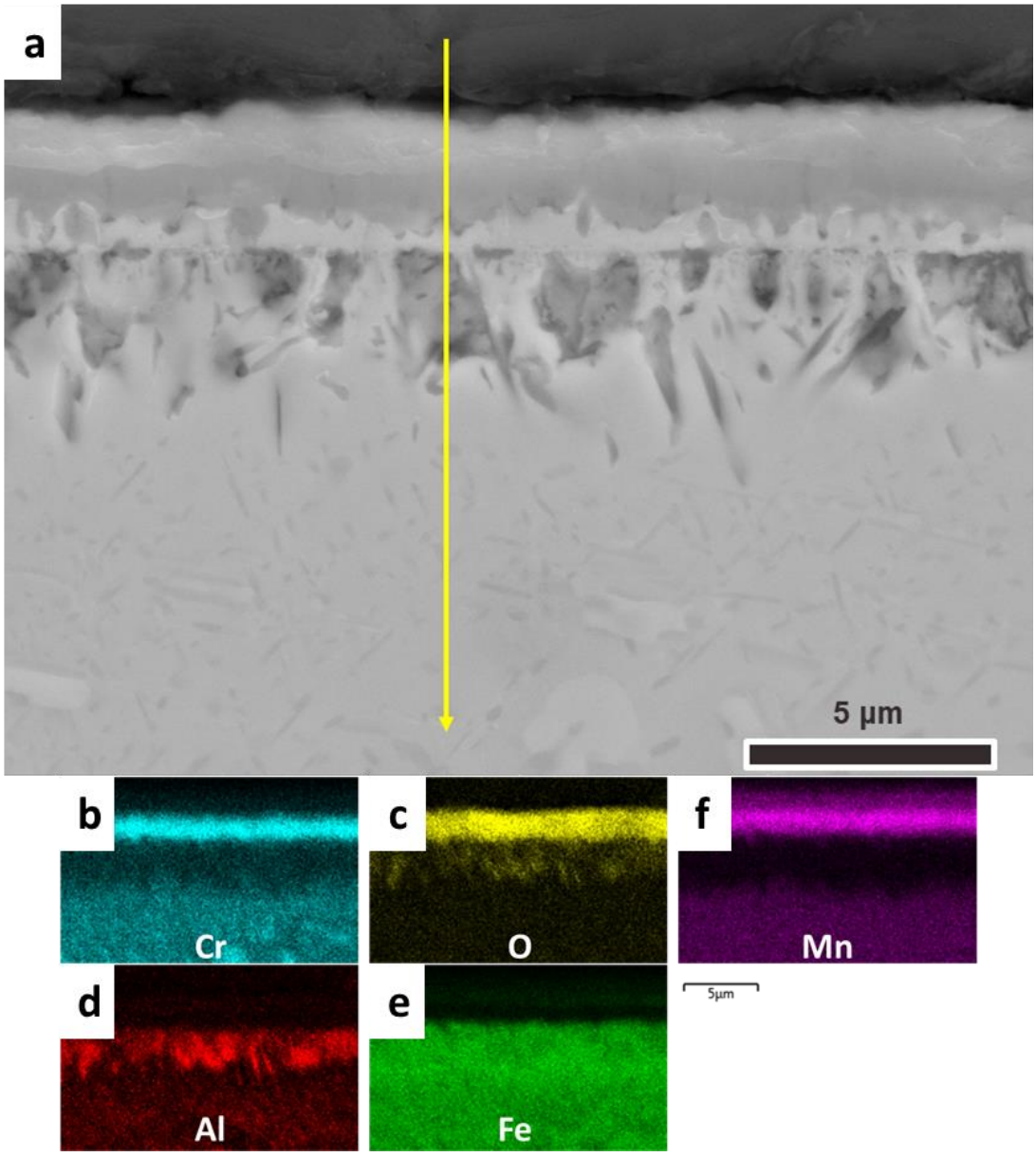

Figure 58 PGAA2-3, oxidized at 800°C for 72 h: (a) SEM of the cross-section, and the corresponding elemental maps for (b) Cr, (c) O, (d) Al, (e) Fe, and (f) Mn. A Cr oxide on top of Al oxide layer is formed. The yellow line denotes the linescan, the result of which are shown in Figure 59.

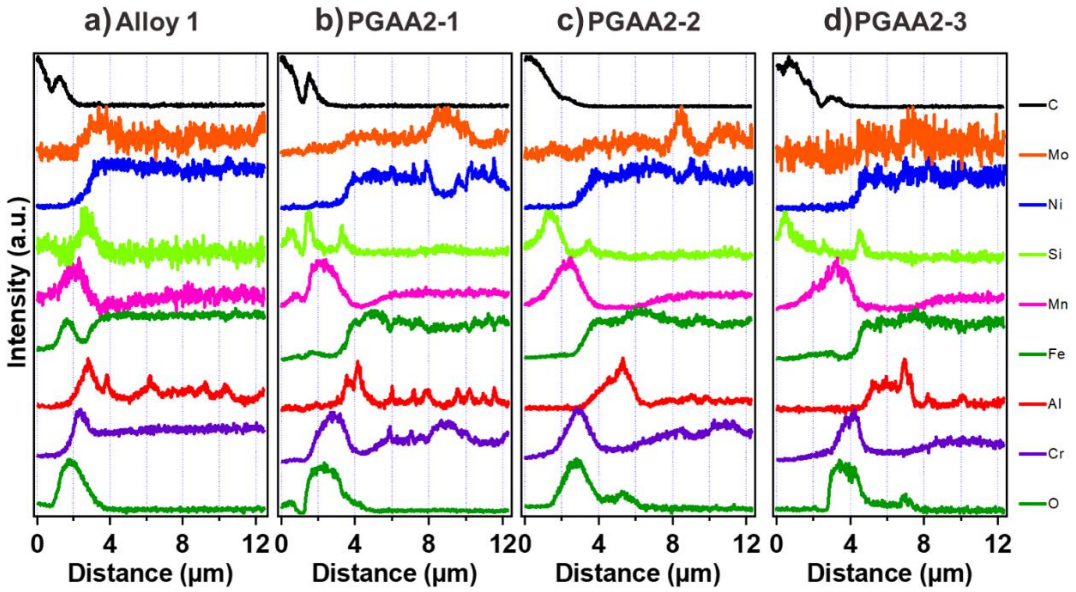

Figure 59 EDS scans along the lines shown in Figures 55 to 58, mapping out the elemental profiles after the oxidation at 800°C for 72 h. Formation of multi-layer scales can be witnessed in both alloys with certain similarities as explained in the text.

EDS Linescans of All Alloys Oxidized at 800 °C for 72 Hours

Figure 59 is the profile showing elemental change along the yellow lines in the cross-section images, obtained from EDS linescans. Carbon is presented as a measure to show where the epoxy finished and the sample starts. Mo exists in small quantities, but the linescans show a slight increase at the outmost surface for Alloy 1, possibly a mixture in the oxide scale. In the model alloys, Mn is deeper in the substrate, occasionally accompanied with Cr, and can be in form of an intermetallic precipitate. Ni appears to have a similar behavior in all the alloys, and probably doesn't have an important role in alumina-scale formation. Si, while quite difficult to be detected by EDS, seems to be mostly on the surface. This can be either due to the fact that Si can diffuse quickly to the surface and form in the oxide scale, or it is an impurity lodged between the carbon epoxy

and sample during the polishing process. Mn, in all case, has diffused quickly to the surface to form the oxide, and a Mn-denuded zone is observed underneath, usually where Al content is high. In Alloy 1, Fe appears to exist in the outmost oxide layer, while it is not the case for the model alloys. This could be because either the thicker scale that is present in model alloys forms faster and blocks the outward diffusion of Fe, or that an Fe-rich scale forms on the outmost but is so unstable that goes away quickly. The latter explanation seems less likely. As for Al, it is in the oxide scale in Alloy 1, next to Si and Mo, right below Fe, Mn, and then Cr, especially where an Fe-denuded zone is visible. Al-rich particles also appear in the substrate. In the model alloys, the Al layer is a bit deeper simply because the scale is thicker, and not necessarily where Fe is denuded. No noticeable relation between Al and Si or Mo is visible. Presence of Al-rich particles in the substrate is present. Cr is a major component in the oxide scale in all the alloys, but in the model alloys a denuded zone can be seen in the oxide where the Al content is high. This is not the case for Alloy 1. It can be concluded that the Al layer in the model alloys has higher Al content than the same layer does in Alloy 1. This will also explain why an Fe oxide doesn't exist in the scale of model alloys. Lastly, O shows where the oxide layer is, and in some case, a dual layer of Al oxide is present.

Summary and Conclusion of Short-Term Oxidation Tests

In summary, a series of custom-designed Alumina-Forming Austenitic Stainless Steels were exposed to oxidation experiments alongside a well-known alloy used as the baseline material, in order to study the alumina scale formation. The custom alloys was

designed based on thermodynamic calculations to have an austenite matrix, combined with oxide transport phenomena and third-element effect to form alumina scale, and Genetic Algorithm based optimization scheme (with the least-possible Ni content, no Nb, W, Ti, V, and Cu additions). The similarities between the two oxidation scales point to the conclusion that the custom designed alloys are oxidation resistance in the same manner as the well-known AFA-SS baseline material. These custom alloys have the smallest number and amount of alloying elements among the AFA-SSs reported in the literature. In particular, Nb, which has been deemed essential for formation of alumina scale, is not present in any of the custom alloys, nonetheless the alloys formed alumina scale and an Al-rich layer, while eliminating the potential problem of undissolvable NbC at the same time. Ni content is also lower than most other AFA-SS alloys, while still a fully austenitic matrix exists in the operating temperature, due to the extra Mn. Other expensive alloying elements, such as W and Hf, and Y are also absent. In general, these alloy can be considered as the leanest, most basic AFA-SS, and of importance as the simplest baseline alloys for further AFA-SS development. Effects of adding other alloying elements to this baseline on the oxidation/corrosion behavior can be systematically studied. Evolution and effect of different types of precipitates (e.g. carbides and nitrides, different Ni-Al precipitates facilitated by other elements) needs to be studied as well. A long-term oxidation test to further investigate the oxidation response will follow. This test will at the same condition (800 °C) for the same type of samples, only up to at least 1000 hours, interrupted to measure weight change during the oxidation.

Long-term Oxidation Test of Model Alloys vs. Control Alloy

The alloys behavior after a short-term oxidation test was evaluated in the previous section, and it was found that the alloys designed the oxidation model can successfully form an aluminum-rich layer near the surface. The characteristics of the scale on the model alloys were similar to that of the control sample, with the only difference that the control alloy also formed an iron oxide layer on the surface. In this section, a long-term oxidation test will be performed on the same alloys shown in Table 4 and Table 5, in the same conditions described in Figure 44 and Figures 52 to 54. The oxidation test was similarly done at 800 °C in lab atmosphere. Two samples from each alloy was prepared in coupons with dimension of 15 mm by 15 mm, and 2 mm thickness. These coupons were then polished down to 0.25 μm diamond suspension on the top surface. During the oxidation test, in specific time intervals, samples were taken out of the furnace and measured using a delicate scale to monitor the change in their masses. After the 1000 hours of the test, one sample from each alloy was cut in half and mounted in conductive epoxy and polished for microstructural studies using SEM and EDS, the results of which will be presented in the following chapters.

The results of mass change for all the alloys are presented in Figure 60. As it can be seen, the control alloys behave in a significantly different manner. The show a noticeably larger changes in mass, a loss in mass in this case. It is interesting to note that all three of the model alloys don't show a significant change in mass change compared to the control alloy. It must be added that the mass change value for the model alloys are the average of two samples for each alloy. A more detailed graph is presented in Figure 61.

As for the control samples represented in Figure 60, the mass change of each sample is plotted individually. A significant difference in the values of the mass change in observed even between the two samples of control alloy, despite them being identical initially. This points out a mechanism is at work which is very sensitive to sample variety. Concerning the noticeable mass loss for control alloys, based on the results obtained in the previous section, it can be deduced that the iron oxide that forms in this alloy is spalled off the higher temperatures at longer times, which leads to the mass loss. There is a possibility the scale that forms on this alloy is not as protective as the scale formed on the model alloys. It could be either because the scale is too thin at some point or even discontinuous. Such phenomenon can lead to a larger oxidation rate and a larger mass loss. It must be added that while the control alloy samples show different values for mass changes, the trend is similar, so a common mechanism is at work for both samples.

Figure 61 shows the mass change only for the model alloys, in smaller scales than Figure 60. The error bars in the graph depict the standard deviation of the mass change values obtained from measuring the two coupons from each alloy, and they show that both coupons for each alloy behave very similar and there is very little inconsistency. Keep in mind that the scale used here is in the order of milligrams on a surface of 225 mm^2 for each coupons. It is interesting to witness that although the model alloys were all quite close in chemistry, and their oxide scale after 72 hours were also very similar, their oxidation behavior is different, especially during the initial hours of oxidation. Figure 62 shows the mass change behavior for the model alloys up to 80 hours, corresponding the cross-sectional data obtained from Figures 56 to 58. PGAA2-1 shows a sudden decrease

in mass, signifying that a fast-growing scale is formed then spalled off, then its mass gradually increases. PGAA2-2 shows very similar behavior only smaller values of mass change. PGAA2-3, on the other hand, shows a mass gain, implying the formation of an oxide that is not spalled off. All three alloys appear to be constant in mass after the very first few hours of oxidation up to 80 hours, representing the similar scales shown in Figures 56 to 58.

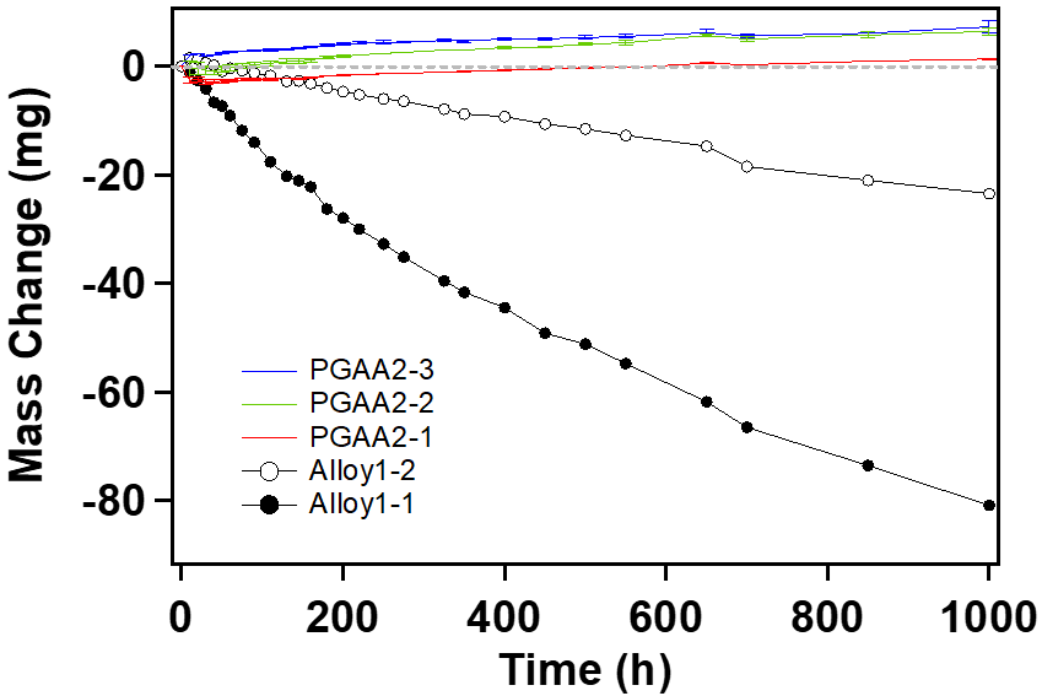

Figure 60 Mass change for all the alloys in the long-term oxidation test at 800 °C. The model alloys are average values of two samples, and the values for the control sample (Alloy1-1 and Alloy1-2) are presented individually.

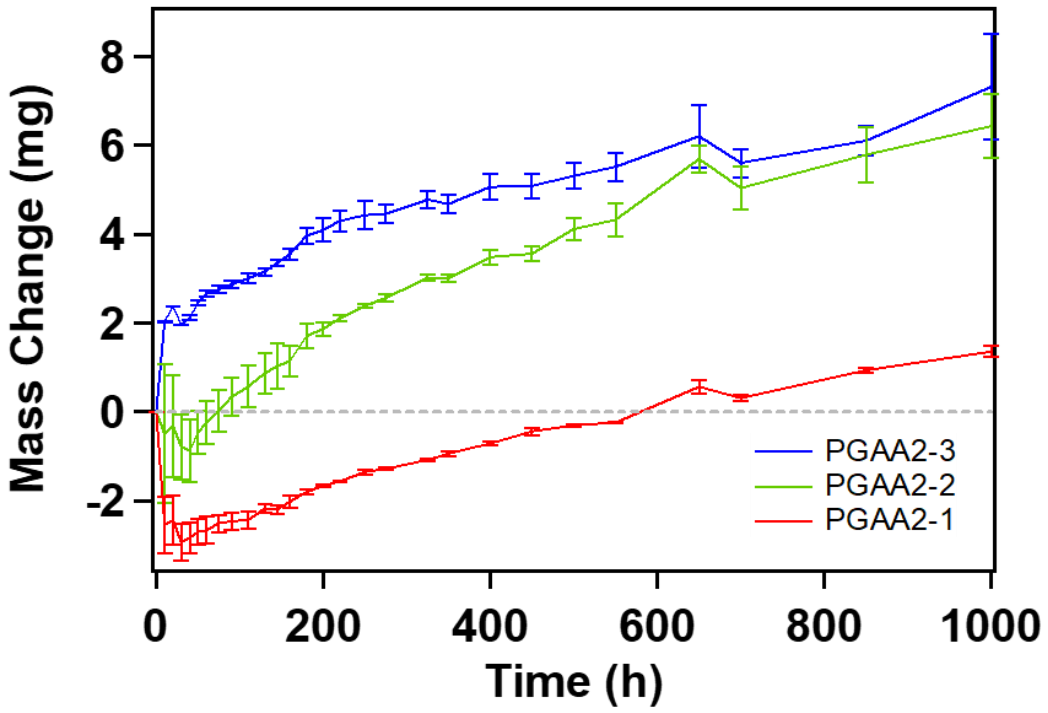

Figure 61 Mass change of only the model alloys on smaller scales, showing the standard deviation after averaging values of mass change for each alloy.

Back on Figure 61, the oxidation is observed to cause mass gain in all of the alloys, after the initial states of oxidation. It is noticed that this mass gain is very insignificant to the mass loss observed in the control alloy. The trend of the mass changes of the model alloys share similarities, for example all three alloys experience a small and sudden increase in mass at ~650 hours, followed by a momentary dip then the gradual increase. This can be used to deduce that the mechanisms active in the oxidation of these alloys are similar, passed the initial few hours. Finally, it appears that PGAA2-1, even though undergoes a mass loss initially, shows the smallest total mass change after 1000 hours.

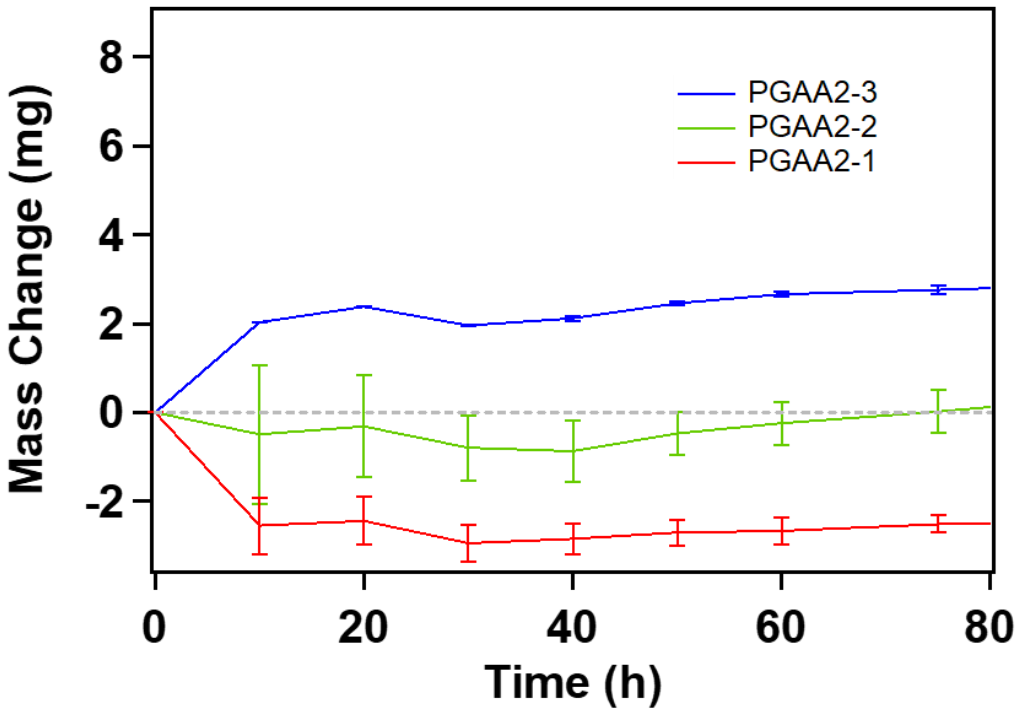

Figure 62 Mass change of only the model alloys on smaller scales, and only up to 80 hours, in correspondence with the cross-section data presented in Figures 56 to 58.

Alloy 1 (Control) Oxidized at 800 °C for 1000 Hours

The SEM image of the cross-section of Alloys 1 after oxidation at 800 °C for 100 hours is presented in Figure 63. Please note that the magnification of this micrograph is higher than that of Figure 55. The elemental maps produced by EDS are also presented. It can be seen a rather thin layer of oxide exists on the surface, mostly rich in Aluminum. An Al-denuded zone is witnessed underneath the scale. Precipitate containing Al, and Mo/Nb in other cases, are presented deeper in the substrate. The presence of a thin oxide scale consisting of only Al may be reason for the large mass loss of this alloy, which is the loss of the Cr/Mn/Fe oxide from the outermost of the scale.

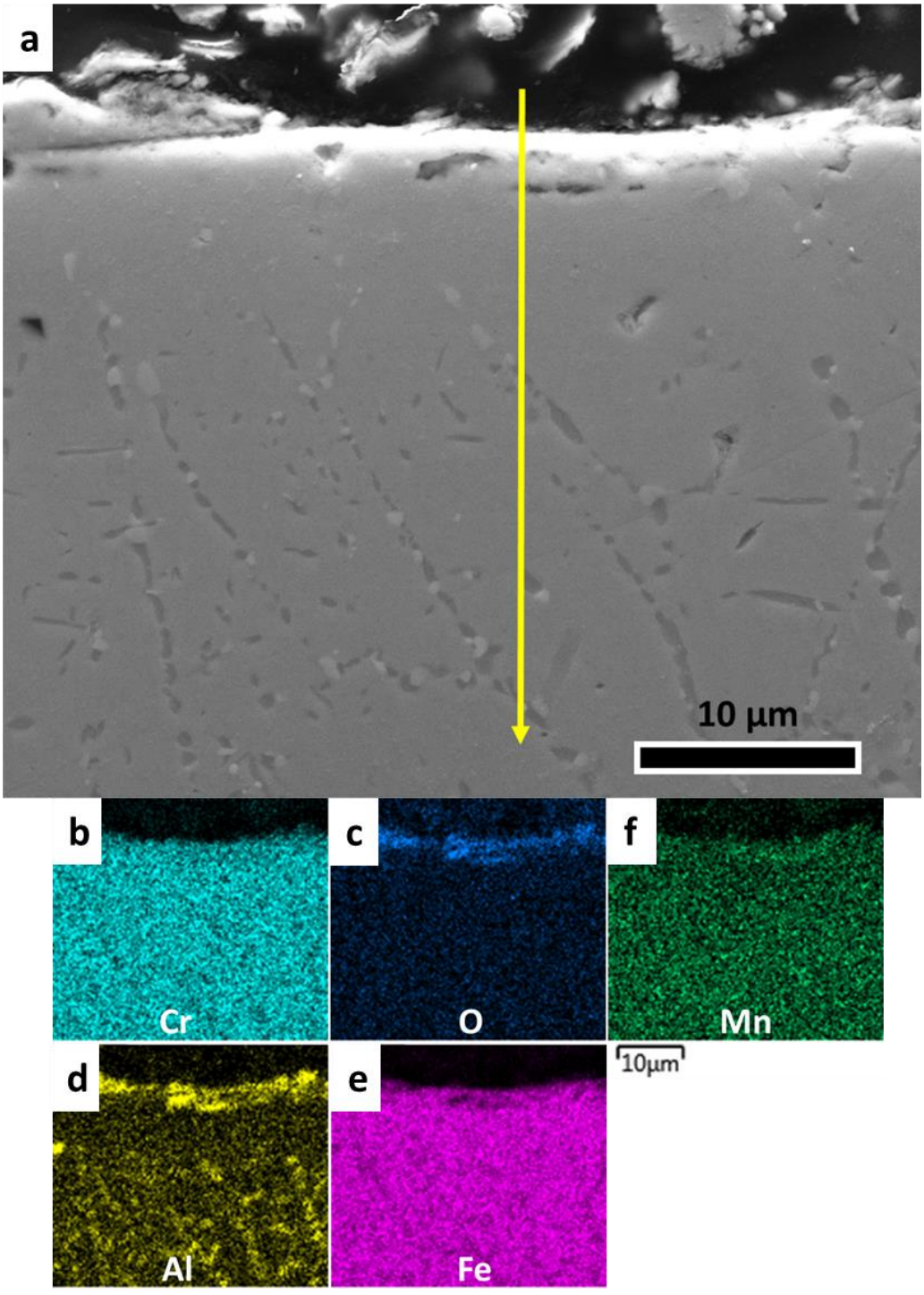

Figure 63 Alloy 1, oxidized at 800°C for 1000 h: (a) SEM of the cross-section, and the corresponding elemental maps for (b) Cr, (c) O, (d) Al, (e) Fe, and (f) Mn. A very thin scale of Al oxide formed that appears discontinuous at some locations. The yellow line denotes the linescan, the results of which are shown in Figure 67.

PGAA2-1 Oxidized at 800 °C for 1000 Hours

The SEM image of the cross-section of PGAA2-1 after oxidation at 800 °C for 1000 hours is presented in Figure 64. The elemental maps produced by EDS are also presented. A much thicker scale is observed on top of this alloy. A denuded zone followed by a precipitated zone is similarly visible. The oxide layer is mostly rich on Cr and Mn on the outermost of the scale, with small hints of Fe on the outer part of the scale layer. An Al-rich oxide exists underneath this layer. Followed by a denuded zone on top of the precipitation layer. It is very interesting to witness that the Fe-oxides and Mn-oxides are still present on the surface after 1000 hours. These oxides are expected to be instable at elevated temperatures and be spalled off. Two possible reasons may be suggested. It is possible that such scales are spalled off at more aggressive environments, such as present of water or other oxidizing species. However, the Mn/Fe oxides that were present on the Alloy-1 scale after 72 hours are spalled off after 1000 hours in the same environment. Another possible reason is that due to a higher outward diffusion of aluminum compared to oxygen, since it was a criterion used by the model to design the alloy, this alloy is still in the earlier stages of alumina-scale formation, i.e., the outer parts of scale rich in Fe and Mn have not spalled off yet. It is possible that even after longer periods of testing at the same condition, they will not spall off because the mass change trend doesn't change noticeably as seen in Figure 60. It can be concluded that the scale formed on top of a thick Al-rich scale is more oxidation resistant.

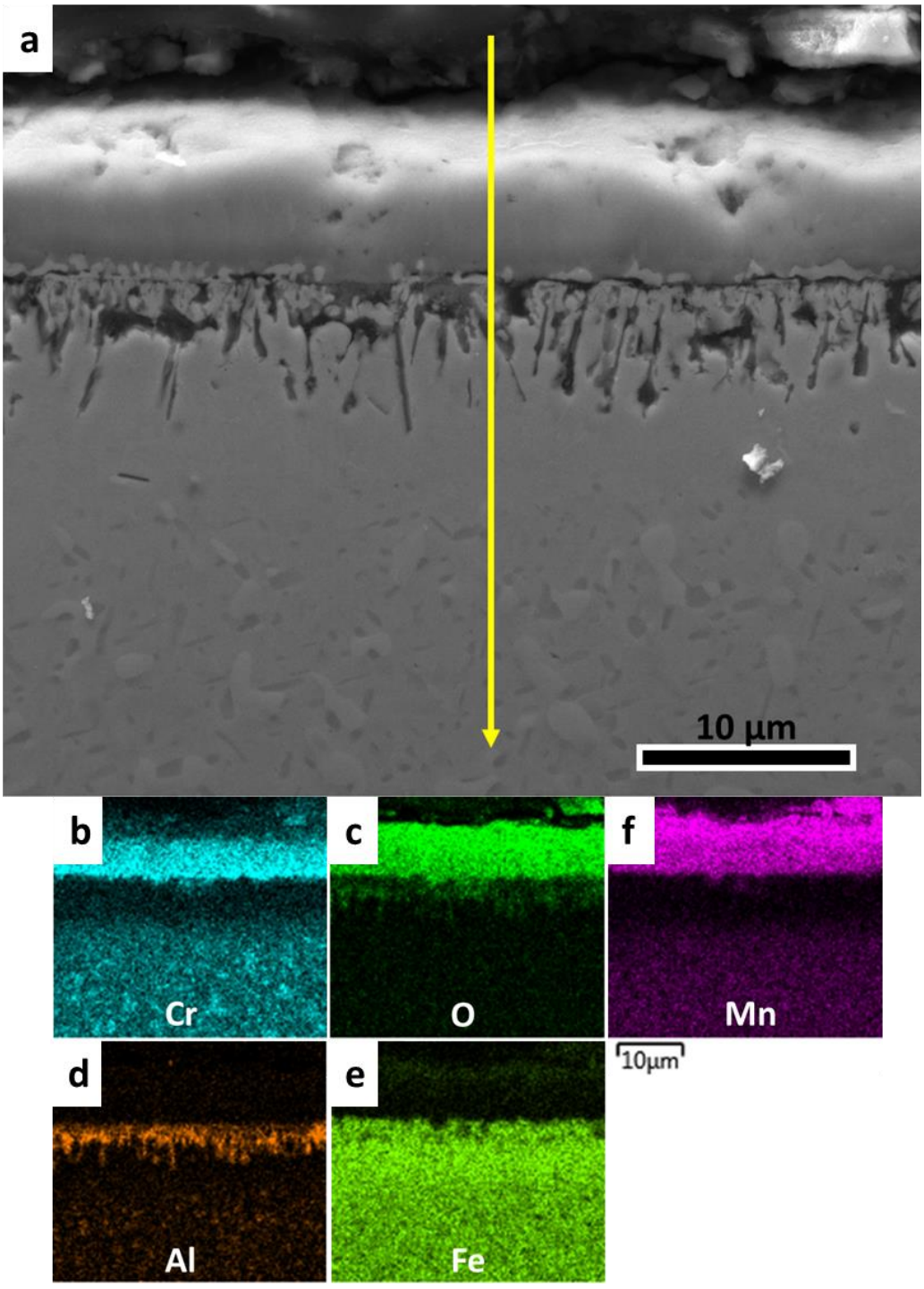

Figure 64 PGAA2-1, oxidized at 800°C for 1000 h: (a) SEM of the cross-section, and the corresponding elemental maps for (b) Cr, (c) O, (d) Al, (e) Fe, and (f) Mn. A Cr/Mn-rich oxide exists on the outermost with traces of Fe, followed by an Al-rich oxide layer. The yellow line denotes the linescan, the results of which are shown in Figure 67.

PGAA2-2 Oxidized at 800 °C for 1000 Hours

The SEM image of the cross-section of PGAA2-2 after oxidation at 800 °C for 1000 hours is presented in Figure 65. The elemental maps produced by EDS are also presented. This figure also depicts that a thick oxide layer has formed on the sample. This oxide is also rich in Mn and Cr, and similar to PGAA2-1, the Cr is more present deeper in the scale. The denuded zone and the precipitation zone appear deeper in this alloy, hinting that the diffusion occur faster. It must be reminded that, as presented in Figure 53, this alloy's initial condition was a mixture of ferrite and austenite, and depending on the diffusion of different species in austenite vs. ferrite, the mechanisms of oxidation might be different initially. However, as it was previously suggested, the diffusion of Al toward the surface at the early stages of oxidation leads to a lower Al content in the matrix right below the scale which is in favor of austenite stability. While the austenite is the stable phase at high temperatures, the samples are repeatedly cooled down to room temperature for mass measurements and heated back up. No noticeable evidence can be seen in these images that lead to a reason why PGAA2-1 initially shows a larger dip in mass change compared to PGAA2-2.

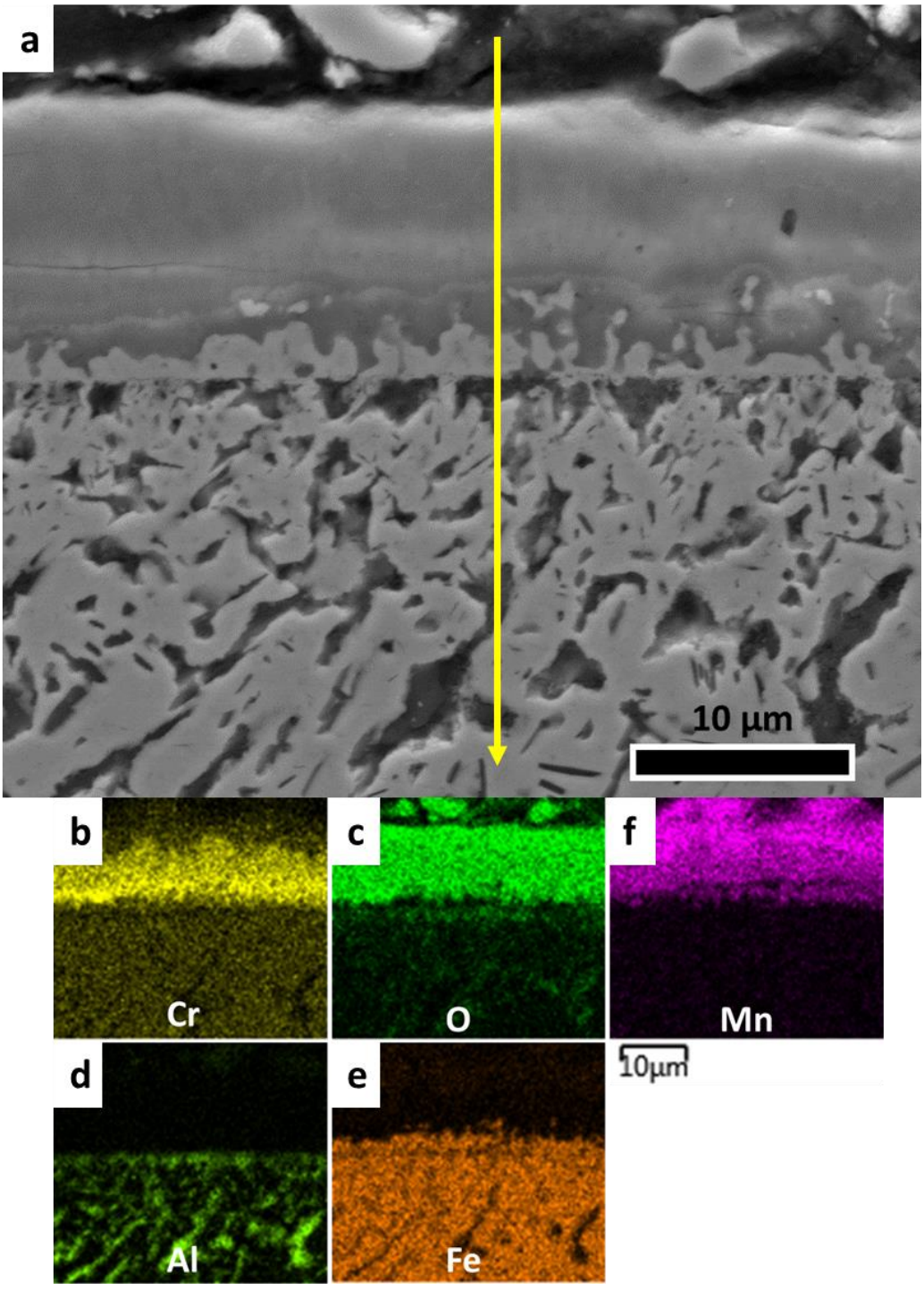

Figure 65 PGAA2-2, oxidized at 800°C for 1000 h: (a) SEM of the cross-section, and the corresponding elemental maps for (b) Cr, (c) O, (d) Al, (e) Fe, and (f) Mn. A thick Mn/Cr oxide layer exists on top of an Al-rich layer. The yellow line denotes the linescan, the results of which are shown in Figure 67.

PGAA2-3 Oxidized at 800 °C for 1000 Hours

The SEM image of the cross-section of PGAA2-3 after oxidation at 800 °C for 1000 hours is presented in Figure 66. The elemental maps produced by EDS are also presented. The oxide scale, similar to the two previous model alloys, is mostly Cr/Mn on the outer, followed by an Al-rich oxide layer. The layer thickness appears smaller than those of PGAA2-1 and PGAA2-2. The denuded zone is smaller and shallower than that of PGAA2-2 but similar to PGAA2-1. The precipitate layer is also shallower compared to PGAA2-2, and similar to PGAA2-1. This could be due to the austenite stability in PGAA2-1 and PGAA2-3. Since the thickness of the scale layer is smaller for PGAA2-3 compared to the other model alloys, it may be considered as a possible reason for this alloy to have the largest mass gain shown in Figure 61.

In general, the cross-section structures of the model alloys do not look noticeably different, despite their dissimilarities in their initial condition. This could also be reason for their similar oxidation behavior as represented by their mass change in Figure 60, and the fact that compared to the control alloy, these model alloys demonstrate a higher oxidation to resistance.

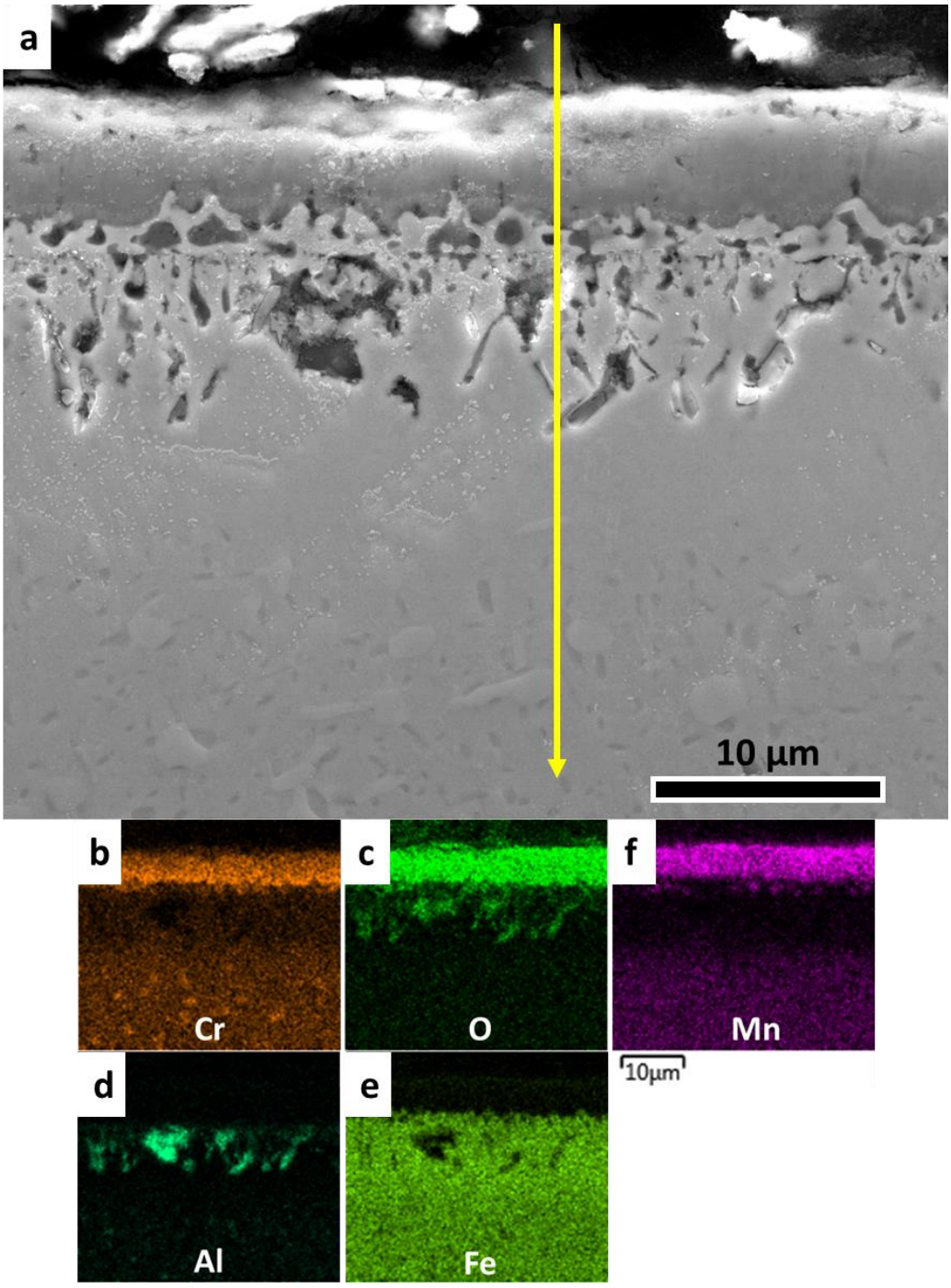

Figure 66 PGAA2-3, oxidized at 800°C for 1000 h: (a) SEM of the cross-section, and the corresponding elemental maps for (b) Cr, (c) O, (d) Al, (e) Fe, and (f) Mn. The oxide scale is Mn/Cr then Al, and not as thick. The yellow line denotes the linescan, the results of which are shown in Figure 67.

EDS Linescans of All Alloys Oxidized at 800 °C for 1000 Hours

Figure 67 is the profile showing elemental change along the yellow lines in the cross-section images, obtained from EDS linescans. Please not that these lines are approximately twice the length of the lines from the previous section. Carbon is presented as a measure to show where the epoxy finishes and the sample starts. Mo exists in small amount in the alloys, and not usually in the scale. Its content increases after 10-15 micron into the surface, for model alloys, denoting where the denuded zone is. Some peaks in Mo is observed which occurs when the linescan goes over a precipitate. Ni is also not present in the scale and has a small increase when after the denuded zone. It can be seen that some Ni-rich precipitates exist in the bulk of the alloy, usually also rich in Al and low Fe, implying a Ni-Ti intermetallic. In some spots along the lines, an increase in Ni is coinciding the Fe, but it is possibly mere due to the presence (or lack of) of other elements. Si mostly exists at the surface, either in form of impurity from the polishing, or since it diffused rapidly to the surface during oxidation. In some cases, it exists with Mn and/or Mo, probably in the form of precipitates shown in Figure 52. Mn is slightly higher in the scale for the control alloy, then slightly lowers as it reaches the denuded zone and the bulk, but for the model alloys, it usually is in outmost part of the oxide scale. A denuded zone of Mn is slightly visible, which can possibly be due to the presence of higher contents of other alloy. Occasionally, a Mn-rich precipitate is detected. Fe is slightly present in the oxide layer of the control alloy, possibly causing the significant mass loss of this alloy, especially since Fe content is not as high as it is after 72 hours shown in Figure 52. Fe appears to be effectively absent in the oxide region of the model alloys, especially where

the scale is mainly Mn/Cr-rich. The Fe content starts to rise as Mn/Cr is substituted with Al in the oxide scale, then reaches its maximum in the bulk of the material. Drops in Fe content in the bulk is witnessed when a region, probably a precipitates, rich in other elements are detected. Al exists in the oxide scale of the control alloy, not homogenously, usually where Mn is also high and Fe is low in content. Its content drops after the oxide scale and a few peaks for Ni-Ti precipitates are detected. In the model alloys, Al also exists alongside oxygen in the oxide layer, but starts to increase as Mn and Cr content decreases. Again Al-rich precipitates are detected in the substrate. Cr content in the oxide layer of Alloy 1 is smaller than the bulk, but it noticeably exists in the oxide of the model alloys. The Cr content slightly increases as the Mn content slightly decreases, and drops down when Al shows up in the scale of the model alloys. No Cr-rich particles were detected in the linescans although in the maps, some Cr-rich particles are visible deeper into the bulk of the material, especially for PGAA2-1 and PGAA2-3 which are fully austenitic. Finally, the oxygen profile shows that the thickness of the oxide layer in the control alloy is about 5 µm. The thickness is about 12 µm, 22 µm, and 15 µm in PGAA2-1, PGAA2-2, and PGAA2-3, respectively. The O profile in the model alloys usually shows a higher oxygen region followed by a lower oxygen region. If this fact is used to assume that the oxidation process of Al underneath the Mn/Cr oxide is not fully completed, this may point to a lower oxidation mechanism in the model alloys, which could justify their lower mass changes during the long-term oxidation test compared to the control alloy.

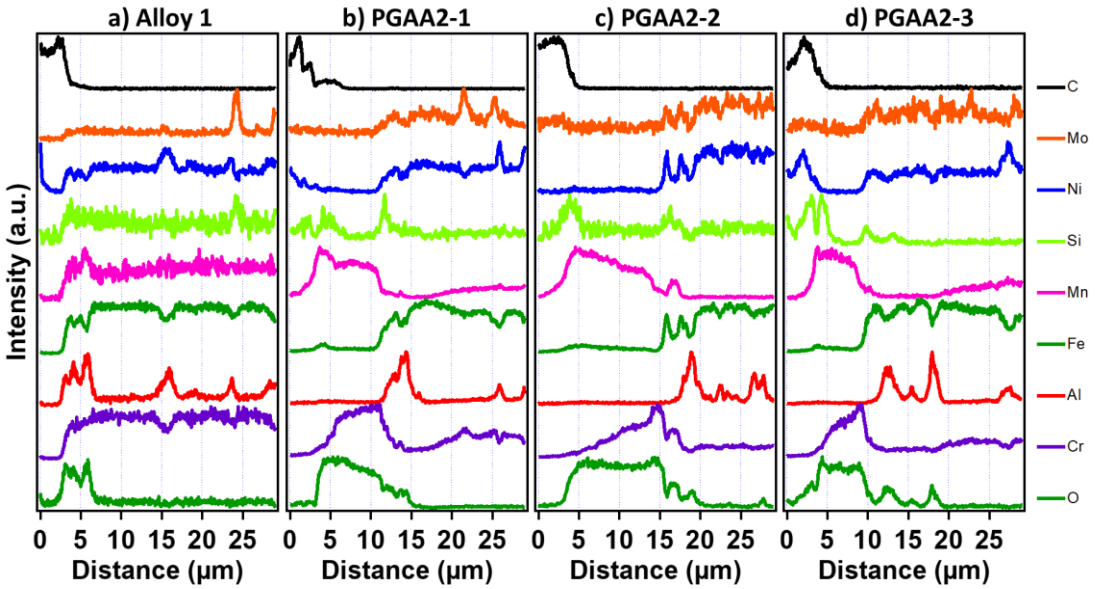

Figure 67 EDS scans along the lines shown in Figures 63 to 66, mapping out the elemental profiles after the oxidation at 800°C for 1000 h. Formation of multi-layer scales can be witnessed in both alloys with certain similarities as explained in the text.

Summary and Conclusion of Long-Term Oxidation Tests

The long-term oxidation tests were performed on the same alloys in the similar condition as the short-term tests. Two samples out of each alloy was prepared and placed in the furnace at 800 °C for up to 1000 hours. Samples were removed periodically and measured using a scale to monitor the mass change. After the completion of the oxidation test, samples were cut in half and mounted and studied using electron microscopy to investigate the scale layers that have formed. The mass change vs. time for the alloys show that the samples from the control alloy demonstrate a significant mass loss, meaning that an unstable form of oxide forms continuously on the surface and spalls off, causing the constant mass loss. Based on the observations of the oxide scales that form during the short-term oxidation test on the control and the model alloys, it could be deduced that an

iron-rich oxide forms in the control alloys that does not in the model alloys, and this scale is unstable at high temperatures and long durations, and spalls off. The mass change up to 80 hours of the test is not significantly larger for Alloys 1 compared to the model alloys, but it continuously decreases in a faster rate than the model alloy. It is possibly because Fe (or other elements such as Mn) keeps diffusing to the surface to form an unstable oxide and then spall off. It was also witnessed that while the trend of mass loss in both samples of Alloy 1 showed similarities, the values in the mass loss were noticeably different for the two samples, so it can be concluded that the mechanism responsible for the loss of mass in the control alloy may depend on other parameters such as homogeneity of the alloying elements. The mass change of the model alloys were noticeably smaller than the control alloy, and the values for both samples of each alloy were quite consistent. PGAA2-1 showed an initial mass loss, but continued into mass gain, and ended with the smallest change in mass after 1000 hours. Cross-section images of the sample after the oxidation showed that the scale on the control alloy is significantly smaller than those of the model alloys. Also, the oxide layer of the control alloy had higher contents of Fe and lower Cr compared to the model alloys, which could be the possible reason for the larger mass loss of this alloy. The scale in the model alloys were a Mn/Cr-rich oxide on the outmost part of the scale, followed by an Al-rich part. The configuration of the oxide scales were quite similar in the model alloys, despite their initial differences, which explains why their behavior is quite similar at the later stages of oxidation.

In conclusion, the results showed the model alloys demonstrate a higher oxygen resistance than the control alloys does. While this oxidation resistant might be not as

significant if tested under more aggressive oxidation condition, it was found out the basic ideas that the model used for designing these alloy (which are models based on the thermodynamics and kinetics of the oxidation), were successful at understanding and predicting the oxidation behavior. As mentioned in the previous section, the model alloys have smaller alloying elements compared to other alumina-forming steels present in the literature. Alloys proposed by this model can be considered the “leanest” alumina-forming steels available, and can be used as a basis for further alloy design.

CHAPTER V

SUMMARY AND CONCLUSIONS

The purpose of this work was to find a way to improve the high-temperature performance of 316 austenitic stainless steel. This quest was driven by the need for a high-temperature structural alloy which is also inexpensive. Such an alloy may find applications in many industrial fields, especially in power production. This high-temperature performance expected of such an alloy can be divided into mechanical strength and oxidation resistance. Austenitic stainless steel is good candidate based on its performance at intermediate temperatures, and the promise of improvement at higher temperatures. For improving the mechanical strength, barriers to dislocation motion (or creep mechanisms) needs to be created in the steel which are stable and effective at elevated temperatures. As for the oxidation resistance, it has been proposed that aluminum oxide, as opposed to chromium oxide on conventional stainless steels, is more stable and protective at higher temperatures, and therefore, alumina-forming austenitic stainless steels have been proposed. In this work, we hypothesize that if such an alloy exists and shows this high-temperature performance, it must have four microstructural features: 1. an austenite matrix for high-temperature stability and strength, 2. high volume fraction of low-energy high-angle grain boundaries to (e.g. coherent twin boundaries) increase the strength at high temperature without total loss of ductility, 3. precipitates that are stable and controllable at high temperatures to pin these boundaries and grain boundaries and impede with dislocation glide, 4. alumina scale on the surface for oxidation resistance. But it is unlikely to find an alloy that possesses all of these attributes, because most of them are conceptually

contradictory. For example, addition of aluminum to from alumina may stabilize ferrite over austenite, increase SFE and make twinning impossible, and create uncontrollable precipitates. However, we would like to investigate whether these features in a hypothetical steel is even beneficial to the high-temperature performance. In other words, we are going to investigate whether: A) Thermally-stable deformation twins contribute to high-temperature strength, and B) There is a way to model the oxidation and design suitable alumina forming austenitic stainless steels.

For the first part, a thermo-mechanical cycling process was designed and performed on 316 austenitic stainless steel in order to create a high-volume fraction of deformation twins, which are thermally-stable up to 100 °C, in an austenite matrix with relatively low dislocation density. Fully annealed samples (AA) and highly twinned samples (TW) were tested at extreme temperatures (-100 °C to 500 °C) and results were compared. It was found out that the hierarchical structure created by this process improved the mechanical strength at all temperatures, without a total loss in ductility. Particularly, it was found out that the relative increase in the yield strength due to this unique structure increased as the temperature increased, and the increase in strength showed a peculiar strength against increase of temperature. It was later deduced that, among the contributions of all the structural elements present, the role of thermally-stable twins is the most helpful in enhancing high-temperature strength. In addition, it was discovered that this structure increases the flow strength beyond the ultimate tensile strength, without the total loss of ductility, unlike the usual strengthening effect of conventional cold-working. The fracture surfaces at different temperatures also showed that although a twinned structure

experiences smaller necking, the microstructure of the surface is not significantly different from the fully annealed structure. This unique structure is expected to perform well under creep condition, and benefit immensely from precipitation strengthening, especially where the precipitates coarsen in conventional matrices.

As for the oxidation resistance, in collaboration with a computational alloy design group, an oxidation model for the alumina-forming austenitic steels was developed based on the thermodynamics and kinetics of the oxidation. An optimized alloy was prosed based on the model that has the lowest amount of alloying compared with the other alumina-forming steels in literature. Alloys based on the model was ordered and produced from different producers with slightly different chemical compositions that, in some case, cause unfavorable conditions for the alloys. In other to compare the oxidation resistance, a control alloy was also produced based on the chemical composition of an alumina-forming steel in the literature already demonstrating successful alumina-formation. The control alloy and the model alloys were tested at 800 °C for 72 hours, where the control alloy had already demonstrated alumina-formation. The cross-section EDS data of the control alloy showed that it has a scale consisting of Cr, Mn, Fe, and Al oxides, while the model alloys had a thicker scale, with Mn and Cr richer on the top, followed by an Al-rich layer. This structure of the model alloys were consistent with the predictions of the model. A long-term oxidation test was performed at the same condition except for 1000 hours instead of 72. The control alloys showed a significant and inconsistent mass loss during the oxidation, while the model alloys demonstrated a much smaller change in mass, with similar trends in mass change especially in later stages of oxidation. The smaller mass

change could be due to the lack of Fe in the model alloys based on the short-term results, or because the control alloy has a thinner (and possibly discontinuous) alumina scale. The initial differences in the oxidation trend of the model alloys could be due to their initial structure because of their small differences in chemistry. Similarly, the cross-sections of the samples after the long-term oxidation test were studied. The control alloy showed a thinner scale consisting mainly of Al/Mn oxides, while the model alloys had thicker layers of Mn,Cr oxides on top of Al-rich layers. Based on these findings, it could be said the scale formed on the model alloys are either more stable (and protective), or the kinetics and rate of the oxidation of the model alloys are significantly slower than the control alloy. In conclusion, it was deduced that the model was successful at predicting the oxidation behavior and designing the "leanest" alumina-forming austenitic stainless steel. This alloy (and the oxidation model) can be used as a basis for further studies in this group of steels.

At the end of it all, when looking at the mechanical response and the oxidation behavior of the austenitic steels in perspective, it appears unlikely that we can combine the aspects of thermally-stable twins and a chemistry capable of alumina-scale formation. While the change in SFE is difficult to calculate or even monitor, it is expected that the addition of Al to the steel increases the SFE beyond the limits of twin formation. However, if there exists a small window where the proposed hypothetical alloy can be found and produced, the methodology presented in this work would be the best road map to achieve the end. Our best bet to create such an alloy is to use the oxidation model to find an alloy chemistry that is capable of alumina-scale formation alongside appropriate fractions of beneficial precipitates, while the SFE is in a region capable of deformation twinning. Then

following the same principle for creating a high volume density of thermally-stable twins in a matrix that the model has predicted to be fully austenitic, finished by a heat treatment to form the precipitates on the twin to make both the particles and the boundaries more stable and homogenous. Such an alloy can be expected to match the performance of Ni-based alloys.

REFERENCES

[1] S. Sridhar, P. Rozzelle, B. Morreale, D. Alman, Materials challenges for advanced combustion and gasification fossil energy systems, Metallurgical and Materials Transactions A 42(4) (2011) 871-877.

[2] G. Chai, J.-O. Nilsson, M. Boström, J. Högberg, U. Forsberg, Advanced Heat Resistant Austenitic Stainless Steels, Advanced Steels, Springer2011, pp. 385-397.

[3] Y. Yamamoto, M.P. Brady, Z.P. Lu, P.J. Maziasz, C.T. Liu, B.A. Pint, K.L. More, H. Meyer, E.A. Payzant, Creep-resistant, Al2O3-forming austenitic stainless steels, Science 316(5823) (2007) 433-436.

[4] M.P. Brady, Y. Yamamoto, M.L. Santella, P.J. Maziasz, B.A. Pint, C. Liu, Z. Lu, H. Bei, The development of alumina-forming austenitic stainless steels for high-temperature structural use, JOM 60(7) (2008) 12-18.

[5] G.Y. Lai, High temperature corrosion of engineering alloys, (1990).

[6] B. Gleeson, Corrosion and Environmental Degradation of Materials, V. II, Materials Science and Technology V 19 (2000) 174-228.

[7] E.J. Opila, Volatility of common protective oxides in high-temperature water vapor: current understanding and unanswered questions, Materials Science Forum, Trans Tech Publ, 2004, pp. 765-774.

[8] R. Lagneborg, R. Attermo, Creep of austenitic 20% Cr/35% Ni stainless steels at low stresses, Journal of Materials Science 4(3) (1969) 195-201.

[9] R. Viswanathan, W. Bakker, Materials for ultrasupercritical coal power plants—Boiler materials: Part 1, Journal of Materials Engineering and Performance 10(1) (2001) 81-95.

[10] R. Rautio, S. Bruce, Alloy for ultrasupercritical coal fired boilers, Advanced materials & processes 166(4) (2008) 35-37.

[11] T. Gladman, The physical metallurgy of microalloyed steels, Maney Pub1997.

[12] V.T. Ha, W.S. Jung, J.Y. Suh, Improved Creep Behavior of a High Nitrogen Nb-Stabilized 15Cr-15Ni Austenitic Stainless Steel Strengthened by Multiple Nanoprecipitates, Metallurgical and Materials Transactions a-Physical Metallurgy and Materials Science 42A(11) (2011) 3378-3385.

[13] P.J. Maziasz, J.P. Shingledecker, B.A. Pint, N.D. Evans, Y. Yamamoto, K. More, E. Lara-Curzio, Overview of creep strength and oxidation of heat-resistant alloy sheets and foils for compact heat exchangers, Journal of turbomachinery 128(4) (2006) 814-819.

[14] W.S. Jung, J.Y. Suh, Improved Creep Behavior of a High Nitrogen Nb-Stabilized 15Cr-15Ni Austenitic Stainless Steel Strengthened by Multiple Nanoprecipitates, Metallurgical and Materials Transactions A 42(11) (2011) 3378-3385.

[15] Q. Wu, Microstructural evolution in advanced boiler materials for ultra-supercritical coal power plants, University of Cincinnati, 2006.

[16] M. Harper, M. Ducasse, D. Young, Cyclic oxidation plus carburization of heat-resistant alloys, Corrosion 51(3) (1995) 191-200.

[17] A. La Fontaine, H.-W. Yen, P. Trimby, S. Moody, S. Miller, M. Chensee, S. Ringer, J. Cairney, Martensitic transformation in an intergranular corrosion area of austenitic stainless steel during thermal cycling, Corrosion Science 85 (2014) 1-6.

[18] A. La Fontaine, H.-W. Yen, P.J. Felfer, S.P. Ringer, J.M. Cairney, Atom probe study of chromium oxide spinels formed during intergranular corrosion, Scripta Materialia 99 (2015) 1-4.

[19] D. Zhou, W. Zhao, H. Mao, Y. Hu, X. Xu, X. Sun, Z. Lu, Precipitate characteristics and their effects on the high-temperature creep resistance of alumina-forming austenitic stainless steels, Materials Science and Engineering: A 622 (2015) 91-100.

[20] Y. Murata, S. Ohashi, Y. Uematsu, Recent Trends in the Production and Use of High Strength Stainless Steels, ISIJ international 33(7) (1993) 711-720.

[21] M. Pohl, O. Storz, T. Glogowski, Effect of intermetallic precipitations on the properties of duplex stainless steel, Materials characterization 58(1) (2007) 65-71.

[22] S. Erlach, H. Leitner, M. Bischof, H. Clemens, F. Danoix, D. Lemarchand, I. Siller, Comparison of NiAl precipitation in a medium carbon secondary hardening steel and C-free PH13-8 maraging steel, Materials Science and Engineering: A 429(1) (2006) 96-106.

[23] D. Escriba, E. Materna-Morris, R. Plaut, A.F. Padilha, Intermetallic Phase Precipitation in Duplex Stainless Steels during High Temperature Exposition, Materials Science Forum, Trans Tech Publ, 2010, pp. 478-484.

[24] Y. Yamamoto, M.L. Santella, M.P. Brady, H. Bei, P.J. Maziasz, Effect of alloying additions on phase equilibria and creep resistance of alumina-forming austenitic stainless steels, Metallurgical and Materials Transactions A 40(8) (2009) 1868-1880.

[25] I. Karaman, G. Yapici, Y. Chumlyakov, I. Kireeva, Deformation twinning in difficult-to-work alloys during severe plastic deformation, Materials Science and Engineering: A 410 (2005) 243-247.

[26] W. Xu, P. Rivera-Díaz-del-Castillo, W. Wang, K. Yang, V. Bliznuk, L. Kestens, S. Van der Zwaag, Genetic design and characterization of novel ultra-high-strength stainless steels strengthened by Ni3Ti intermetallic nanoprecipitates, Acta Materialia 58(10) (2010) 3582-3593.

[27] W. Sha, A. Cerezo, G. Smith, Phase chemistry and precipitation reactions in maraging steels: Part I. Introduction and study of Co-containing C-300 steel, Metallurgical Transactions A 24(6) (1993) 1221-1232.

[28] G. Bokuchava, I. Papushkin, V. Sumin, A. Balagurov, D. Sheptyakov, Investigation of microstrain in dispersion-strengthened steels, Physics of the Solid State 56(1) (2014) 166-170.

[29] H. Bhadeshia, R. Honeycombe, Steels: Microstructure and Properties: Microstructure and Properties, Butterworth-Heinemann2011.

[30] G. Yapici, I. Karaman, Z. Luo, H. Maier, Y. Chumlyakov, Microstructural refinement and deformation twinning during severe plastic deformation of 316L stainless steel at high temperatures, Journal of materials research 19(08) (2004) 2268-2278.

[31] H. Ueno, K. Kakihata, Y. Kaneko, S. Hashimoto, A. Vinogradov, Nanostructurization assisted by twinning during equal channel angular pressing of metastable 316L stainless steel, Journal of materials science 46(12) (2011) 4276-4283.

[32] Y. Idell, G. Facco, A. Kulovits, M. Shankar, J. Wiezorek, Strengthening of austenitic stainless steel by formation of nanocrystalline γ-phase through severe plastic deformation during two-dimensional linear plane-strain machining, Scripta Materialia 68(9) (2013) 667-670.

[33] N. De Vincentis, M. Avalos, A. Kliauga, V. Sordi, N. Schell, H. Brokmeier, R. Bolmaro, Deformation analysis on F138 austenitic stainless steel: ECAE and rolling, IOP Conference Series: Materials Science and Engineering, IOP Publishing, 2014, p. 012057.

[34] Z. Pakiela, H. Garbacz, M. Lewandowska, A. Druzycka-Wiencek, M. Sus-Ryszkowska, W. Zielinski, K.J. Kurzydlowski, Structure and properties of nanomaterials produced by severe plastic deformation, Nukleonika 51 (2006) S19-S25.

[35] S. Scheriau, Z. Zhang, S. Kleber, R. Pippan, Deformation mechanisms of a modified 316L austenitic steel subjected to high pressure torsion, Materials Science and Engineering: A 528(6) (2011) 2776-2786.

[36] R.Z. Valiev, A. Korznikov, R. Mulyukov, Structure and properties of ultrafine-grained materials produced by severe plastic deformation, Materials Science and Engineering: A 168(2) (1993) 141-148.

[37] S.V. Dobatkin, On the increase of thermal stability of ultrafine grained materials obtained by severe plastic deformation, Materials Science Forum, Trans Tech Publ, 2003, pp. 2699-2704.

[38] O. Bouaziz, C. Scott, G. Petitgand, Nanostructured steel with high work-hardening by the exploitation of the thermal stability of mechanically induced twins, Scripta Materialia 60(8) (2009) 714-716.

[39] M.K. Abadi, A. Najafizadeh, A. Kermanpur, Y. Mazaheri, S.S. Attar, A. Monshi, M. Meratian, A. Arefpour, A. Saidi, T. Khayamian, Effect of annealing process on microstructure and mechanical properties of high manganese austenitic TWIP steel.

[40] D.B. Santos, A.A. Saleh, A.A. Gazder, A. Carman, D.M. Duarte, É.A. Ribeiro, B.M. Gonzalez, E.V. Pereloma, Effect of annealing on the microstructure and mechanical properties of cold rolled Fe–24Mn–3Al–2Si–1Ni–0.06 C TWIP steel, Materials Science and Engineering: A 528(10) (2011) 3545-3555.

[41] A.A. Gazder, A.A. Saleh, E.V. Pereloma, Microtexture analysis of cold-rolled and annealed twinning-induced plasticity steel, Scripta Materialia 65(6) (2011) 560-563.

[42] A.A. Saleh, E.V. Pereloma, A.A. Gazder, Texture Evolution during Recrystallisation of Cold Rolled TWIP Steel, Materials Science Forum, Trans Tech Publ, 2012, pp. 647-650.

[43] T. Watanabe, An approach to grain boundary design for strong and ductile polycrystals, Res Mechanica 11(1) (1984) 47-84.

[44] V. Randle, Mechanism of twinning-induced grain boundary engineering in low stacking-fault energy materials, Acta materialia 47(15) (1999) 4187-4196.

[45] M. Shimada, H. Kokawa, Z. Wang, Y. Sato, I. Karibe, Optimization of grain boundary character distribution for intergranular corrosion resistant 304 stainless steel by twin-induced grain boundary engineering, Acta Materialia 50(9) (2002) 2331-2341.

[46] V. Randle, Twinning-related grain boundary engineering, Acta materialia 52(14) (2004) 4067-4081.

[47] D. Raabe, M. Herbig, S. Sandlöbes, Y. Li, D. Tytko, M. Kuzmina, D. Ponge, P.-P. Choi, Grain boundary segregation engineering in metallic alloys: A pathway to the design of interfaces, Current Opinion in Solid State and Materials Science 18(4) (2014) 253-261.

[48] A. Forsström, J. Talonen, T. Saukkonen, H. Hänninen, Grain boundary engineering of metastable 204Cu, 301, and 301LN austenitic stainless steels to improve their sensitization resistance, Materials and Corrosion (2014).

[49] S. Mandal, A. Bhaduri, V.S. Sarma, One-step and iterative thermo-mechanical treatments to enhance Σ3 n boundaries in a Ti-modified austenitic stainless steel, Journal of Materials Science 46(1) (2011) 275-284.

[50] L. Tan, K. Sridharan, T.R. Allen, R.K. Nanstad, D.A. McClintock, Microstructure tailoring for property improvements by grain boundary engineering, Journal of Nuclear Materials 374(1) (2008) 270-280.

[51] S. Bechtle, M. Kumar, B.P. Somerday, M.E. Launey, R.O. Ritchie, Grain-boundary engineering markedly reduces susceptibility to intergranular hydrogen embrittlement in metallic materials, Acta materialia 57(14) (2009) 4148-4157.

[52] V. Randle, Grain boundary engineering: an overview after 25 years, Materials Science and Technology 26(3) (2010) 253-261.

[53] L. Tan, K. Sridharan, T. Allen, Altering corrosion response via grain boundary engineering, Materials Science Forum, Trans Tech Publ, 2008, pp. 409-418.

[54] P. Lin, G. Palumbo, U. Erb, K. Aust, Influence of grain boundary character distribution on sensitization and intergranular corrosion of alloy 600, Scripta Metallurgica et materialia 33(9) (1995) 1387-1392.

[55] K. Kurihara, H. Kokawa, S. Sato, Y. Sato, H. Fujii, M. Kawai, Grain boundary engineering of titanium-stabilized 321 austenitic stainless steel, Journal of materials science 46(12) (2011) 4270-4275.

[56] S. Sinha, D.-I. Kim, E. Fleury, S. Suwas, Effect of grain boundary engineering on the microstructure and mechanical properties of copper containing austenitic stainless steel, Materials Science and Engineering: A 626 (2015) 175-185.

[57] D. Engelberg, F. Humphreys, T. Marrow, The influence of low-strain thermo-mechanical processing on grain boundary network characteristics in type 304 austenitic stainless steel, Journal of microscopy 230(3) (2008) 435-444.

[58] Y. Jin, M. Bernacki, G. Rohrer, A.D. Rollett, B. Lin, N. Bozzolo, Formation of annealing twins during recrystallization and grain growth in 304L austenitic stainless steel, Materials Science Forum, Trans Tech Publ, 2013, pp. 113-116.

[59] K. Lu, F. Yan, H. Wang, N. Tao, Strengthening austenitic steels by using nanotwinned austenitic grains, Scripta Materialia 66(11) (2012) 878-883.

[60] F. Yan, G. Liu, N. Tao, K. Lu, Strength and ductility of 316L austenitic stainless steel strengthened by nano-scale twin bundles, Acta Materialia 60(3) (2012) 1059-1071.

[61] I.J. Beyerlein, X. Zhang, A. Misra, Growth twins and deformation twins in metals, Annual Review of Materials Research 44 (2014) 329-363.

[62] I. Karaman, H. Sehitoglu, K. Gall, Y. Chumlyakov, H. Maier, Deformation of single crystal Hadfield steel by twinning and slip, Acta materialia 48(6) (2000) 1345-1359.

[63] I. Karaman, H. Sehitoglu, Y.I. Chumlyakov, H. Maier, I. Kireeva, Extrinsic stacking faults and twinning in Hadfield manganese steel single crystals, Scripta materialia 44(2) (2001) 337-343.

[64] X. Wang, H. Zurob, J. Embury, X. Ren, I. Yakubtsov, Microstructural features controlling the deformation and recrystallization behaviour Fe–30% Mn and Fe–30% Mn–0.5% C, Materials Science and Engineering: A 527(16) (2010) 3785-3791.

[65] P. Kofstad, High temperature corrosion, Elsevier Applied Science Publishers, Crown House, Linton Road, Barking, Essex IG 11 8 JU, UK, 1988. (1988).

[66] B.A. Pint, R. Peraldi, P. Maziasz, The use of model alloys to develop corrosion-resistant stainless steels, Materials Science Forum, Trans Tech Publ, 2004, pp. 815-822.

[67] M. Yoshida, A. Seki, Y. Shirai, T. Ohmi, Passivation of stainless steel by δ-Al 2 O 3 films resistant to ozonized water, Journal of Vacuum Science & Technology A: Vacuum, Surfaces, and Films 17(3) (1999) 1059-1065.

[68] S. Basu, N. Obando, A. Gowdy, I. Karaman, M. Radovic, Long-Term Oxidation of Ti2AlC in Air and Water Vapor at 1000–1300° C Temperature Range, Journal of The Electrochemical Society 159(2) (2011) C90-C96.

[69] B.A. Pint, M.P. Brady, Y. Yamamoto, M.L. Santella, P.J. Maziasz, W.J. Matthews, Evaluation of alumina-forming austenitic foil for advanced recuperators, Journal of Engineering for Gas Turbines and Power 133(10) (2011) 102302.

[70] Y. Yamamoto, M.P. Brady, Z.P. Lu, C.T. Liu, M. Takeyama, P.J. Maziasz, B.A. Pint, Alumina-forming austenitic stainless steels strengthened by laves phase and MC carbide precipitates, Metallurgical and Materials Transactions A 38(11) (2007) 2737-2746.

[71] M.P. Brady, Y. Yamamoto, M.L. Santella, L.R. Walker, Composition, microstructure, and water vapor effects on internal/external oxidation of alumina-forming austenitic stainless steels, Oxidation of metals 72(5-6) (2009) 311-333.

[72] X. Xu, X. Zhang, G. Chen, Z. Lu, Improvement of high-temperature oxidation resistance and strength in alumina-forming austenitic stainless steels, Materials Letters 65(21) (2011) 3285-3288.

[73] Y. Yamamoto, G. Muralidharan, M.P. Brady, Development of L1 2-ordered Ni 3 (Al, Ti)-strengthened alumina-forming austenitic stainless steel alloys, Scripta Materialia 69(11) (2013) 816-819.

[74] J. Moon, M.-H. Jang, J.-Y. Kang, T.-H. Lee, The negative effect of Zr addition on the high temperature strength in alumina-forming austenitic stainless steels, Materials Characterization 87 (2014) 12-18.

[75] C. Thomson, V. Randle, “Fine tuning” at Σ3< sup> n</sup> boundaries in nickel, Acta materialia 45(12) (1997) 4909-4916.

[76] A. Belyakov, H. Miura, T. Sakai, Dynamic recrystallization in ultra fine-grained 304 stainless steel, Scripta materialia 43(1) (2000) 21-26.

[77] A. Belyakov, T. Sakai, H. Miura, R. Kaibyshev, Substructures and internal stresses developed under warm severe deformation of austenitic stainless steel, Scripta materialia 42(4) (2000) 319-325.

[78] I. Karaman, H. Sehitoglu, H. Maier, Y. Chumlyakov, Competing mechanisms and modeling of deformation in austenitic stainless steel single crystals with and without nitrogen, Acta materialia 49(19) (2001) 3919-3933.

[79] D. Canadinc, H. Sehitoglu, I. Karaman, Y. Chumlyakov, H. Maier, The role of nitrogen on the deformation response of hadfield steel single crystals, Metallurgical and Materials Transactions A 34(9) (2003) 1821-1831.

[80] I. Karaman, The competing effects of slip and twinning on the deformation of Hadfield manganese steel single and polycrystals, 2000.

[81] I. Karaman, H. Sehitoglu, Y.I. Chumlyakov, H.J. Maier, I. Kireeva, The effect of twinning and slip on the Bauschinger effect of Hadfield steel single crystals, Metallurgical and Materials Transactions A 32(13) (2001) 695-706.

[82] H. Sehitoglu, I. Karaman, X. Zhang, Y. Chumlyakov, H. Maier, Deformation of FeNiCoTi shape memory single crystals, Scripta materialia 44(5) (2001) 779-784.

[83] I. Karaman, H. Sehitoglu, A. Beaudoin, Y. Chumlyakov, H. Maier, C. Tome, Modeling the deformation behavior of Hadfield steel single and polycrystals due to twinning and slip, Acta Materialia 48(9) (2000) 2031-2047.

[84] I. Karaman, H. Sehitoglu, K. Gall, Y.I. Chumlyakov, On the deformation mechanisms in single crystal Hadfield manganese steels, Scripta materialia 38(6) (1998) 1009-1015.

[85] E. Zakharova, I. Kireeva, Y.I. Chumlyakov, S. Efimenko, H. Sehitoglu, I. Karaman, Deformation mechanisms and strain hardening of Hadfield-steel single crystals alloyed with aluminum, Doklady Physics, Springer, 2002, pp. 515-517.

[86] Y.I. Chumlyakov, I. Kireeva, E. Litvinova, E. Zakharova, N. Luzginova, H. Sehitoglu, I. Karaman, Strain Hardening in Single Crystals of Hadfield Steel, PHYSICS OF METALS AND METALLOGRAPHY C/C OF FIZIKA METALLOV I METALLOVEDENIE 90(SUPP/1) (2000) S1-S17.

[87] E. Zakharova, I. Kireeva, Y. Chumlyakov, A. Shul'Mina, H. Sehitoglu, I. Karaman, The effect of aluminium on mechanical properties and deformation mechanisms of

hadfield steel single crystals, Journal de Physique IV (Proceedings), EDP sciences, 2004, pp. 243-250.

[88] I. Kireeva, N. Luzginova, Y.I. Chumlyakov, I. Karaman, B. Lichter, Plastic deformation of nitrogen-containing austenitic stainless steel single crystals with low stacking fault energy, Journal de Physique IV (Proceedings), EDP sciences, 2004, pp. 223-230.

[89] Y. Chumlyakov, I. Kireeva, E. Zakharova, N. Luzginova, H. Sehitoglu, I. Karaman, Strain hardening and fracture of austenitic steel single crystals with high concentration of interstitial atoms, Russian physics journal 45(3) (2002) 274-284.

[90] S. Kibey, J. Liu, M. Curtis, D. Johnson, H. Sehitoglu, Effect of nitrogen on generalized stacking fault energy and stacking fault widths in high nitrogen steels, Acta materialia 54(11) (2006) 2991-3001.

[91] R. Viswanathan, W. Bakker, Materials for ultrasupercritical coal power plants—Turbine materials: Part II, Journal of Materials Engineering and Performance 10(1) (2001) 96-101.

[92] R. Klueh, A. Nelson, Ferritic/martensitic steels for next-generation reactors, Journal of Nuclear Materials 371(1) (2007) 37-52.

[93] T. Sourmail, Precipitation in creep resistant austenitic stainless steels, Materials science and technology 17(1) (2001) 1-14.

[94] M. Taneike, F. Abe, K. Sawada, Creep-strengthening of steel at high temperatures using nano-sized carbonitride dispersions, Nature 424(6946) (2003) 294-296.

[95] J.W. Christian, S. Mahajan, Deformation twinning, Progress in materials science 39(1) (1995) 1-157.

[96] E. El-Danaf, S.R. Kalidindi, R.D. Doherty, Influence of grain size and stacking-fault energy on deformation twinning in fcc metals, Metallurgical and Materials Transactions A 30(5) (1999) 1223-1233.

[97] I. Karaman, H. Sehitoglu, Y. Chumlyakov, H. Maier, The deformation of low-stacking-fault-energy austenitic steels, JOM 54(7) (2002) 31-37.

[98] S. Vercammen, B. Blanpain, B. De Cooman, P. Wollants, Cold rolling behaviour of an austenitic Fe–30Mn–3Al–3Si TWIP-steel: the importance of deformation twinning, Acta Materialia 52(7) (2004) 2005-2012.

[99] R.L. Peng, M. Odén, Y. Wang, S. Johansson, Intergranular strains and plastic deformation of an austenitic stainless steel, Materials Science and Engineering: A 334(1) (2002) 215-222.

[100] O. Bouaziz, S. Allain, C. Scott, P. Cugy, D. Barbier, High manganese austenitic twinning induced plasticity steels: A review of the microstructure properties relationships, Current opinion in solid state and materials science 15(4) (2011) 141-168.

[101] O. Bouaziz, D. Barbier, Benefits of Recovery and Partial Recrystallization of Nano-Twinned Austenitic Steels, Advanced Engineering Materials 15(10) (2013) 976-979.

[102] H. Wang, N. Tao, K. Lu, Strengthening an austenitic Fe–Mn steel using nanotwinned austenitic grains, Acta Materialia 60(9) (2012) 4027-4040.

[103] S. Kang, Y.-S. Jung, J.-H. Jun, Y.-K. Lee, Effects of recrystallization annealing temperature on carbide precipitation, microstructure, and mechanical properties in Fe–

18Mn–0.6 C–1.5 Al TWIP steel, Materials Science and Engineering: A 527(3) (2010) 745-751.

[104] G. Dini, A. Najafizadeh, R. Ueji, S. Monir-Vaghefi, Improved tensile properties of partially recrystallized submicron grained TWIP steel, Materials Letters 64(1) (2010) 15-18.

[105] W. Zhao, N. Tao, J. Guo, Q. Lu, K. Lu, High density nano-scale twins in Cu induced by dynamic plastic deformation, Scripta materialia 53(6) (2005) 745-749.

[106] O. Bouaziz, D. Barbier, Strain-Hardening in Nano-Structured Single Phase Steels: Mechanisms and Control, Journal of nanoscience and nanotechnology 12(11) (2012) 8732-8734.

[107] X. Zhang, A. Misra, Superior thermal stability of coherent twin boundaries in nanotwinned metals, Scripta Materialia 66(11) (2012) 860-865.

[108] V. Randle, V. Randle, The role of the coincidence site lattice in grain boundary engineering, Institute of Materials London1996.

[109] S. Asgari, E. El-Danaf, S.R. Kalidindi, R.D. Doherty, Strain hardening regimes and microstructural evolution during large strain compression of low stacking fault energy fcc alloys that form deformation twins, Metallurgical and Materials Transactions A 28(9) (1997) 1781-1795.

[110] X. Wu, X. Pan, J.C. Mabon, M. Li, J.F. Stubbins, The role of deformation mechanisms in flow localization of 316L stainless steel, Journal of nuclear materials 356(1) (2006) 70-77.

[111] Y. Zhang, N. Tao, K. Lu, Effect of stacking-fault energy on deformation twin thickness in Cu–Al alloys, Scripta Materialia 60(4) (2009) 211-213.

[112] J. Patel, M. Cohen, Criterion for the action of applied stress in the martensitic transformation, Acta Metallurgica 1(5) (1953) 531-538.

[113] P. Kelly, J. Nutting, The morphology of martensite, J. Iron Steel Inst 197(3) (1961) 199-211.

[114] İ. Üçok, T. Ando, N.J. Grant, Property enhancement in Type 316L stainless steel by spray forming, Materials Science and Engineering: A 133 (1991) 284-287.

[115] M. Eskandari, A. Najafizadeh, A. Kermanpur, Effect of strain-induced martensite on the formation of nanocrystalline 316L stainless steel after cold rolling and annealing, Materials Science and Engineering: A 519(1) (2009) 46-50.

[116] V. Seetharaman, R. Krishnan, Influence of the martensitic transformation on the deformation behaviour of an AISI 316 stainless steel at low temperatures, Journal of Materials Science 16(2) (1981) 523-530.

[117] K. Holloway, R. Sinclair, High-resolution and in situ TEM studies of annealing of Ti-Si multilayers, Journal of the Less Common Metals 140 (1988) 139-148.

[118] R. Sinclair, M. Parker, K. Kim, In situ high-resolution electron microscopy reactions in semiconductors, Ultramicroscopy 23(3) (1987) 383-395.

[119] H. Mecking, U. Kocks, Kinetics of flow and strain-hardening, Acta Metallurgica 29(11) (1981) 1865-1875.

[120] U. Kocks, H. Mecking, Physics and phenomenology of strain hardening: the FCC case, Progress in materials science 48(3) (2003) 171-273.

[121] O. Bouaziz, N. Guelton, Modelling of TWIP effect on work-hardening, Materials Science and Engineering: A 319 (2001) 246-249.

[122] Z. You, X. Li, L. Gui, Q. Lu, T. Zhu, H. Gao, L. Lu, Plastic anisotropy and associated deformation mechanisms in nanotwinned metals, Acta Materialia 61(1) (2013) 217-227.

[123] K. Lu, L. Lu, S. Suresh, Strengthening materials by engineering coherent internal boundaries at the nanoscale, Science 324(5925) (2009) 349-352.

[124] D. Fabrègue, O. Bouaziz, D. Barbier, Nano-twinned steel exhibits high mechanical properties obtained through ultra-rapid heat treatment, Materials Science and Engineering: A 712 (2018) 765-771.

[125] A. Grajcar, A. Kozłowska, B. Grzegorczyk, Strain Hardening Behavior and Microstructure Evolution of High-Manganese Steel Subjected to Interrupted Tensile Tests, Metals 8(2) (2018) 122.

[126] T. Zhu, J. Li, A. Samanta, H.G. Kim, S. Suresh, Interfacial plasticity governs strain rate sensitivity and ductility in nanostructured metals, Proceedings of the National Academy of Sciences 104(9) (2007) 3031-3036.

[127] A.T. Krawczynska, S. Gierlotka, P. Suchecki, D. Setman, B. Adamczyk-Cieslak, M. Lewandowska, M. Zehetbauer, Recrystallization and grain growth of a nano/ultrafine structured austenitic stainless steel during annealing under high hydrostatic pressure, Journal of Materials Science 53(16) (2018) 11823-11836.

[128] I. Kireeva, Y.I. Chumlyakov, Z. Pobedennaya, I. Kuksgausen, I. Karaman, Orientation dependence of twinning in single crystalline CoCrFeMnNi high-entropy alloy, Materials Science and Engineering: A 705 (2017) 176-181.

[129] B. Uzer, S. Picak, J. Liu, T. Jozaghi, D. Canadinc, I. Karaman, Y. Chumlyakov, I. Kireeva, On the mechanical response and microstructure evolution of NiCoCr single crystalline medium entropy alloys, Materials Research Letters 6(8) (2018) 442-449.

[130] M. El-Tahawy, Y. Huang, H. Choi, H. Choe, J.L. Lábár, T.G. Langdon, J. Gubicza, High temperature thermal stability of nanocrystalline 316L stainless steel processed by high-pressure torsion, Materials Science and Engineering: A 682 (2017) 323-331.

[131] J. Li, Y. Cao, B. Gao, Y. Li, Y. Zhu, Superior strength and ductility of 316L stainless steel with heterogeneous lamella structure, Journal of Materials Science 53(14) (2018) 10442-10456.

[132] J. Li, B. Gao, Z. Huang, H. Zhou, Q. Mao, Y. Li, Design for strength-ductility synergy of 316L stainless steel with heterogeneous lamella structure through medium cold rolling and annealing, Vacuum (2018).

[133] L. Xiong, Z. You, S. Qu, L. Lu, Fracture behavior of heterogeneous nanostructured 316L austenitic stainless steel with nanotwin bundles, Acta Materialia (2018).

[134] S. Wang, T. Jozaghi, I. Karaman, R. Arroyave, Y. Chumlyakov, Hierarchical evolution and thermal stability of microstructure with deformation twins in 316 stainless steel, Materials Science and Engineering: A 694 (2017) 121-131.

[135] T. Byun, N. Hashimoto, K. Farrell, Temperature dependence of strain hardening and plastic instability behaviors in austenitic stainless steels, Acta Materialia 52(13) (2004) 3889-3899.

[136] B. Zhang, F. Yan, M. Zhao, N. Tao, K. Lu, Combined strengthening from nanotwins and nanoprecipitates in an iron-based superalloy, Acta Materialia 151 (2018) 310-320.

[137] J.S. Li, W.D. Gao, Y. Cao, Z.W. Huang, B. Gao, Q.Z. Mao, Y.S. Li, Microstructures and mechanical properties of a gradient nanostructured 316L stainless steel processed by rotationally accelerated shot peening, Advanced Engineering Materials (2018) 1800402.

[138] N. Solomon, I. Solomon, Deformation induced martensite in AISI 316 stainless steel, Revista de metalurgia 46(2) (2010) 121.

[139] Z.-H. Jin, P. Gumbsch, K. Albe, E. Ma, K. Lu, H. Gleiter, H. Hahn, Interactions between non-screw lattice dislocations and coherent twin boundaries in face-centered cubic metals, Acta Materialia 56(5) (2008) 1126-1135.

[140] A. Van den Beukel, Theory of the effect of dynamic strain aging on mechanical properties, Physica status solidi (a) 30(1) (1975) 197-206.

[141] P. Rodriguez, Serrated plastic flow, Bulletin of Materials Science 6(4) (1984) 653-663.

[142] S. Mannan, K. Samuel, P. Rodriguez, Dynamic Strain Aging in Type 316 Stainless Steel, Trans. Indian Inst. Met. 36(4) (1983) 313-320.

[143] S. Mannan, K. Samuel, P. Rodriguez, The influence of grain size on elevated temperature deformation behaviour of a type 316 stainless steel, Strength of Metals and Alloys (ICSMA 6), Elsevier1982, pp. 637-642.

[144] S. Mannan, K. Samuel, P. Rodriguez, Stress-strain relation for 316 stainless steel at 300K, Scripta Metallurgica 16(3) (1982) 255-257.

[145] G. Bolling, R. Richman, Continual mechanical twinning: Part III: Nucleation and dislocation production Part IV: Cyclic twinning in Fe3Be single crystals, Acta Metallurgica 13(7) (1965) 745-757.

[146] G. Bolling, R. Richman, Continual mechanical twinning: Part II: Standard Experiments, Acta Metallurgica 13(7) (1965) 723-743.

[147] G. Bolling, R. Richman, Continual mechanical twinning: part I: formal description, Acta Metallurgica 13(7) (1965) 709-722.

[148] R. Armstrong, Dislocation dynamics, by AR ROSENFIELD, GT HAHN, AL BEMENT, Jr., and RI JAFFEE (1968) 293.

[149] B.C. De Cooman, Y. Estrin, S.K. Kim, Twinning-induced plasticity (TWIP) steels, Acta Materialia 142 (2018) 283-362.

[150] J. Kim, Y. Estrin, H. Beladi, I. Timokhina, K.-G. Chin, S.-K. Kim, B.C. De Cooman, Constitutive modeling of the tensile behavior of Al-TWIP steel, Metallurgical and Materials Transactions A 43(2) (2012) 479-490.

[151] I. Baker, N. Afonina, Z. Wang, M. Wu, Preliminary creep testing of the alumina-forming austenitic stainless steel Fe-20Cr-30Ni-2Nb-5Al, Materials Science and Engineering: A 718 (2018) 492-498.

[152] M. Brumm, H. Grabke, The oxidation behaviour of NiAl-I. Phase transformations in the alumina scale during oxidation of NiAl and NiAl-Cr alloys, Corrosion science 33(11) (1992) 1677-1690.

[153] M. Yoshida, A. Seki, Y. Shirai, T. Ohmi, Passivation of stainless steel by delta-Al2O3 films resistant to ozonized water, Journal of Vacuum Science & Technology A 17(3) (1999) 1059-1065.

[154] Y. Yamamoto, M.L. Santella, C.T. Liu, N.D. Evans, P.J. Maziasz, M.P. Brady, Evaluation of Mn substitution for Ni in alumina-forming austenitic stainless steels, Materials Science and Engineering: A 524(1) (2009) 176-185.

[155] B. Zhao, J. Fan, Y. Liu, L. Zhao, X. Dong, F. Sun, L. Zhang, Formation of L1 2-ordered precipitation in an alumina-forming austenitic stainless steel via Cu addition and its contribution to creep/rupture resistance, Scripta Materialia (2015).

[156] M.-H. Jang, J. Moon, J.-Y. Kang, H.-Y. Ha, B.G. Choi, T.-H. Lee, C. Lee, Effect of tungsten addition on high-temperature properties and microstructure of alumina-forming austenitic heat-resistant steels, Materials Science and Engineering: A 647 (2015) 163-169.

[157] W.-x. ZHAO, W. Yuan, S.-h. JIANG, W. Hui, X.-j. LIU, Z.-p. LU, Micro-alloying Effects of Yttrium on Recrystallization Behavior of an Alumina-forming Austenitic Stainless Steel, Journal of Iron and Steel Research, International 23(6) (2016) 553-558.

[158] M.P. Brady, Y. Yamamoto, M.L. Santella, B.A. Pint, Effects of minor alloy additions and oxidation temperature on protective alumina scale formation in creep-resistant austenitic stainless steels, Scripta Materialia 57(12) (2007) 1117-1120.

[159] M.P. Brady, K.A. Unocic, M.J. Lance, M.L. Santella, Y. Yamamoto, L.R. Walker, Increasing the upper temperature oxidation limit of alumina forming austenitic stainless steels in air with water vapor, Oxidation of Metals 75(5-6) (2011) 337-357.

[160] F. Stott, G. Wood, J. Stringer, The influence of alloying elements on the development and maintenance of protective scales, Oxidation of metals 44(1-2) (1995) 113-145.

[161] Y. Yamamoto, M.P. Brady, M.L. Santella, H. Bei, P.J. Maziasz, B.A. Pint, Overview of strategies for high-temperature creep and oxidation resistance of alumina-forming austenitic stainless steels, Metallurgical and Materials Transactions A 42(4) (2011) 922-931.

[162] S. Nie, Y. Chen, X. Ren, K. Sridharan, T. Allen, Corrosion of alumina-forming austenitic steel Fe–20Ni–14Cr–3Al–0.6 Nb–0.1 Ti in supercritical water, Journal of Nuclear Materials 399(2) (2010) 231-235.

[163] H. Sun, H. Yang, M. Wang, B. Giron-Palomares, Z. Zhou, L. Zhang, G. Zhang, The corrosion and stress corrosion cracking behavior of a novel alumina-forming austenitic stainless steel in supercritical water, Journal of Nuclear Materials (2016).

[164] X. Xu, X. Zhang, X. Sun, Z.P. Lu, Roles of Manganese in the High-temperature Oxidation Resistance of Alumina-forming Austenitic Steels at above 800 °C, Oxidation of Metals 78(5-6) (2012) 349-362.

[165] C. Wang, Study of Alumina in Austenitic Stainless Steels, Materials Science and Engineering Department, Texas A & M University, 2014.

[166] K. Ishida, Calculation of the effect of alloying elements on the Ms temperature in steels, Journal of Alloys and Compounds 220(1-2) (1995) 126-131.

[167] Q. Lu, W. Xu, S. Van Der Zwaag, A strain-based computational design of creep-resistant steels, Acta Materialia 64 (2014) 133-143.